

FIRST EXPERIMENTAL CONSTRAINT ON THE
 $^{191}\text{Os}(n, \gamma)$ REACTION RATE RELEVANT TO
S-PROCESS NUCLEOSYNTHESIS

by

Ina Kristine Berentsen Kullmann

THESIS
for the degree of
MASTER OF SCIENCE



Faculty of Mathematics and Natural Sciences
University of Oslo

May 2018

Abstract

The first experimentally constrained Maxwellian-averaged cross section for the $^{191}\text{Os}(n, \gamma)^{192}\text{Os}$ reaction relevant to s-process nucleosynthesis has been calculated by means of the nuclear level density and γ -strength function of ^{192}Os . By performing an experiment at the Oslo Cyclotron Laboratory (OCL) using an ion beam of 30 MeV α -particles, particle-coincidence data from the $^{192}\text{Os}(\alpha, \alpha'\gamma)^{192}\text{Os}$ reaction was obtained. The Oslo method was utilized on the resulting matrix of γ -ray spectra versus excitation energy to simultaneously extract the nuclear level density and the γ -strength function of ^{192}Os . Due to the lack of neutron-resonance data for the unstable isotope ^{191}Os , the required normalization parameters have been estimated by means of data from isotopes in the same mass region.

To calculate the Maxwellian-averaged cross section of the $^{191}\text{Os}(n, \gamma)^{192}\text{Os}$ reaction, the decomposed $E1$ and $M1$ strengths of the γ -strength function and the level density of ^{192}Os were used as input in the TALYS reaction code. The systematic uncertainties introduced by the normalization procedure of the level density and γ -strength function were investigated and propagated to the calculated Maxwellian-averaged cross section.

Quite large uncertainties were deduced in the final level density and γ -strength function of ^{192}Os . The errors propagated by the Oslo method software and the uncertainties introduced by the normalization parameters are found to be of approximately the same order of magnitude. The final result of the Maxwellian-averaged cross section, $\langle\sigma\rangle_{n,\gamma} = 1134 \pm 354$ mb, is in very good agreement with the theoretical estimate provided by the KADoNiS project. To study the impact of the present result on s-process nucleosynthesis in this mass region, the obtained cross section will, in the near future, be included in a reaction network taking branch points into account.

For mankind.

And of course my dear Dishwasher.

Acknowledgements

First, I would like to thank my supervisors Ann-Cecilie Larsen and Therese Renstrøm. You always welcome me with a smile, an open door when I seek your help, and motivate me with your everlasting good mood and encouragements. I have been extremely lucky to have you ‘on my team’. Thank you for thinking about my future, regardless of what it may bring.

A special thanks to the nuclear physics group as a whole, providing the best social environment (at UiO, probably), bringing students and employees together at lunch, conferences, summer schools and, of course, the Holmenkollen relay. Fabio, I hope we will have several spontaneous trips to Maridalsvannet and Norefjell in the future.

The last six years have given me great experiences. Thanks to Sara and Dayah for making my semester at MSU memorable. Thanks to Blindern, my second home (even at an early morning like this one), for making me feel welcome. If I could redo my time spent, I would choose to waste my time on Realistforeningen, Lillefy, FFU and MNSU again.

Thanks to the Basketball team for keeping me sane, giving me something to look forward to every week (and something new to organize). The other Kvantefysikk teaching assistants, thanks for taking parts of my workload when the deadline was closing in. Kine, you make me smile and provide perfect work-outs together with Katja. You are the best cheerleaders.

I am indebted to my office mate and partner in crime, Kristine. I am glad I met someone as crazy as me, we have more adventures to come. My never-forgotten past office mate, Ellen, may our argumentative discussions never end.

I am grateful to my dear family for your help and understanding. My big brother Carl-Erik, I look forward to our next trip. As always, I suggest we bring kites. Dad, I value our time spent in the mountains. Mum, your dinners are very much appreciated, specially those you bring me when I am in the middle of the sprint for the deadline. My perfect twin Annelise, you mean the world to me.

Finally, my beloved Trond, I would have been lost without your kindness and support. I love you.

Ina Kristine Berentsen Kullmann

May 16, 2018

Contents

1	Introduction	11
2	Nucleosynthesis beyond the iron peak	17
2.1	The s-process	20
2.2	The r-process	24
2.3	The p-process	25
2.4	The i-process	26
2.5	Reaction networks	26
2.5.1	Stellar input	27
2.5.2	Nuclear input	27
3	Experimental setup and data calibration	33
3.1	The Oslo Cyclotron Laboratory (OCL)	33
3.1.1	The experiment	35
3.1.2	The CACTUS and SiRi detectors	35
3.2	Detector calibration	38
3.2.1	Particle calibration and identification	40
3.2.2	Selecting the data from the $^{192}\text{Os}(\alpha, \alpha'\gamma)^{192}\text{Os}$ reaction	43
3.2.3	γ -calibration	43
3.2.4	Treatment of the time signals	45
3.2.5	The coincidence matrix	46
4	The Oslo method	49
4.1	Unfolding the γ -ray spectra	49
4.1.1	The folding iteration method	51
4.1.2	The Compton subtraction method	52
4.2	Extracting the first-generation γ -rays	54
4.3	Determining the nuclear level density and the γ -strength function	58
4.3.1	The χ^2 -minimization iteration method	58
4.3.2	The normalization procedure	60
5	Results and discussion	63
5.1	Obtaining the normalization parameters	63
5.1.1	The level density parameters	64
5.1.2	The γ -ray transmission coefficient parameters	66
5.1.3	Systematic error estimate	68
5.2	The level density	70
5.3	The γ -strength function	71
5.4	The radiative neutron capture cross section	74

6 Summary and outlook	81
6.1 Summary of the results	81
6.2 Upgrade of the experimental setup: OSCAR	82
6.3 Outlook	83
Bibliography	85

Chapter 1

Introduction

“We must wait, but we may trust the physicist that we do not have to wait too long.”

— Abbe G. Lemaitre, Nature 1931

Humans have wondered about our place in the universe for centuries. Step by step, our understanding of the origin, current state and future of the universe have improved by means of scientific studies. Currently, our knowledge is far from complete as many questions remain unsolved. One of the “Eleven Science Questions for the New Century” [1] involves explaining the origin of the elements from iron up to uranium.

The results obtained in the present work may be regarded as a tiny building block in this cosmological puzzle. The main goal of the thesis is to give a first experimental constraint on the neutron capture cross section for the $^{191}\text{Os}(n, \gamma)$ reaction by means of an experimentally obtained nuclear level density and γ -strength function of ^{192}Os .

In general, nuclear cross sections are relevant for several fields including reactor physics and medical diagnosis and treatments. Nuclear astrophysics is the application of focus in the current work. The $^{191}\text{Os}(n, \gamma)$ reaction may play a role in the formation of the heavy elements in asymptotic giant branch (AGB) stars. To set the experimental results in context, a brief historical overview of the scientific advances to explain the origin of the elements is given.

A short introduction to nuclear astrophysics

In 1957, E. Margaret Burbidge et al. [3] laid the very foundation of the nuclear astrophysics field in the article commonly referred to as B²FH. The famous paper proposed the hypothesis that all except the lightest chemical elements were synthesized in stars by nuclear reactions, i.e., stellar nucleosynthesis. Independently, in the same year, Cameron [4] proposed a similar framework explaining the origin of the elements by several synthesis processes. Impressively, the articles quite

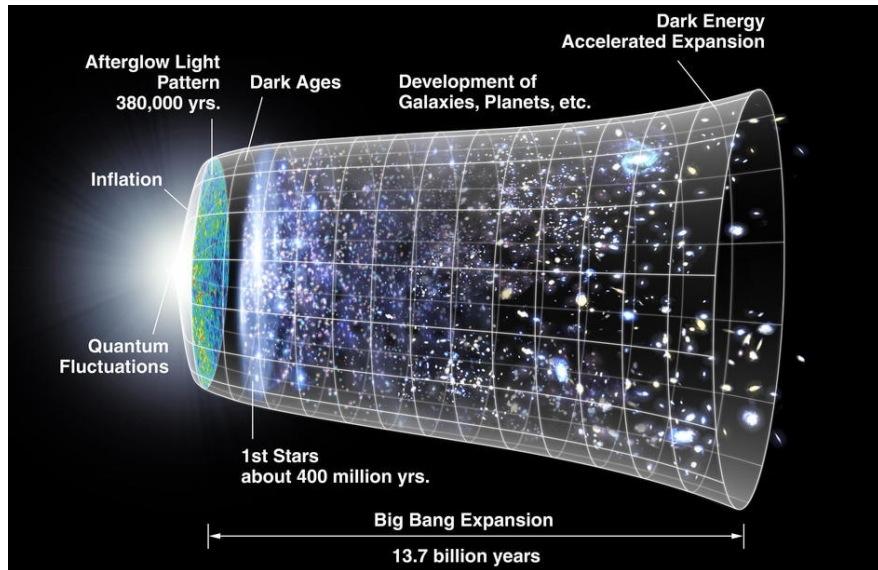


Figure 1.1: A NASA/JPL [2] illustration of the Big Bang and expansion of the universe. The cone represents the expansion of space itself from the beginning, i.e., the Big Bang, up to the present universe ~ 13.7 billion years later. The ‘Dark Ages’ refer to the period before the ignition of the first stars, but after the cosmic microwave background radiation (CMB), denoted ‘Afterglow Light Pattern’, was emitted. Quantum fluctuations in the very early universe are believed to explain the observed temperature fluctuations in the CMB, illustrated by the colored cross section of the cone right after the ‘Inflation’ (the early exponential expansion of the universe).

accurately describe the processes involved, and their theoretical descriptions are to a large extent still used today. For this reason, their work is one of the most important scientific theories of this century.

At the time the B²FH paper was published, the origin of the chemical elements was still under heavy debate. Multiple theories were considered probable, some deviating at a quite philosophical level. A common belief was that the universe was static, i.e., that the size does not change over time. F. Hoyle was a well known enthusiast and developer of the so called steady-state universe model assuming a static universe[5]. This assumption is in great contrast to the idea of an expanding universe first proposed by A. Lemaitre in 1931 [6]. In this picture, the universe would evolve, starting from a hot and dense primordial state. This idea has later evolved into our current prevailing cosmological model for the beginning of the universe, the so-called ‘Big Bang theory’¹, see Figure 1.1.

Relying on the expansion model, several theories assumed that all elements were formed in the early universe. In the 1940s, Gamow, Alpher, Herman and

¹Ironically, the famous ‘Big Bang’ name appeared in 1949 when F. Hoyle described, with some controversy, the model on a BBC radio show, and later in writing [7].

collaborators proposed that all elements would be synthesized shortly after the Big Bang, when the temperature was appropriate for nuclear reactions to occur [8, 9]. This gave a first explanation of the origin of the elements based on nuclear and cosmological arguments.

In Figure 1.2 the observed galactic elemental abundance distribution, mass number versus relative elemental abundance, is presented. Categorized by B²FH, the main nucleosynthesis processes are denoted. B²FH argued that any theory aiming to explain the origin of the elements must explain all general features observed in the abundance distribution. This was a major problem for the primordial nucleosynthesis models. The structures observed in Figure 1.2 cannot be accounted for when all elements are assumed to be produced in the early universe. B²FH, on the other hand, showed that all characteristics in Figure 1.2 can be properly explained with eight stellar processes taking place over the lifetime of the universe. The only primordial elemental production proposed was hydrogen.

Contradictory to the initial goal, the Big Bang theory cannot explain the origin of all elements. The model has been modified over the years, presently it accounts for the very lightest elements in Figure 1.2 [10]. Starting from an extremely hot and dense quark-gluon plasma, the universe expanded out to the size of our current universe. A few seconds after the beginning, the temperature dropped enough to allow nuclei to form, i.e., a quick Big Bang Nucleosynthesis (BBN) occurred. In this period only the very lightest elements were produced: mainly ¹H ($\sim 75\%$) and ⁴He ($\sim 24\%$), and small amounts of ²H and ³He ($\sim 0.01\%$) and traces of ⁷Li ($\sim 10^{-10}$) [10]. These isotopes correspond to the largest abundance peak denoted H and He, in addition to the very low abundance denoted Li-Be-B in Figure 1.2.

In stars, elements up to the iron peak can be synthesized in different burning stages, resulting in the peak around $A \sim 56$ denoted ‘Iron group’ in Figure 1.2. The peaks above the iron group, i.e., r- and s-peaks in addition to the line denoted p, are created by the main heavy element nucleosynthesis processes. The s- and r-processes rely on stepwise neutron captures and β -decays to build up the heavy isotopes. Several heavy proton rich nuclei are produced by the p-process by photodisintegrations, i.e., destruction of heavy s- and r-process elements.

Today the abundance distribution is modeled by large reaction network codes. These codes attempt to reproduce the observed distribution by evolving an initial abundance for a given time. In this way, the separate processes contributing to the abundance distribution can be quantified. In order to perform these calculations, nuclear and stellar input parameters are essential. An updated cross section value may or may not have a significant impact on the distribution. The origin of the elements can be better understood by improving the nuclear input, one step at the time.

Presently, a large portion of the nuclear input values rely on theory. The deviations between nuclear theories are largest for unstable nuclei. The neutron

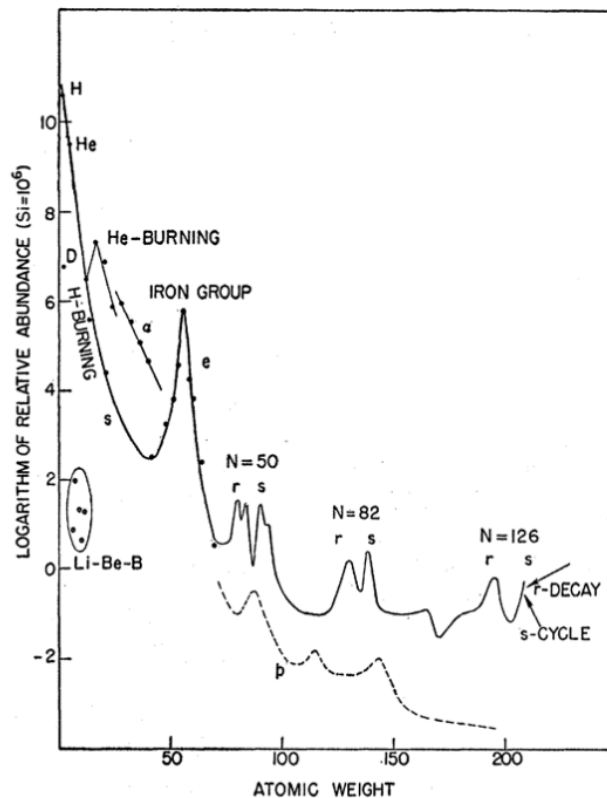


Figure 1.2: The abundance distribution, mass number versus relative abundance, as presented in B²FH [3]. Several nucleosynthesis processes were proposed by B²FH, all denoted with initials in the figure. The structures at masses above the iron group, i.e., the r- and s-peaks in addition to the line denoted p, are abbreviations for the rapid and slow neutron capture process and the proton capture process, respectively. Notice the logarithmic scale, the abundances of helium and hydrogen are many orders of magnitude larger than all of the other elements displayed.

capture cross section obtained in this work will be a first experimental constraint on the $^{191}\text{Os}(n, \gamma)^{192}\text{Os}$ reaction. This reaction occurs close to the valley of stability implying that the deviations between theory and experiment should be small. Even if the deviation between the old theoretical and the new experimental value should turn out to be small, new knowledge is not wasteful in this context. The result will provide a useful test of the theoretical predicting power in this mass region.

The field of nuclear astrophysics aims at explaining the origin of the elements and also the energy generation in stars. In this work, the main focus will be on the synthesis of the elements heavier than iron, more specifically the s-process, and relate this to the experiment performed. Our main goal is to motivate why

we need nuclear data to explain astrophysical phenomena and specifically why the nuclear level density and the γ -strength function are useful to astrophysics.

An overview of important definitions and concepts relevant for nuclear astrophysics, and most importantly the s-process, will be given in chapter 2. The experiment, experimental set-up and data calibration will be described in chapter 3, while chapter 4 introduces the Oslo method utilized to extract the level density and γ -strength function of ^{192}Os . Chapter 5 presents the main result, the Maxwellian-averaged cross section of the $^{191}\text{Os}(n, \gamma)^{192}\text{Os}$ reaction calculated by means of the level density and γ -strength function of ^{192}Os . A summary of the main findings and possible future work will be given in chapter 6.

Chapter 2

Nucleosynthesis beyond the iron peak

*“Our whole universe was in a hot, dense state
Then nearly fourteen billion years ago expansion started, wait
The earth began to cool, the autotrophs began to drool
Neanderthals developed tools
We built a wall (we built the pyramids)
Math, science, history, unraveling the mysteries
That all started with the Big Bang! Hey!”*

— Big Bang Theory Theme Song, Barenaked Ladies

Just after the Big Bang, the universe consisted of only hydrogen and helium. In the last ≈ 13.7 billion years, only about $\approx 1\%$ of the initial helium and hydrogen from the BBN have been converted into elements heavier than helium [12]. Given the astronomical scale, all of the present matter in the universe can be approximated to consist of $\approx 75\%$ hydrogen and $\approx 24\%$ helium. For this reason, astronomers refer to all elements heavier than helium as ‘metals’, and hydrogen and helium as ‘non-metals’.

Of course, without the 1% of metals, life as we know it would not exist. Our bodies, the earth and our food consist of elements heavier than helium. The nuclear chart, often called the periodic table for nuclear physicists (Figure 2.1), illustrates the rich diversity of the existing elements.

The elements up to the ‘iron peak’, i.e., around $Z \approx 26$ in Figure 2.1 are built up by charged-particle reactions during stellar burning. One may ask, why do these reactions not contribute to the formation of elements beyond the iron peak? The first reason is that the isotopes around ^{56}Fe have the largest binding energy per nucleon. This implies that the creation of heavier elements will demand energy instead of releasing it. If the reactions occur, the needed energy must be ‘stolen’ from the environment, decreasing the stellar temperature. This fact leads to the second argument, the probability for charged-particle reactions to

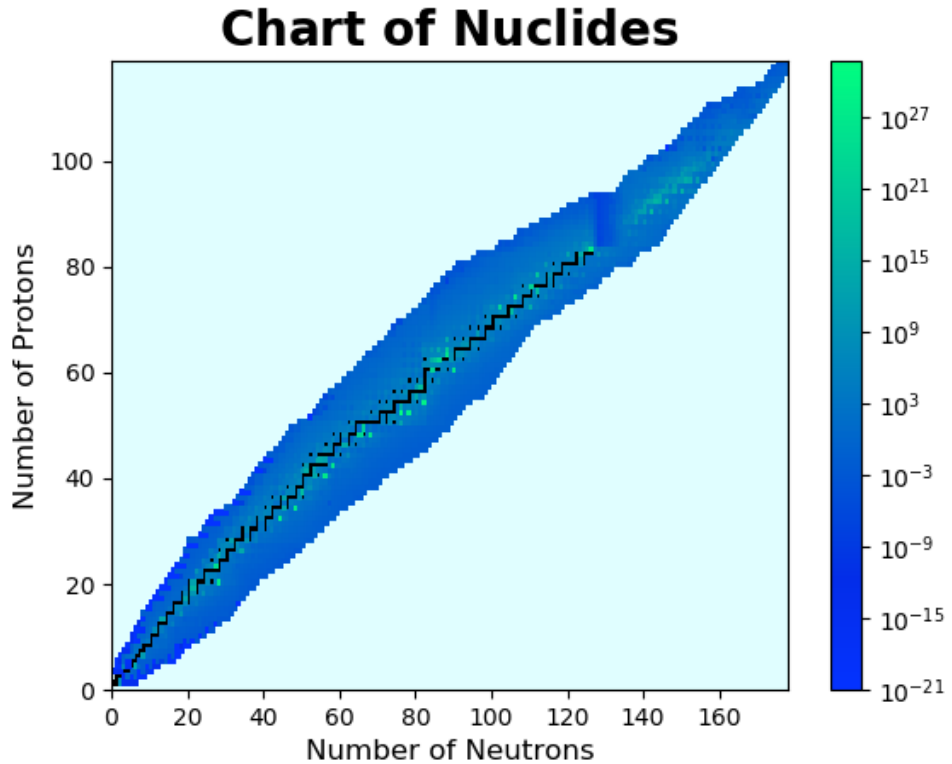


Figure 2.1: The nuclear chart, with the number of neutrons (N) versus protons (Z) for the experimentally known isotopes in the NUBASE2016 [11] database. Each box represents an isotope where the colors indicate the half-lives in seconds of the unstable isotopes. In general, the half-lives are longer closer to the black, stable isotopes forming the so-called ‘valley of stability’.

occur depends on the temperature of the environment, i.e., when the temperature decreases the probability decreases. This self-regulates the stellar environment so that charged-particle reactions involving elements heavier than iron are very unlikely.

Further, the probability depends on the charge of the involved nuclei, i.e., the number of protons Z . Classically, the reaction will only occur if the temperature allows the involved particles to come close enough, so that the repulsive Coulomb barrier will be overcome. In the quantum mechanical description, the reactions are allowed to occur at an energy below the Coulomb barrier via quantum tunneling. The probability of transmission through the potential barrier depends on the energy of the incident particle, i.e., the temperature of the environment. In addition, the tunneling probability is related to the height of the Coulomb potential which scales with the atomic number Z of the colliding nuclei. If the charge of the involved nuclei is large enough, the probability for a reaction to occur will be essentially zero given the stellar temperatures. The sum of the

above-mentioned arguments implies insufficient reaction rates involving isotopes heavier than iron during hydrostatic burning. Hence, other physical processes are required to explain the creation of elements heavier than iron. Realizing that neutrons do not feel the Coulomb force, the two most dominant nucleosynthesis processes called the slow (s) and the rapid (r) neutron capture process can be introduced. The idea is that the neutron can easily be captured by the nucleus independent of charge, building up the heavier elements.

The purpose of this chapter is to set the present work into context and relate the performed experiment to the astrophysical applications. Four nucleosynthesis processes will be outlined. The s-process will be described in most detail in section 2.1, in addition to the r-, p- and i-processes briefly summarized in section 2.2, 2.3 and 2.4, respectively. Other processes that are not believed to contribute significantly to the observed abundance distribution will be omitted. Section 2.5 presents the stellar and nuclear input needed in nuclear reaction network simulations applied to simulate the heavy-element nucleosynthesis processes.

Nuclear reactions in the stellar plasma

In order to simulate the synthesis of the elements, it is essential to know the probability for the reactions of all nuclei involved in the nucleosynthesis process. The nuclear cross section σ is a measure of probability for a nuclear reaction to occur. In nuclear astrophysics, the rate of a nuclear reaction, the number of reactions at a given temperature per time per unit volume, is also of vital importance.

In a stellar environment, the temperature T is governed by the velocities of the present particles. In this setting, it is natural that the cross section is velocity dependent: $\sigma = \sigma(v)$. Then, the reaction rate between two species 0 and 1 involved in a reaction $0 + 1 \rightarrow 2 + 3$ is given by [12]:

$$r_{01} = N_0 N_1 \int_0^\infty v P(v) \sigma(v) dv \equiv N_0 N_1 \langle \sigma v \rangle_{01}, \quad (2.1)$$

where $P(v)dv$ is the normalized probability that the relative velocity of the interacting species are in the range between v and $v + dv$. The number density (particles per volume) of particle 0 and 1 is denoted as N_0 and N_1 . Usually, the quantity $N_A \langle \sigma v \rangle_{01}$ is presented in the literature (N_A is Avogadro's number). The transformation is done in order to express the reaction rate in units of $\text{cm}^3 \text{mol}^{-1} \text{s}^{-1}$, removing the dependence of the number of particle pairs $N_0 N_1$ in Equation 2.1.

The reaction rate relates to the mean lifetime $\tau_1(0)$ of the nuclear species 0 destroyed by reactions with 1 in the stellar plasma through [12]:

$$r_{01} = \frac{1}{1 + \delta_{01}} \frac{N_0}{\tau_1(0)} = \frac{\lambda_1(0)}{1 + \delta_{01}}, \quad (2.2)$$

where $\delta_{01} = 1$ in the case of identical particles and zero for nonidentical particles. The decay rate $\lambda_1(0)$ is the number of decays per second.

The stellar plasma is non-degenerate and the reactants have non-relativistic velocities. Therefore, the velocities follow a Maxwell-Boltzmann distribution with a velocity maximum $v_T = \sqrt{2k_bT/m_{01}}$ at $E = k_bT$ (k_b is Boltzmann's constant) and reduced mass $m_{01} = m_0m_1/(m_0 + m_1)$. For neutron-induced reactions such as (n, γ) or (n, α) , the reaction rate (Equation 2.1) is often averaged over the Maxwell-Boltzmann velocity distribution giving the so-called Maxwellian-averaged cross section (MACS):

$$N_A \langle \sigma v \rangle_T \equiv \frac{N_A \langle \sigma v \rangle}{v_T} = \frac{4}{\sqrt{\pi}} \frac{N_A}{v_T^2} \int_0^\infty v \sigma_n(v) \left(\frac{v}{v_T} \right)^2 e^{(-v/v_T)^2} dv, \quad (2.3)$$

where $\sigma_n(v)$ is the energy dependent neutron-capture cross section. In the literature, the MACS values relevant for the s-process are usually presented at the energy $E = k_bT = 30$ keV, which is assumed to represent the most appropriate stellar temperature.

For the neutron capture processes, the (n, γ) reaction rate and the β -decay half-lives are the most significant parameters. Using the framework provided in Equation 2.2, the β -decay rate can be compared to the neutron capture rate in order to estimate the strongest decay path. For most known unstable nuclei, the half-life $t_{1/2}$ is experimentally known. Then, the decay constants are also known through the relation:

$$\lambda_\beta = \frac{1}{\tau} = \frac{\ln(2)}{t_{1/2}}, \quad (2.4)$$

where τ is the mean lifetime.

2.1 The s-process

As suggested by the name, the slow neutron capture process (s-process for short) is indeed a slow process. It takes place over the time span of long-lived stars, i.e., thousands of years involving neutron capture on stable nuclei. In contrast, the rapid neutron capture process (r-process) ends within a few seconds and includes very neutron rich, or extremely unstable nuclei.

The free neutron has a half-life of ≈ 15 minutes [10]. This implies that the s-process cannot take place in the interstellar medium, for which there are no known neutron sources. The s-process must take place in an environment that can provide a supply of neutrons during thousands of years. For this reason, stars were believed to be the perfect candidates for the s-process site as they live for millions of years.

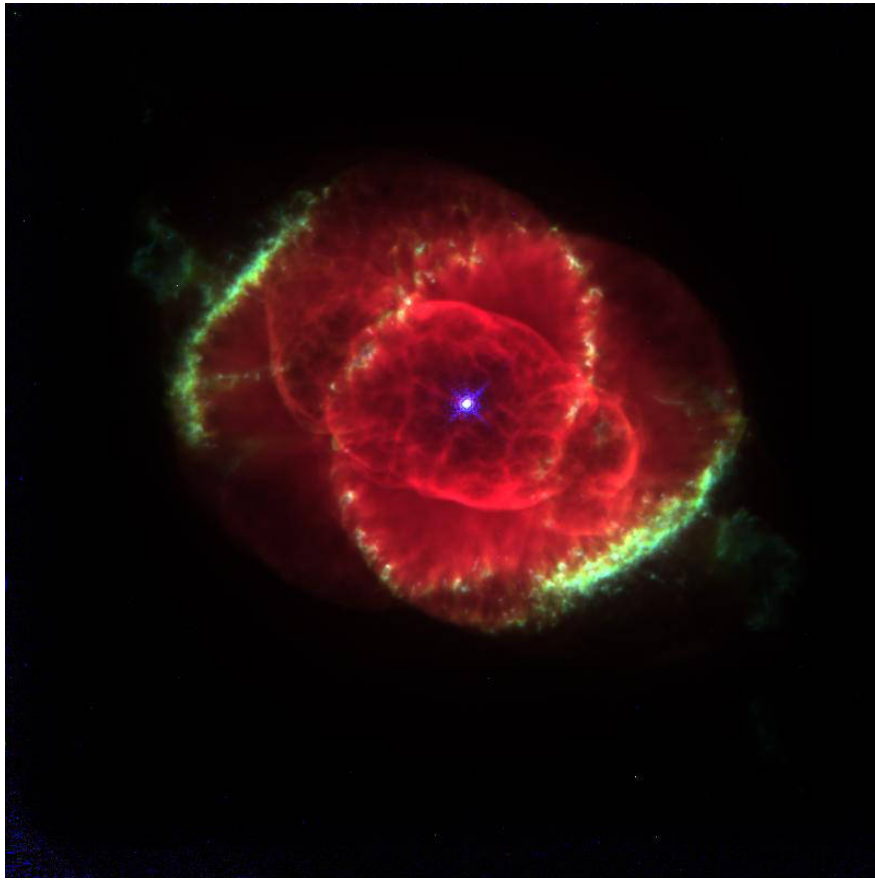


Figure 2.2: A NASA photo [13] of The Cat's eye nebula, a former AGB star [14] and s-process site. Layers of the AGB are thrown off the star after/during the thermal pulse periods and at the center a planetary nebula is left. These stellar winds would transport the s-process material away from the star and enrich the surrounding interstellar medium which later collapses into new stars.

The first astronomical observation of a live s-process was in 1952 when Merrill [15] discovered Tc absorption lines in red-giant and asymptotic-giant branch (AGB) stars, see Figure 2.2. Since Tc has no known stable isotopes, this observation provided a first evidence that the s-process nucleosynthesis must take place in stars. At the time, the observation was groundbreaking as there was no consensus on whether heavy-element nucleosynthesis took place in stars at all.

Today, two sites are considered for the s-process [16]: 1) AGB stars and 2) massive stars ($M > 8M_{\odot}$) during the helium burning phase. The main s-process component is proposed to produce the very heaviest nuclei at the first site, while the ‘weak’ component synthesizes elements up to about $A \sim 100$ at the latter site [16]. To provide a suitable neutron density, two main neutron sources have been proposed: the $^{13}\text{C}(\alpha, n)^{16}\text{O}$ and $^{22}\text{Ne}(\alpha, n)^{25}\text{Mg}$ reactions, active at the main and weak s-process sites, respectively [16]. These reactions release neutrons,

but require the involved reactants to be present at the site. This complicates the issue further because the exact stellar composition and dynamics are not well understood. Simulations of the interior of the star are often done in one dimension, and artificial pockets of ^{13}C and ^{22}Ne material are placed inside the star to obtain the desired chemical composition [17].

Nucleosynthesis material are observed at the surface of the star, but these elements are not synthesized at the surface. Therefore, some sort of convection between the layers within the star must take place, mixing the material, which is a complex and turbulent system to simulate [17]. To account for mixing, so-called dredge-up events are introduced, transporting material from the inside to the surface of the star. For more information about the astrophysical site of the s-process, model assumptions and uncertainties see the s-process review by Käppeler et al. [16].

In Figure 2.3, a small section of the chart of nuclides showing isotopes of Ta, W, Re, Os, Ir, Pt and Au is presented. The stable isotopes are represented by the black boxes, while the unstable are displayed in blue. All of the neutron rich isotopes positioned to the right of the stable isotopes are β^- unstable, i.e., β -decay is their main mode of decay. The s-process path, which is the direction of the abundance flow, is indicated with black arrows. The horizontal lines indicate radiative neutron capture (n, γ) and the diagonal lines indicate β -decay along isobars of constant A.

It is often assumed that the s-process starts from an abundance of seed nuclei, in a stellar environment with a neutron density of $N_n \approx 10^{11} \text{ cm}^3$ [12]. Then, the abundance flows through the nuclear chart close to the stable isotopes by a series of neutron captures and β -decays. In most calculations, a single seed species is used. Often ^{56}Fe ($Z = 26$ in Figure 2.1) is chosen since this is the most abundant isotope of the iron peak after stellar burning in heavy stars [12]. The s-process uses stable isotopes as stepping stones to build heavier elements and will therefore terminate at ^{209}Bi . This is the most massive stable isotope in the nuclear chart, i.e., the rightmost black point in Figure 2.1. Further neutron capture from this point will produce radioactive nuclei that decay by α -emission.

The abundance flows through stable ^{181}Ta first. Eventually, ^{181}Ta captures a neutron through the $^{181}\text{Ta}(n, \gamma)^{182}\text{Ta}$ reaction moving one step to the right in the chart. The next isotope, ^{182}Ta is unstable and will most likely β -decay before it captures another neutron. This reveals the main assumption of the s-process:

$$\lambda_\beta \gg \lambda_{n, \gamma} \quad (2.5)$$

i.e., the timescale $\tau \sim 1/\lambda$ for neutron capture (n, γ) is assumed to be much longer than the timescale for the competing β -decay for the unstable isotopes. In this simplification, only two competing processes are included, the neutron capture (n, γ) and β -decay. All other nuclear reactions are neglected as they are

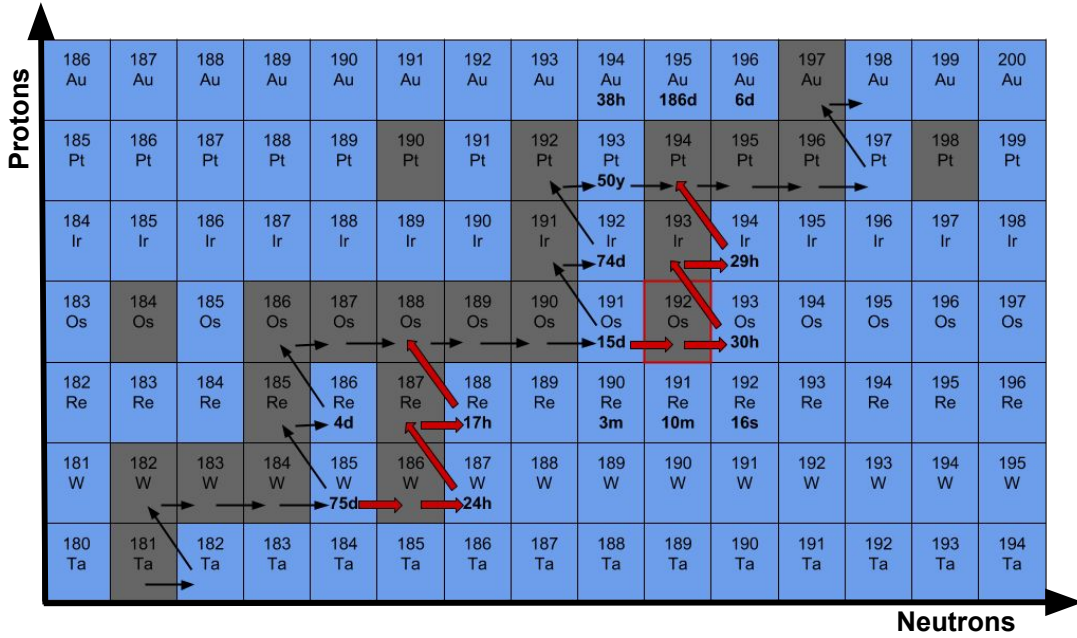


Figure 2.3: Section of the chart of nuclides, the dark boxes indicate a stable isotope while the blue are unstable isotopes. The halflifes / data are adapted from NNDC [18]. The path of the s-process is shown, possible branchings (red) and a few half-lives around ^{192}Os . The half-lives of the isotopes in the vicinity of ^{192}Os are indicated.

assumed to only contribute in small amounts in the astrophysical environment of the s-process.

Further, ^{182}Ta will β -decay into ^{182}W , which is stable. The stable nuclei are bound to undergo neutron capture transforming ^{182}W into ^{184}W . Relying on the assumption in Equation 2.5, the whole s-process path can be quite easily outlined in a similar manner. The s-process abundance moves in a zig-zag pattern in between the stable and the unstable nuclei, from the light to the heavier elements.

A complication is indicated by the red arrows in Figure 2.3. From the unstable nucleus ^{185}W two paths are indicated, i.e., a branching. The issue arises when the time scales of β -decay and neutron capture are similar. At such a branch point, neutron capture cannot be neglected. The unstable ^{185}W could undergo neutron capture or β -decay, and the assumption in Equation 2.5 breaks down.

A similar scenario to ^{185}W is indicated for ^{191}Os by the red arrows in Figure 2.3. The s-process path might go through ^{192}Os depending on the neutron capture and β -decay rate of ^{191}Os , i.e., the rate of the reaction $^{191}\text{Os}(n, \gamma)^{192}\text{Os}$ and λ_β . The β -decay half-life of ^{191}Os is considerably large, $t_{1/2} = 15$ days (see Figure 2.3), while the neutron capture rate of ^{191}Os presently relies solely on theory.

If the current theoretical value for the neutron capture rate of ^{191}Os is rea-

sonable, ^{191}Os is not a significant branch point [19]. The goal of this work is to provide a first experimental constraint the neutron capture cross section of ^{191}Os to compare with theoretical estimates recommended in the KADoNiS data base [19]. Further details on the calculation of the radiative neutron-capture cross section by means of the nuclear level density and the γ -strength function of ^{192}Os will be given in section 2.5.

2.2 The r-process

The rapid neutron capture-process (r-process) is known to operate far away from the stable nuclei. This implies a path to the far-right in the nuclear chart (Figure 2.1), i.e., isotopes with (extremely) short β -decay half-lives are involved. In contrast to the s-process, the main assumption of the r-process reads:

$$\lambda_\beta \ll \lambda_{n,\gamma} \quad (2.6)$$

demanding an extremely neutron rich environment ($N_n \approx 10^{20} \text{ cm}^3$) so that neutron capture is more likely than β -decay for unstable nuclei. In other words, a nucleus does not have enough time to β -decay before another neutron is captured.

In an r-process event, the abundance starts from several light seed nuclei. After a sequence of consecutive neutron captures, very unstable nuclei are reached. Far away from stability, the timescale for β^- -decay decreases rapidly. In the end $\lambda_\beta \approx \lambda_{n,\gamma}$ is reached, and a zig-zag pattern along the r-process path similar to the s-process is observed in simulations. After a few seconds, or less, the neutron source of the r-process will extinguish. Then, the abundance will flow from the unstable to the stable nuclei through a cascade of β^- decays. The final abundance produced by the r-process is the stable isotopes positioned along the isobars, i.e., constant mass number diagonals of the β^- decay routes (see, for instance, the r-process nucleosynthesis animation¹ of [20]).

The astrophysical site of the r-process has been unknown for decades; both supernovae and compact-object mergers were suggested sources for the observed r-process material [21, 22]. On August 17, 2017, the Advanced LIGO and Advanced Virgo gravitational-wave detectors made the first observation of a neutron star binary merger named GW170817 [23]. The gravitational-wave observation was immediately followed by a γ -ray burst, denoted GRB170817, detected by the Fermi Gamma-Ray Burst Monitor [24] and the INTEGRAL telescope [25].

During the days and weeks after the merger event, measurements of electromagnetic radiation by several telescopes in a broad range of frequencies revealed an ‘afterglow’ explained by the production of heavy isotopes [26] in the r-process. After years of speculations, this observation finally confirmed neutron star mergers as one the site for the r-process. The discovery does not exclude the existence

¹<http://jonaslippuner.com/research/skynet/>

of other astrophysical r-process sites, as further investigations of the explosion dynamics and chemical composition of supernovae are needed [27].

Many of the stable isotopes in Figure 2.3 will be produced in both the s- and r-process. If the branch points (red arrows) are ignored, the ^{186}W , ^{192}Os and ^{198}Pt isotopes are not reached by the s-process. These isotopes are called r-only nuclei since the r-process is the only process accounting for their existence. Similarly, ^{186}Os , ^{187}Os and ^{192}Pt are completely shielded from the r-process (assuming no branching) and are called s-only nuclei.

Usually the r-process contribution a_r to the total abundance a_{tot} can be disentangled from the s-process a_s by the relation:

$$a_r = a_{tot} - a_s, \quad (2.7)$$

assuming only an s- and r-process contribution to the abundance. The r-process distribution is traditionally estimated by means of the s-process since the astrophysical methods used to classify s-process elements are less uncertain [12]. Hence it is possible to connect observations of r-only elements to the r-abundance, providing a powerful tool for comparisons between theory and observations.

2.3 The p-process

The s- and r-process together produce the abundance of nearly all elements heavier than iron. However, about 30 proton rich nuclei are shielded from both neutron capture processes. These nuclei cannot be accounted for by either the s- or r-process. B²FH argued that at least one additional process is required to synthesize the p-nuclei and proposed the proton-capture process.

The abundance of p-nuclei is typically a factor of ten to thousand smaller than s- and r-isotopes of the same elements [28]. A single element will never have the p-process as the main synthesis contribution. Therefore, it is not possible to identify the p-abundance in stellar spectra². The determination of the p-abundances is based on measurements of solar system material such as meteoritic material and presolar grains [28].

The existence of the p-nuclei was at first explained by a proton capture process on stable nuclei and β^+ -decays, similar to the s-process [3]. Originally, the p-nuclei was defined as the nuclei not produced by either the s- or r-process. In this context, the term p-process is often sloppily used for any process producing p-nuclei, even if no proton captures are involved. Several models have been proposed to explain the p-nuclei including the photodisintegration process (γ -process) and ν -processes [29].

²Absorption lines in stellar spectra only reveal the element, not the isotope of the detected species.

The p-nuclei could be synthesized through the destruction of preexisting s- or r-nuclei by combinations of (p, γ) captures and (γ, n) , (γ, p) or (γ, α) photodisintegrations. To give suitable conditions allowing for photodisintegrations to take place, explosive environments are favored. Temperatures exceeding about $3.5 \cdot 10^9$ K are required, but only for a short amount of time. A long-lasting hot environment would imply total disintegration of the heavy elements into the iron peak nuclei. Therefore, core-collapse, Type Ia, Ib and Ic supernovae in addition to novae from binary star systems have been proposed as possible p-process sites, see [28] for further details.

2.4 The i-process

In 1977, Cowan and Rose [30] proposed that an intermediate (i) process with a neutron density in between those of the s and r-processes might be present in stars, i.e., $10^{11} < N_n \leq 10^{20}$ cm⁻³. The suggestion did not receive much attention until several stars with metallicities in between the s- and r-process extremes were observed, i.e., stars carrying a signature of both the s- and r-process.

Herwig et al. (2011) [31] suggested that the observed chemical composition in very metal poor stars can be explained by an intermediate neutron density of $N_n \approx 10^{15}$ cm⁻³. Using this neutron density, the abundance flows parallel to the valley of the stability in the nuclear chart. The path observed in simulations has an offset from the s-process of approximately 1-6 neutron numbers [32].

The neutron source suggested for the i-process, the $^{13}\text{C}(\alpha, n)^{16}\text{O}$ reaction, is the exact same reaction proposed for the main s-process. Therefore, critics may argue that the i-process is simply a version of the s-process and not a separate process in itself.

2.5 Reaction networks

To test the validity of nucleosynthesis models, nuclear reaction network simulations aim at reproducing the observed elemental abundance distribution. A simulation starts from an assumed initial abundance of a set of isotopes, and some given astrophysical conditions such as temperature and density. Then, the system can be evolved by allowing the isotopes to undergo nuclear reactions, using the probability for each reaction and isotope as input.

Ideally, a simulation would include all possible stellar and nuclear variables, but in principle this is not feasible within a finite computing time. Therefore, approximations have to be done to truncate the number of input variables.

2.5.1 Stellar input

To perform nucleosynthesis calculations, information about the stellar environment is needed. The temperature, density and chemical composition is of main interest for the nuclear reaction networks. To obtain these values, stars are modeled from an initial state to death through computer simulations. Several parameters affect the lifetime, most importantly the initial mass and metallicity (chemical composition) of the star [17]. Often stars rotate and will suffer mass loss over time, which also affects the fate of the star.

The interior material will also mix through convection between hot and cool layers within the star. Every isotope should in principle be tracked to calculate the energy generation within a pocket of the star. In addition, the temperature and density have to be evolved (in accordance with the energy generation), creating hydrodynamic convection streams within the star. All of these factors are time dependent, making it extremely demanding to evolve the spatial movement, temperature and density of the material. To omit several complicating factors, many simulations are performed in one dimension, and/or only including a limited section of the star [17].

Often the stellar dynamics is separated from the nuclear reactions. In this form of postprocessing, the nucleosynthesis is simulated after the evolution of the star. Then, the reaction network code can apply the initial isotopic abundance and the time evolution of the temperature and density suggested by the stellar hydrodynamics code.

2.5.2 Nuclear input

To further simplify the nucleosynthesis calculations, only the relevant reactions for a given process are included. For the s-process, all reactions except for (n, γ) and β -decay can be ignored to a good approximation [12]. The properties of the neutron sources $^{13}\text{C}(\alpha, n)^{16}\text{O}$ and $^{22}\text{C}(\alpha, n)^{25}\text{O}$ are also essential to determine the neutron density in the star. In principle, this is investigated in the stellar dynamics codes, and a post-process trajectory, or a constant neutron density is used in the reaction networks [16]. Then, only the MACS and half-lives for a given temperature and density are needed as nuclear input. The focus in this work is the MACS, i.e., the β -decay rates are assumed to be known and the temperature dependence of the β -decay half-lives [16] will not be discussed.

A complete set of experimental data is essential to give a reliable description of the abundance distribution. For stable nuclei, neutron capture rates can be measured directly through several experimental techniques [16]. However, numerous experimental difficulties are faced for short lived unstable nuclei. Therefore, most neutron capture rates are available for stable nuclei, while data is increasingly scarce for unstable isotopes. State-of-the-art radioactive beam facilities such as FRIB [33], FAIR [34] and HIE-ISOLDE [35] will be able to reach

a significant mass-range of the unstable nuclei, when fully operational. Nevertheless, performing direct measurements of (n, γ) cross sections might never be feasible. Therefore, experimental constraints on theoretical calculations will be indispensable in the time to come.

For the s-process, most neutron capture cross sections (n, γ) are tabulated in the compilation by Bao et al. [36] published via the KADoNiS project [37]. The library includes 357 isotopes, where 77 are radioactive nuclei on, or close, to the s-process path in the stellar temperature range $k_b T = 5 - 100$ keV.

The library includes both experimental and theoretically calculated values, and have been updated several times. Currently, 79 data sets (22.1%) rely on theoretical predictions with typical uncertainties of 25-30% [38]. For the $^{191}\text{Os}(n, \gamma)^{192}\text{Os}$ reaction investigated in this work, only a theoretical reaction rate is available [19]. Therefore, it is of interest to obtain an experimentally constrained MACS value by means of a nuclear level density and γ -strength function, obtained in the present analysis.

The level density and γ -strength function

Three nuclear input parameters are of key importance when calculating (n, γ) cross sections: the nuclear level density (NLD), the γ -strength function (γ SF), and the neutron optical-model potential (n-OMP) [21]. The latter will not be discussed here.

When the excitation energy of a nucleus is increased, the density of energy levels increases, as illustrated in Figure 2.4. The low-energy excitation region may be defined as the discrete energy range, where energy levels are easily resolved. At very high excitation energy, the level spacing is vanishing. Here, the levels are overlapping so that it is impossible to resolve individual energy levels; this happens in the continuum region. In between these two regimes, we can define the quasi-continuum region. Here, it is still theoretically possible to resolve the energy levels, but it is very difficult to keep track of all energy levels and the transitions between them.

In the quasi-continuum region, it is very useful to introduce statistical, or average properties such as the NLD and the γ SF to describe the nucleus. One may think of the NLD and the γ SF as the statistical counterparts of the discrete energy levels and individual transition probabilities.

The NLD is defined as the number of quantum energy levels accessible at a specific excitation energy, within a given energy bin. Experimentally, it is possible to obtain the level density at low energy by simply counting the number of levels, listed in databases such as NUDAT [39]. At higher excitation energies such level schemes are incomplete, and this method becomes unreliable. An example of an experimental procedure used to obtain the NLD is the Oslo method utilized in the current work. This technique determines the functional form of the level density between the discrete region and the neutron (proton) separation energy.

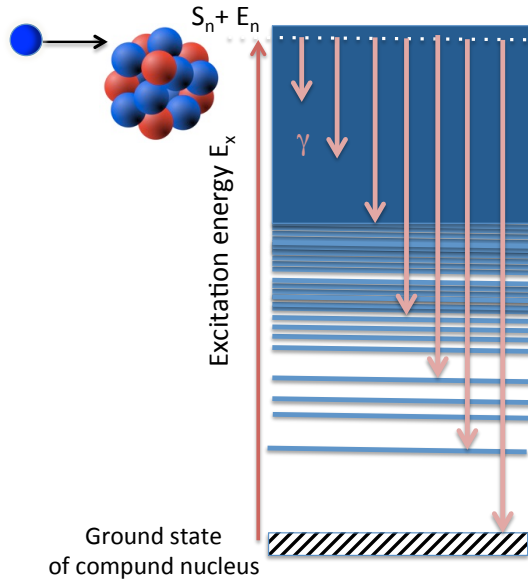


Figure 2.4: An illustration [40] of the energy levels in a nucleus Y, and the γ rays emitted following the neutron capture reaction $X(n, \gamma)Y$ presented to the left. Here X is the nucleus that captures the incident neutron n , with the incoming energy E_n , while Y is the ‘compound nucleus’. The neutron separation energy of Y is denoted S_n , and the excitation energy is denoted E_x .

A drawback of the method is that it is necessary to use information of discrete levels and neutron (proton) resonances in order to obtain the correct slope and absolute value of the NLD.

Several models have been proposed to give a theoretical or phenomenological description of the level density. In this work, two models will be considered: 1) the Hartree-Fock-Bogolyubov plus combinatorial (HFB+) model proposed by Goriely, Hilaire and Koning [41], and 2) the constant-temperature (CT) formula introduced by Ericson [42] and further combined with the Fermi-gas model leading to the much used composite formula by Gilbert and Cameron [43].

The CT model provides a simple, analytic formula for the NLD:

$$\rho(E) = \frac{1}{T_{CT}} \exp\left(\frac{E - E_0}{T_{CT}}\right), \quad (2.8)$$

where the nuclear temperature T_{CT} and the energy shift E_0 serve as free parameters to be adjusted to the experimental discrete levels.

For the HFB+ model, the level densities of more than 8500 nuclei are tabu-

lated [44]. These level densities are based on calculations using a microscopic and statistical approach, i.e., partially based on first principles, Skyrme interactions and phenomenological treatments.

The γ SF, also referred to as the radiative strength function and photon strength function in the literature, characterizes the average electromagnetic decay properties of excited nuclei. Bartholomew et al. [45] suggested a first model-independent definition of the γ SF, f :

$$f_{XL}(E_\gamma) = \frac{\langle \Gamma_{\gamma\ell} \rangle}{E_\gamma^{2L+1} D_\ell}, \quad (2.9)$$

where E_γ is the γ -ray energy with electromagnetic character X and multipolarity L . The average partial radiative width is $\langle \Gamma_{\gamma\ell} \rangle$ and D_ℓ represents the energy level spacing for ℓ -wave resonances determined from average resonance neutron-capture experiments. The γ -ray transmission coefficient \mathcal{T} is related to the strength function f through [46]:

$$f_{XL}(E_\gamma) = \frac{1}{2\pi} \frac{\mathcal{T}_{XL}(E_\gamma)}{E_\gamma^{(2L+1)}}. \quad (2.10)$$

Several theoretical models attempt to quantify the γ -SF. To a good approximation, the dominant radiation types involved in γ emission and absorption are $E1$ and $M1$ transitions [47]. Therefore, the total strength function can be decomposed into a separate $E1$ and $M1$ contribution:

$$f_{total} = f_{E1} + f_{M1}. \quad (2.11)$$

The generalized Lorentzian (GLO) model describes the giant electric dipole resonance ($E1$) as [46]:

$$f_{E1}^{GLO}(E_\gamma) = \frac{\sigma_{E1}\Gamma_{E1}}{3\pi^2\hbar^2c^2} \left(\frac{E_\gamma\Gamma_K}{(E_\gamma^2 - E_{E1}^2)^2 + E_\gamma^2\Gamma_K^2} + 0.7 \frac{\Gamma_{K,0}}{E_{E1}^3} \right), \quad (2.12)$$

where the last term is introduced to have a non-zero strength in the $E_\gamma \rightarrow 0$ limit. The peak cross section, energy centroid and width parameters are denoted as σ_{E1} , E_{E1} and Γ_{E1} , respectively. Further, Γ_K is a function of the γ -ray energy E_γ and the nuclear temperature parameter T_f of the final levels $E_f = E_x - E_\gamma$ is given by:

$$\Gamma_K(E_\gamma, T_f) = \frac{\Gamma_{E1}}{E_{E1}^2} (E_\gamma^2 + 4\pi^2 T_f^2), \quad (2.13)$$

so that $\Gamma_{K,0} = \Gamma_K(0, T_f)$. The giant magnetic dipole resonance ($M1$) can be

described by a standard Lorentzian (SLO) curve [46]:

$$f^{SLO}(E_\gamma) = \frac{1}{3\pi^2\hbar^2c^2} \frac{\sigma_{M1}E_\gamma\Gamma_{M1}^2}{(E_\gamma^2 - E_{M1}^2)^2 + E_\gamma^2\Gamma_{M1}^2}, \quad (2.14)$$

where σ_{M1} , E_{M1} and Γ_{M1} are the peak cross section, energy centroid and width of the SLO. A global parameterization [46] provides $E_{M1} = 41 \cdot A^{-1/3}$ MeV and $\Gamma_{M1} = 4$ MeV for a given mass number A . The peak cross section σ_{M1} can be determined by experimental data, or by using the relation $f_{E1}/f_{M1} = 0.0588 \cdot A^{0.878}$ at $\simeq 7$ MeV.

It can be useful to compare the γ SF to photo-absorbtion data, i.e., (γ, n) data. Assuming $L = 1$ (and detailed balance³), the photonuclear cross section σ_γ can be transformed into the γ SF f by [46]:

$$f(E_\gamma) = \frac{1}{3\pi^2\hbar^2c^2} \frac{\sigma_\gamma(E_\gamma)}{E_\gamma}. \quad (2.15)$$

This way, (γ, n) data can be combined with an experimental γ SF, often obtained in a different E_γ range. Through a fit of the GLO and SLO functions (Equation 2.12 and 2.14), the separate $E1$ and $M1$ contribution to the γ SF (Equation 2.11) can be estimated and used as input in reaction codes.

The TALYS nuclear reaction code

For a given set of nuclear input values it is possible to calculate the MACS by means of nuclear reaction codes. TALYS-1.9 [44] is an open source code that can be used to calculate nuclear reaction rates for astrophysical applications. The code can handle target nuclei with mass numbers between 12 and 339 [44]. Tables of experimental data are used when available and astrophysically important corrections are included, see [44] for further details.

The large number of available nuclear input parameters for the TALYS user can be overwhelming. There are eight available model options for the γ -strength function and six for the level density. For example, the HFB+ model described previously can be applied by choosing the level density model number 4 (`1dmodel 4`). If minimal input is given, predefined default variables are chosen [44].

In addition, it is possible to provide the code with user-defined input such as an experimental NLD and γ SF. In this way, a MACS value can be obtained by means of these essential experimental parameters, in addition to parameters relying on the theoretical framework.

By means of the experiment described in the next chapter and the Oslo method outlined in chapter 4, the NLD and γ SF for ^{192}Os will be obtained.

³Detailed balance is assumed, see e.g. Blatt and Weisskopf [48].

Then, the MACS for the $^{191}\text{Os}(n, \gamma)^{192}\text{Os}$ reaction (chapter 5) will be calculated by applying the experimental NLD and γ SF as input in the TALYS code.

Chapter 3

Experimental setup and data calibration

*“Do you write *The data is* or *The data are*? Is it singular or plural?*

-That is a deep philosophical question, actually. It depends on whether you consider data to be facts (plural) or information (which is singular). It’s a fascinating grammatical conundrum.

-What if I only have one data point?

-Then you have bigger problems than grammar.”

— Jorge Cham, Piled Higher and Deeper (PHD comics)

The purpose of this chapter is to give a brief introduction to the detectors, data acquisition system and methods used for experimental nuclear physics at the Oslo Cyclotron Laboratory (OCL). The experimental details will be discussed in section 3.1 and the detector calibration in section 3.2. The data analysis performed by means of the Oslo method and the motivation behind this technique will be described in chapter 4.

3.1 The Oslo Cyclotron Laboratory (OCL)

The Oslo cyclotron is an MC-35 Scanditronix model and one of the few accelerators in Norway for ionized atoms in basic research [49]. The accelerator is used in various fields of research including nuclear chemistry and medicine involving the production of radioisotopes for medical applications. Other applications of the cyclotron are proton radiation of cancer cells for basic research and radiation hardness testing of electronic chips. The main research project of the nuclear-physics group at OCL is the study of level densities and γ -ray strength functions.

An overview of the OCL is given in figure 3.1, where the cyclotron, situated inside the cyclotron vault (inner hall), is shown at the bottom right. The ac-

celerated particles travel along the beam line through several slits, dipole D_i , quadrupole Q_i , switching magnets and an analyzing magnet before hitting the target inside the target chamber (top left). The analyzing magnet directs the beam out of the cyclotron vault and into the experimental hall by turning the beam 90 degrees. The other magnets and slits shape and focus the beam. Finally, the beam reaches the target chamber in the center of the CACTUS/SiRi array. The switching magnets can be used to deliver beam to other target stations for isotope production or other experiments. The cyclotron delivers pulsed light-ion beams; the possible beam types, energy and intensity ranges are indicated in the table shown to the bottom left in Figure 3.1.

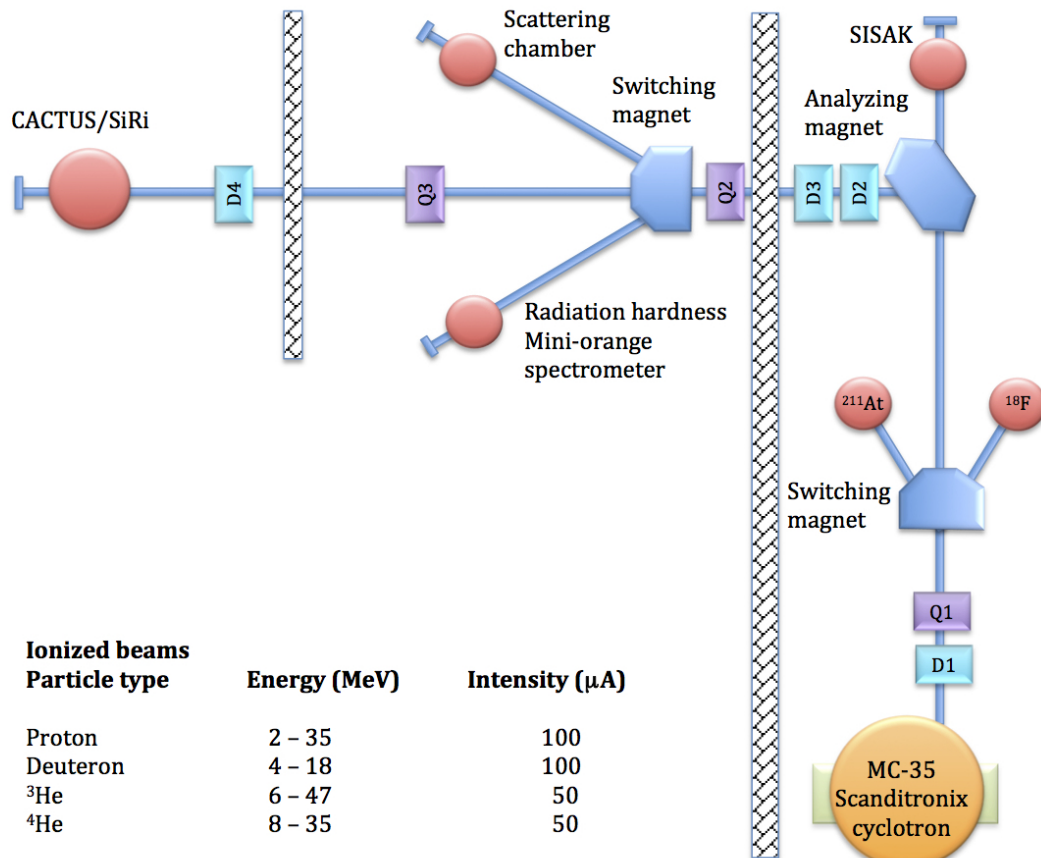


Figure 3.1: An overview of the Oslo Cyclotron Laboratory with the experimental hall to the left and the cyclotron at the bottom right. The beam line is indicated with a blue line and the target chamber is at the top left (CACTUS/SiRi). The possible beam types, energy and intensity ranges are indicated in the table to the bottom left. Illustration from [49].

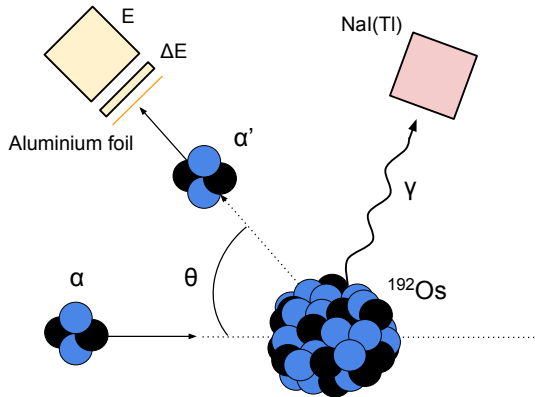


Figure 3.2: A sketch of an incident particle hitting a target nucleus in the $^{192}\text{Os}(\alpha, \alpha'\gamma)^{192}\text{Os}$ reaction (not to scale). The resulting emitted γ ray is detected by the CACTUS detectors and the emitted particle is detected by the SiRi detector positioned in backward angles. The angle between the incident trajectory and the trajectory of the emitted particle is given as θ . The two parts of the SiRi detector, ΔE and E is indicated in the figure, while the collimators for CACTUS are not shown.

3.1.1 The experiment

The present experiment was performed in May 2017 at the OCL, the University of Oslo, with the goal of studying the $^{192}\text{Os}(\alpha, \alpha'\gamma)^{192}\text{Os}$ reaction. An α -beam with an energy of 30 MeV was applied with a beam current of about 4 nA for about 3 days. The SiRi detector array was placed in backward angles, see subsection 3.1.2 for more details.

The ^{192}Os target is self supported, > 99% enriched and with a thickness of 0.33 mg/cm^2 [50]. In Figure 3.5 (right) a photograph of the ^{192}Os target is presented. There is clearly a burn mark in the center of the target on both sides from previous experiments [50]. It is assumed that the contamination is ^{12}C . A self-supporting ^{60}Ni target with a thickness of 2 mg/cm^2 was placed in the beam for approximately 2 hours at the beginning of the experiment for calibration purposes.

3.1.2 The CACTUS and SiRi detectors

The CACTUS/SiRi detector array is designed to study particle- γ coincidences by simultaneous measurement of charged particles and γ rays. Figure 3.2 shows an illustration of the reaction $^{192}\text{Os}(\alpha, \alpha'\gamma)^{192}\text{Os}$ studied in this thesis. The α -particle from the beam hits a target nucleus and scatters off the target. The target nucleus is excited and emits one or more γ rays which are measured by the CACTUS detector, while the energy of the α -particle is measured by SiRi. Of

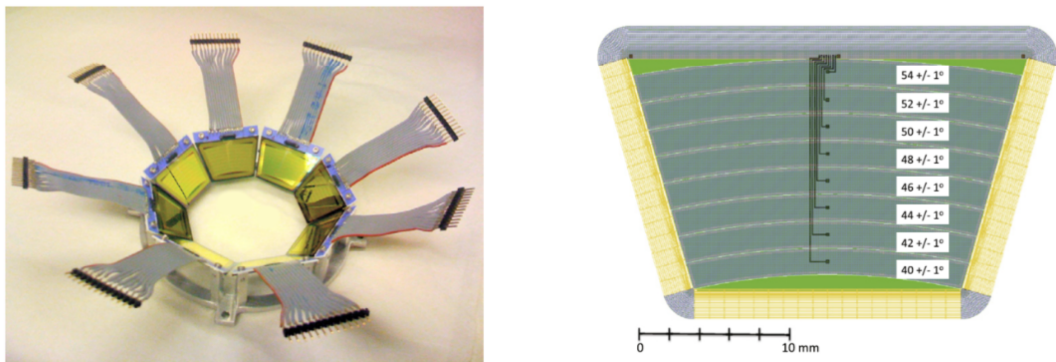


Figure 3.3: The SiRi detector used to measure the energy of a particle from a particle- γ coincidence. **Left:** A picture of the SiRi including cables to read out the signal. **Right:** An illustration of one of the eight ΔE detectors on the ring with the individual strips marked. Both taken from ref. [52].

course, other reactions will also occur when the α -particle hits the target nucleus, but only the $^{192}\text{Os}(\alpha, \alpha'\gamma)^{192}\text{Os}$ reaction will be studied in this work. The figure indicates that the angle between the incident trajectory and the trajectory of the emitted particle is given as θ . The SiRi array will measure the energy of all charged particles emitted in the solid angle that the array covers.

The SiRi detector array consists of eight separate silicon detectors in a ring placed inside the target chamber (Figure 3.3, left). Using the properties of the semiconductor the energy of the charged particles are measured. When a charged particle enters the detector material the silicon atoms are ionized and the electrons are collected due to the voltage applied. Then a signal, which is proportional to the energy of the incident charged particle, can be read out [51].

The detector is divided into two parts, one called ΔE and the other simply E . First, the particles travel through the ΔE detector ($130\ \mu\text{m}$) and then they stop in the E detector ($1550\ \mu\text{m}$ thick). In addition, an aluminium foil of $10.5\ \mu\text{m}$ thickness is placed in front of the ΔE detector to suppress δ -electrons. The positions of the ΔE and E detectors are indicated in Figure 3.2. Each ΔE detector is divided into eight strips making it possible to measure the angle θ of the particle (Figure 3.3, right). Together with the eight E detectors the eight ΔE strips form a particle-telescope system with 64 detectors. The SiRi-array are mounted at 5 cm distance from the target and covers angles from 40° to 54° when placed in the forward position, and 126° to 140° when placed in backward position [52]. The total solid angle coverage is $\approx 6\%$ of 4π and the angular resolution of the strips is $\approx 2^\circ$ [53].

A charged particle will lose some of its energy when traveling through the thin ΔE detector. It is desirable that the remaining energy is deposited in the E detector, i.e., the particles stop. If the charged particle travels through the E

detector we have ‘punch-through’. Given the beam energy, Q value of the reaction and target thickness, the energy of the charged particles traveling through the detectors can be calculated, e.g. by using the Qkinz application [54]. It is useful to check if the beam energy planned for an experiment will cause punch-through or not, and if so, the beam energy may be lowered. In the preparation of the $^{192}\text{Os}(\alpha, \alpha'\gamma)^{192}\text{Os}$ experiment, Qkinz was used to estimate the energy of the α -particles. This confirmed that the beam energy was suitable for the detector setup, i. e. the α -particles would stop in the E detector.

The fact that the SiRi-array has a thin and a thick silicon part makes it possible to distinguish the type of charged particles hitting the detector. By plotting the ΔE energy versus the E energy of the charged particles, so-called ‘banana plots’ are constructed. These plots contains one characteristic ‘banana’ for each particle type, see Figure 3.4. The particles’ difference in charge and mass affect the energy loss through matter [51], separating the particles in the ΔE versus E plot.

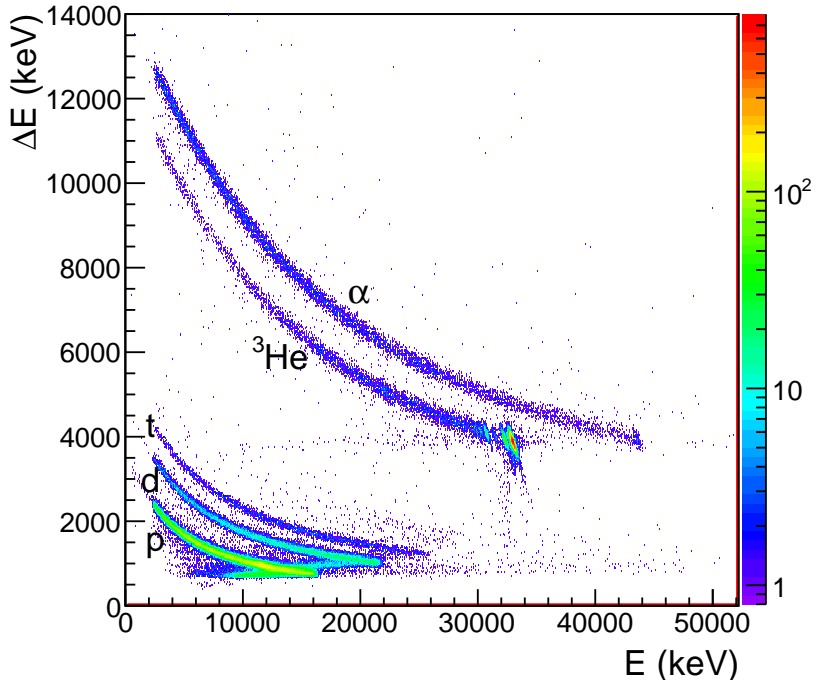


Figure 3.4: An example of a banana plot, ΔE vs. E of back detector one and front detector number five, i.e., strip b1f5. The figure is taken from [52] which studied the $^{112}\text{Cd}+^3\text{He}$ reaction with the SiRi array placed in forward angles. We observe one ‘banana’ corresponding to each type of ejected charged particle measured by the SiRi detector. The Qkinz application [54] can calculate the position and shape of the banana for a given charged particle and ejectile angle.

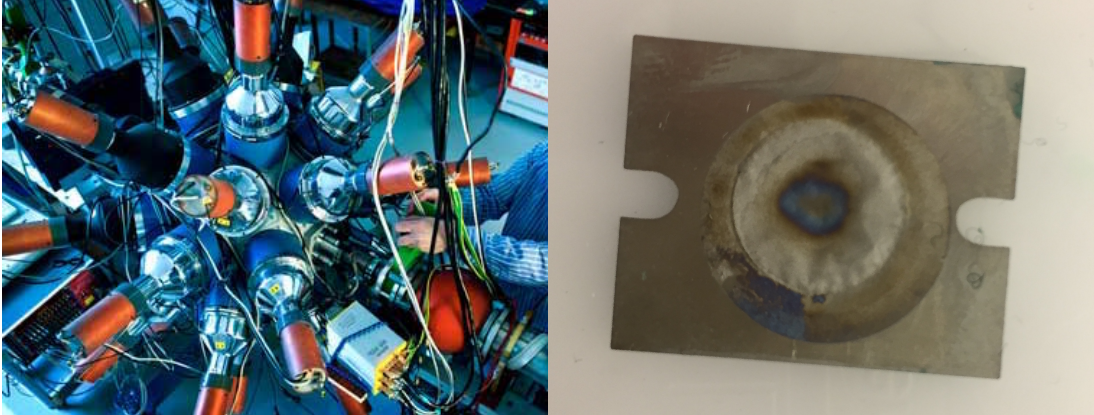


Figure 3.5: **Left:** The CACTUS detector at the Oslo Cyclotron Laboratory for the study of particle- γ coincidences. Picture taken from [49]. **Right:** The ^{192}Os target used in the $^{192}\text{Os}(\alpha, \alpha'\gamma)^{192}\text{Os}$ experiment with a burned mark in the center, see subsection 3.1.1 for further details.

The CACTUS detector array measures the energies of the γ rays. The detector system consists of 26 NaI(Tl) scintillation detectors mounted on a spherical frame surrounding the target chamber, pointing out like the spines of a cactus (Figure 3.5). The NaI(Tl) scintillation detectors measure the energy of the γ radiation by using the excitation effect of the γ radiation on the scintillator crystal. When the electrons in the scintillator are excited by a γ ray, they produce a cascade of photons in the range of visible light that are converted into an electrical signal by a photomultiplier tube [51].

Each crystal is $5'' \times 5''$ large and collimated with lead cones reducing their radius to $r = 3.5$ cm. The solid angle coverage of the collimated NaI(Tl) detectors is $\Omega = \frac{N\pi r^2}{4\pi R^2} = 16.4\%$ of 4π where $N = 26$ is the number of detectors and $R = 22$ cm is the distance between the target and detector. The total efficiency of the NaI(Tl) detectors is measured to be $14.1(1)\%$ at $E_\gamma = 1332.5$ keV [53]. More details of the detectors are given in [51] and more information on the detector and data-acquisition electronics setup at OCL is given in [52, 55, 56]. A summary of the most recent upgrades of the γ -detector setup at OCL (OSCAR) is given in chapter 6.

3.2 Detector calibration

It is known that the amplitude of an electric signal produced by a detector is proportional to the energy of the incoming radiation. However, the detector signal does not give the absolute value of the energy. Therefore, each amplitude is assigned to a *channel*, and the number of signals per channel is counted. For

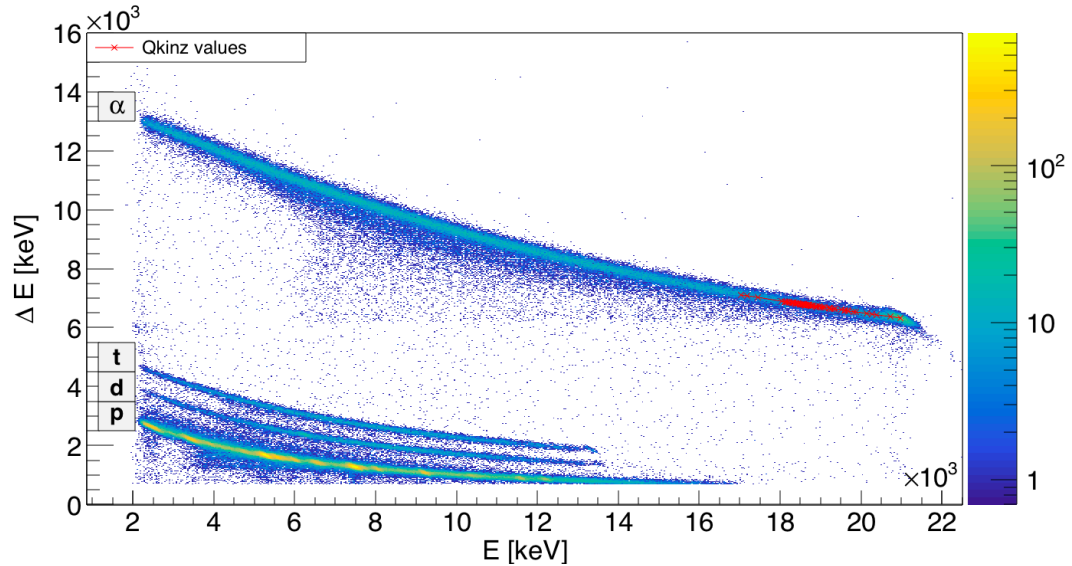


Figure 3.6: The calibrated banana-plot, ΔE versus E plotted for back and front detector number zero, similar to Figure 3.4 for the ^{192}Os experiment. On top of the α -banana the calculated Qkinz values [54] are shown in red.

each detector in the setup an energy spectrum, or histogram in arbitrary energy units is created. Unfortunately, the channel number and its corresponding energy for one detector does not necessarily match the same set of energy and channel number in another detector. This is due to varying properties of the individual detectors and differences in the electronic setup.

The goal is to calibrate the detectors so that the energy spectra, across all of the detectors, have the same physical features, the same peaks, at the same position and unit in the energy spectrum. Assuming a linear correlation between the true energy E in keV and the channel number ch , gives:

$$E = a + b \cdot ch, \quad (3.1)$$

where a is the shift (in keV) and b the gain (or dispersion, in keV/ch). The gain and shift coefficients a and b are determined by choosing two calibration points, i.e., two points of known energy in the spectrum. Then, a spectrum with the true absolute value of the energy on the axis is obtained.

In subsection 3.2.1 the gain and shift for the 64 particle detectors are found. The data corresponding to the $^{192}\text{Os}(\alpha, \alpha'\gamma)^{192}\text{Os}$ reaction is selected in subsection 3.2.2. Next, the same calibration principles for the 26 γ detectors are used in subsection 3.2.3 and finally the time signals are corrected in subsection 3.2.4. The calibration is done when the coincidence matrix is reached in subsection 3.2.5, which is the starting point of the Oslo Method outlined in chapter 4.

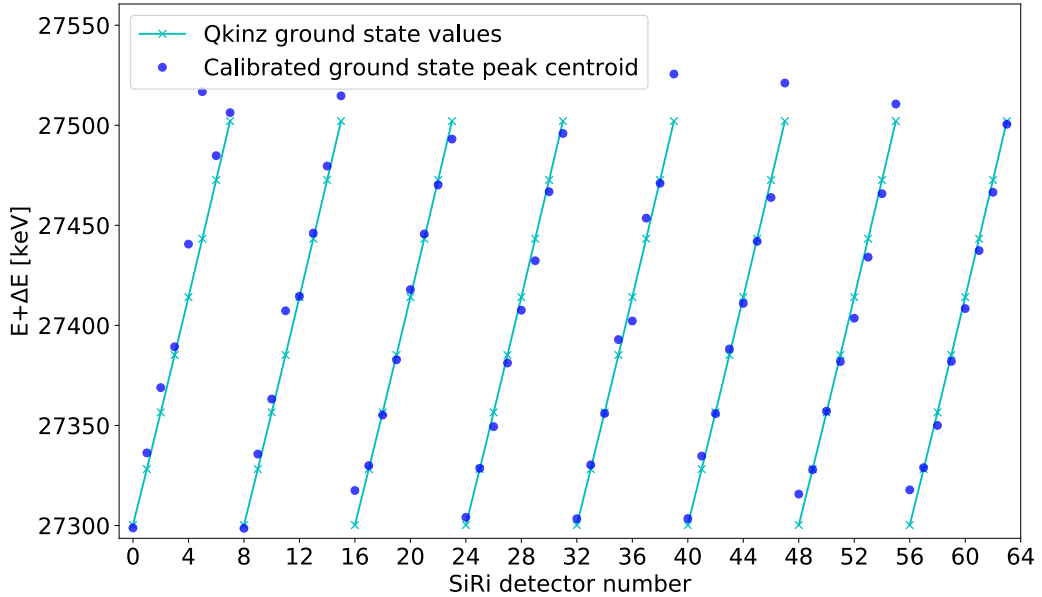


Figure 3.7: $\Delta E + E$ energy versus SiRi-detector number. The blue points are centroids of the ground state peak of the total particle energy $\Delta E + E$ histograms of ^{192}Os , found by a Gaussian curve fit. The calculated $\Delta E + E$ Qkinz values [54] are shown as diagonal lines.

All source codes used for calibration and analysis purposes developed at the OCL can be found in [57, 58].

3.2.1 Particle calibration and identification

When a ^{192}Os target is bombarded with α -particles, the SiRi detectors are mainly hit by protons, deuterons, tritons and α -particles caused by the corresponding $^{192}\text{Os}(\alpha, p)^{195}\text{Ir}$, $^{192}\text{Os}(\alpha, d)^{194}\text{Ir}$, $^{192}\text{Os}(\alpha, t)^{193}\text{Ir}$ and $^{192}\text{Os}(\alpha, \alpha'\gamma)^{192}\text{Os}$ reactions. In Figure 3.6 the calibrated bananas for the protons, deuterons, tritons and α -particles are shown together with the calculated Qkinz values for the $^{192}\text{Os}(\alpha, \alpha'\gamma)^{192}\text{Os}$ reaction in red.

The incoming α -particle has an energy of 30MeV. When it hits the ^{192}Os target it may transfer energy to the target nucleus and produce either ^{195}Ir , ^{194}Ir , ^{193}Ir or ^{192}Os . When energy is transferred from the incoming particle to the target, the resulting nucleus is either given additional kinetic energy, and/or it is excited to a higher energy level. The ground state of the target nucleus is observed if the ejected particle, i.e., the proton, deuteron, triton or α -particle leaves the residual nucleus in the ground state. In the banana-plot, Figure 3.6, the ground

state is observed as the rightmost peak on each banana¹. The position of the excited states are given by the reaction kinematics and result in peaks positioned to the left of the ground state peaks in the banana-plot.

In Figure 3.6 it is difficult to distinguish the excited states of the bananas. This is partially due to the resolution of the particle detectors. In addition, the spacing between the excited levels of ¹⁹⁵Ir, ¹⁹⁴Ir, ¹⁹³Ir and ¹⁹²Os decrease rapidly as a function of excitation energy.

As described in subsection 3.1.2, the SiRi array consists of a set of thin and thick detectors giving in total 64 detectors to calibrate. Theoretically, the detectors corresponding to the same ejectile angle should have identical banana plots, but in practice this is not the case (before calibration).

The fact that the stopping power of the projectiles in the detector material depends on velocity, mass and the charge of the particle is exploited in the calibration. The Bethe-Bloch formula [59] describes the average energy loss of ions traveling through and interacting with matter:

$$\frac{dE}{dx} = 2\pi N_a r_e^2 m_e c^2 \rho \frac{Z}{A} \frac{z^2}{\beta} \left[\ln \left(\frac{2m_e \gamma^2 v^2 W_{max}}{I^2} - 2\beta \right) \right] \quad (3.2)$$

where the parameters are given as [51]:

N_a	Avogadro's constant	z	charge of the incident particle (units of e)
r_e	classical electron radius	v	speed of the particle
m_e	electron mass	β	v/c
c	speed of light	γ	Lorentz factor $1/\sqrt{1-\beta^2}$
ρ	density of absorber	W_{max}	maximum energy transfer in a collision
A	mass number of absorber	I	mean excitation potential
Z	atomic number of absorber		

The Qkinz application uses the Bethe-Bloch formula or tables [60] to calculate the deposited energy in the ΔE and E detectors. This gives us the possibility to match the calculated energy in keV to the channel number of reference points in the banana plots. Two sets of equations are obtained when the linear correlation between energy and channel in Equation 3.1 is assumed to be true for both the ΔE and E detectors. Using two points, the ground state of ¹⁹²Os and the ground state of ⁶⁰Ni from the calibration run, the gain and shift coefficients a and b are determined for each detector.

¹We do not observe the ground state of the proton banana due to punch through in addition to the lower energy limit set for the ΔE detector in Figure 3.6.

Adding the particle detector energy into $\Delta E-E$ histograms separately for the 64 detectors, the energy calibration can be verified. The centroid of the peaks corresponding to the ground state of ^{192}Os (blue circles) after calibration and the corresponding Qkinz values (cyan crosses) are plotted against detector number in Figure 3.7. The detectors corresponding to the same angle θ has the same $\Delta E-E$ value due to the angle dependence of the SiRi setup, giving a repeating diagonal. For most of the data points, the calibrated centroids match very well with the calculated Qkinz values. We observe that some of the calibrated points are not following the Qkinz values as well as the others. This deviation is, however, well within the observed experimental resolution of ≈ 100 keV, observed as the standard deviation of a Gaussian fit of the ground state peak of ^{192}Os in Figure 3.8 (full width half maximum ≈ 235 keV).

The deposited energy in the SiRi detector, $\Delta E + E$, can be converted into excitation energy E_x for the final nucleus. Again, this is done by using the Qkinz-calculated values of deposited energy, taking into account the angle dependence. By using the known levels of the final nucleus the $\Delta E-E$ spectra are converted into E_x spectra, shown in Figure 3.8. The elastic peak, or the ground state is observed at zero excitation energy. Again, it is difficult to separate the first excited states of ^{192}Os due to the small level spacing and the resolution of the detector setup.

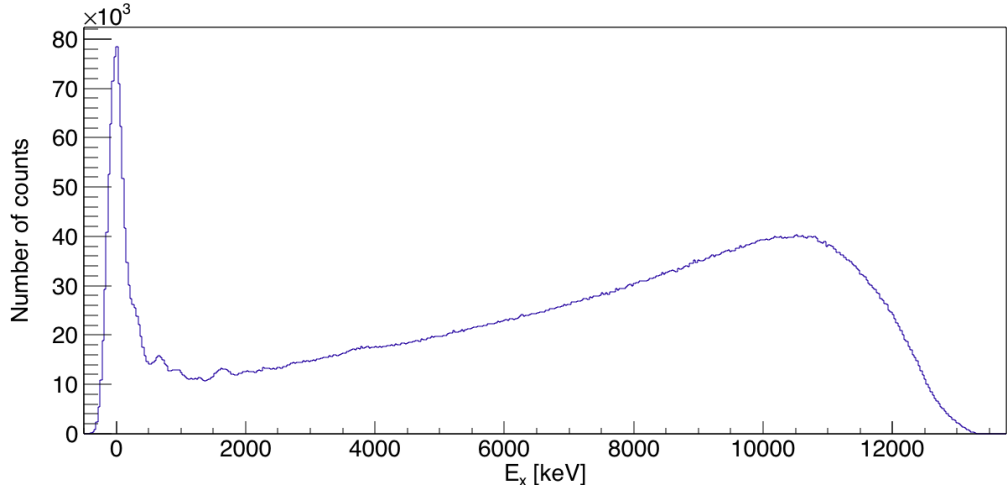


Figure 3.8: The deposited energy in the SiRi detector, $\Delta E + E$, converted into excitation energy E_x using calculated values from the Qkinz application [54] and corresponding known levels of ^{192}Os .

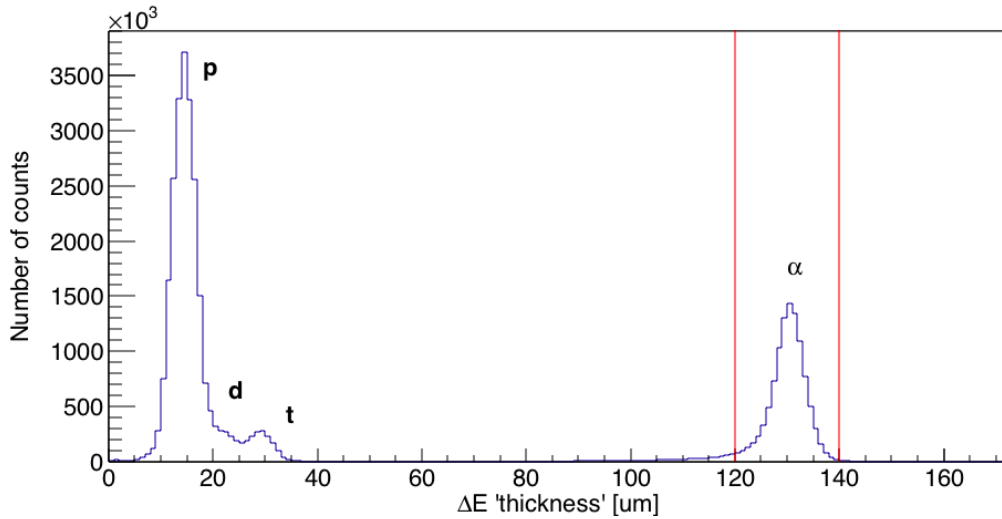


Figure 3.9: The apparent thickness spectrum showing the α -peak (α) centered at $\approx 130\mu\text{m}$, which is the true thickness of the ΔE detector. Selecting the data for the $^{192}\text{Os}(\alpha, \alpha'\gamma)^{192}\text{Os}$ reaction by applying the gates from $120\mu\text{m}$ to $140\mu\text{m}$ (red), excluding the peaks corresponding to the proton (d), deuteron (d) and triton-bananas (t).

3.2.2 Selecting the data from the $^{192}\text{Os}(\alpha, \alpha'\gamma)^{192}\text{Os}$ reaction

The goal is to only use data from the $^{192}\text{Os}(\alpha, \alpha'\gamma)^{192}\text{Os}$ reaction in our analysis. To select events from the (α, α') reaction, a gate on the ‘banana’ corresponding to the emitted α -particles is set. For this purpose we utilize known range functions (how far into a medium a particle can penetrate as a function of energy) to derive a thickness spectrum. In Figure 3.9 the apparent thickness of the front detector for the α -particles are shown. Clear and separated peaks corresponding to the different particle types are observed. The peak corresponding to the α -particles distribute around the central value, the true thickness of the ΔE detector ($130\mu\text{m}$). The applied gate from $120\mu\text{m}$ to $140\mu\text{m}$ is shown as red lines in Figure 3.9. When this gate is applied, data corresponding to the other emitted particles, i.e., protons, deuterons and tritons, are excluded.

3.2.3 γ -calibration

The 26 CACTUS γ -ray detectors are calibrated in a similar way to the SiRi particle detectors in subsection 3.2.1. Again, we assume a linear correlation between the true energy and the recorded channel number as described in Equation 3.1. As reference peaks we use: 1) the transition from the first excited 2^+ state to the ground state of ^{60}Ni at 1332.5 keV in the calibration data set, and 2) the

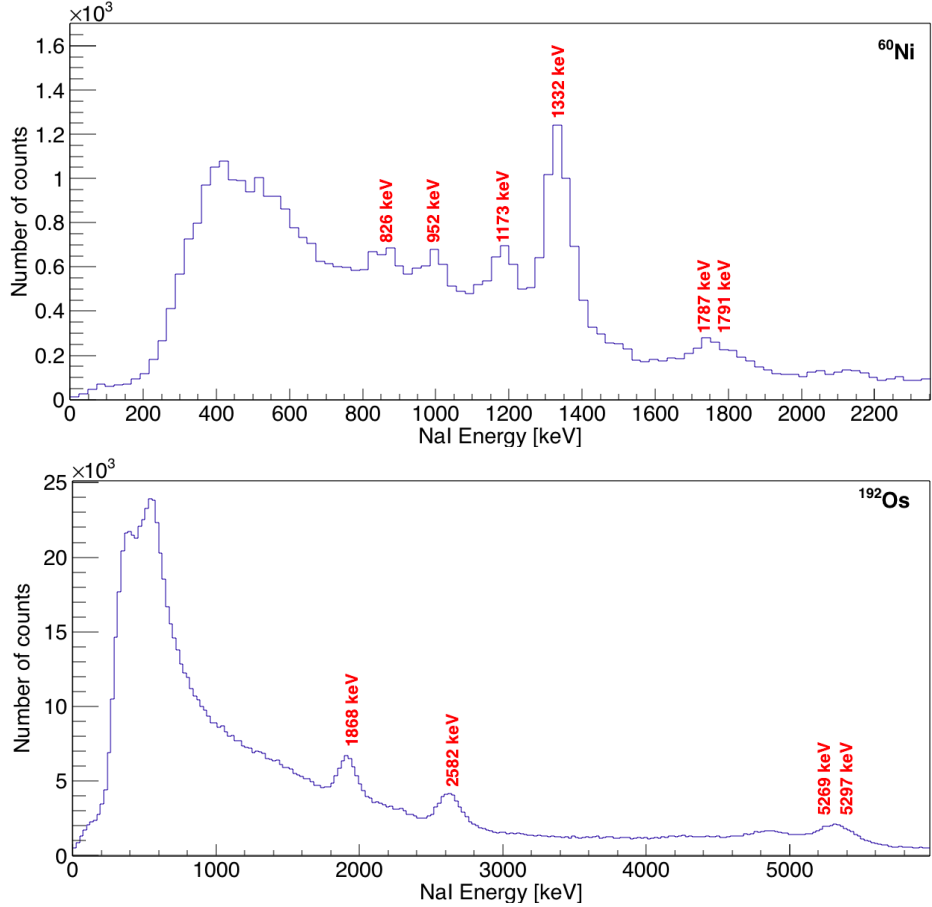


Figure 3.10: The calibrated γ -ray spectrum for ^{60}Ni (top) and ^{192}Os (bottom), see subsection 3.2.3 for details. The peaks with an energy of 1787 keV and 1791 keV in the ^{60}Ni spectrum and 5269 keV and 5297 keV in the ^{192}Os spectrum are not separable due to the resolution of the detectors. All energies were retrieved from [39].

transition from the $1/2^+$ excited state to the ground state of the contaminant ^{15}N at 5298.8 keV from the $^{12}\text{C}(\alpha, p)^{15}\text{N}$ reaction. For the latter purpose, a gate is set on the proton banana. Then, the shift and gain, a and b , of the 26 detectors are obtained by using Equation 3.1.

The calibrated γ -energy spectrum for ^{60}Ni (top) and ^{192}Os (bottom) with the calibration points marked are shown in Figure 3.10. The γ calibration can be verified by identifying the remaining peaks in the γ spectrum. In the top figure, from the calibration run, only peaks corresponding to low-lying transitions in ^{60}Ni are observed. In the bottom figure, the calibration peak at ~ 5.3 MeV from ^{15}N and two additional contaminants from the $^{16}\text{C}(\alpha, p)^{19}\text{F}$ reaction are observed. The peaks at 1868 keV and 2582 keV can be identified as a three-step cascade in ^{19}F from the $13/2^+$ state at 4648 keV via the $9/2^+$ state at 2779 keV, and to

the $5/2^+$ state at 197 keV. The $13/2^+$ state has also been observed in [61]. All known levels, transitions, intensities and energies were retrieved from [39].

3.2.4 Treatment of the time signals

To register coincidences between the α -particle and γ rays a time-to-digital converter (TDC) is used for each of the NaI(Tl) detectors. When a charged particle hits the SiRi-array a start signal is created, and when a γ ray is registered in the NaI(Tl) detectors the stop signal is produced. Due to small differences in the electronics and the photomultiplier tubes (PMTs) the time signals from the 26 γ detectors are not aligned. The time signals are shifted by positioning the prompt peaks in the same time channel. Then the time spectra from all of the detectors overlap well in time.

The stop signal of the TDC is delayed by ≈ 400 ns relative to the start signal. This implies that the duration of the time signal is longer than the cyclotron beam pulse period of ≈ 42 ns. Then, false coincidences are generated when a detected particle and γ ray do not stem from the same beam pulse. In Figure 3.11 the random coincidences are observed as smaller pulses before and after the prompt peak. The prompt peak is expected to contain both true and random coincidences. True events are obtained by subtracting the random events (channel 90 to 110) from the prompt peak (channel 175 to 195). The gates set for the prompt and random coincidences are shown in Figure 3.11. The counts of the random events are about 30% of the prompt peak.

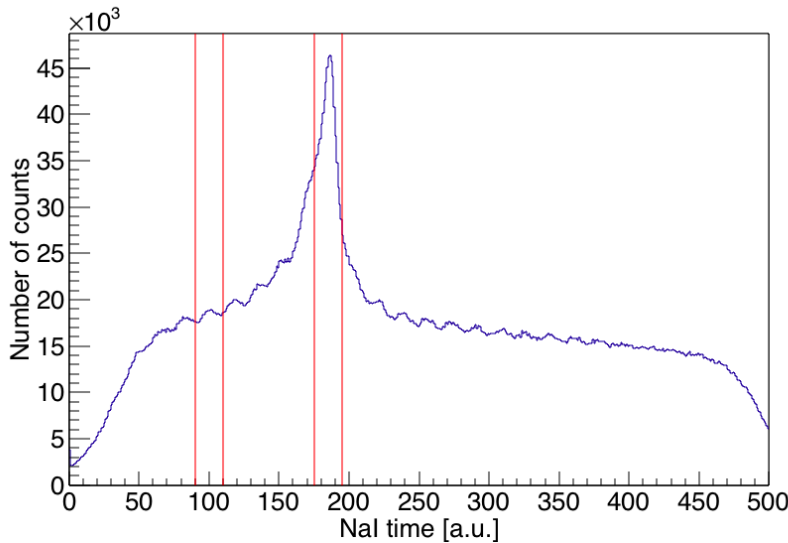


Figure 3.11: A typical TDC spectrum, the time channels versus number of counts for the γ detectors for the ^{192}Os experiment. The applied time gates are shown in red for the random events (right) and for the prompt peak (left).

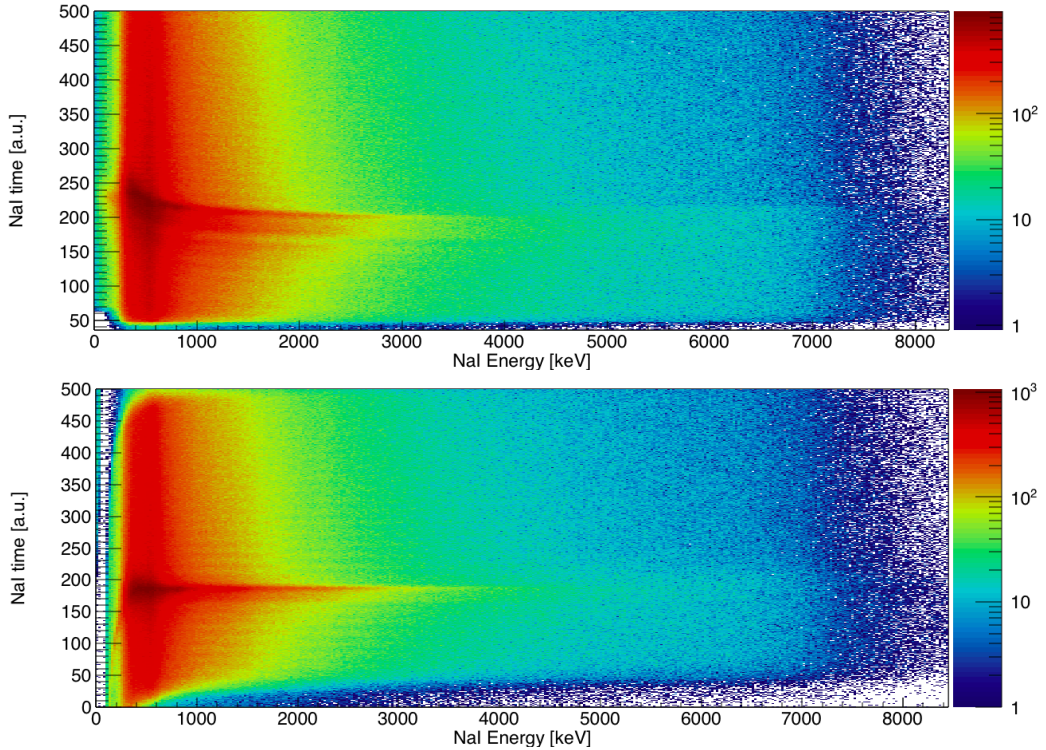


Figure 3.12: The time channels plotted versus the energy of all NaI(Tl) detectors. **Top:** uncorrected plot showing an energy dependence of the time signals. **Bottom:** corrected plot, corrected with a curve fitting, see [52].

Leading edge discriminators (LED) are used in the data acquisition system to process the time signals. Every time the amplitude of the signal is above a certain threshold, the discriminator starts the time signal. This threshold is independent of the pulse height of the signal. Signals with a larger amplitude have a shorter rise time, and will therefore set off the start signal at an earlier time. A higher amplitude corresponds to a higher energy, so high-energy signals will have a different time response than low-energy signals. The fact that the time signals are dependent on the pulse height is called ‘walk’ effects, visible in Figure 3.12 (top). To correct this effect we perform a curve fitting to the time spectra from all the NaI(Tl) detectors, see [52]. A similar time correction and curve fitting is done for the time spectra from the SiRi detectors. The time spectra for the NaI(Tl) detectors before and after the correction are presented in Figure 3.12.

3.2.5 The coincidence matrix

The α -particle may leave the ^{192}Os nucleus in an excited state, with an energy E_x . Then the excited ^{192}Os nucleus sends out γ ray(s) with energy E_γ , which

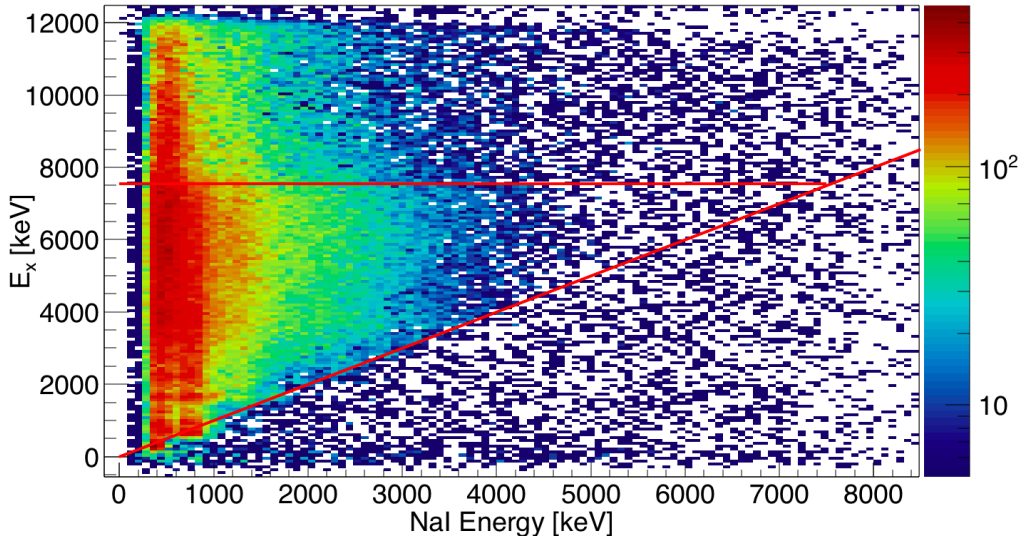


Figure 3.13: The simultaneous detection of an α -particle and γ ray(s) results in the particle- γ -ray coincidence matrix, the excitation energy E_x versus the γ energy for ^{192}Os .

can be detected by the CACTUS array. From the gates on the α -particles in the thickness spectrum, only events from the $^{192}\text{Os}(\alpha, \alpha'\gamma)^{192}\text{Os}$ reaction are selected (subsection 3.2.2). Similarly, the time gates set on the prompt peak in the time spectrum exclude the data that does not include the observation of an α -particle in the SiRi detector within the same time window (time gate) as the observation of γ rays in the CACTUS detectors (subsection 3.2.4). This way, the remaining events can be sorted into a matrix with the excitation energy E_x versus the γ energy E_γ on the y and x axis, and the number of counts on the z axis. Every point corresponds to the simultaneous detection of an α -particle and γ ray(s), hence the name ‘coincidence matrix’. The particle- γ -ray coincidence matrix of ^{192}Os is presented in Figure 3.13. At low energy a few discrete excited states are observed as peaks.

For a given transition, a γ ray is not physically allowed to have an energy exceeding the excitation energy, i.e., $E_\gamma > E_x$. This is observed as essentially no counts below the characteristic diagonal at $E_\gamma = E_x$, marked with a red line in Figure 3.13. Except at low energies, very few direct decays to the ground state are observed, i.e., there are few counts on the diagonal $E_\gamma = E_x$. In general, the coincidence matrix for ^{192}Os is quite empty at γ -ray energies exceeding ~ 3000 keV.

Neutrons cannot be measured in the detector setup. Therefore, it is not possible to separate particle- γ -ray coincidences due to the $^{192}\text{Os}(\alpha, \alpha'n\gamma)^{191}\text{Os}$ reaction from coincidences due to the $^{192}\text{Os}(\alpha, \alpha'\gamma)^{192}\text{Os}$ reaction. Both of these

reactions are therefore present above the neutron separation energy, marked with a horizontal red line in Figure 3.13. This part of the matrix will be excluded in the further analysis.

When the particle and γ -ray detectors have been calibrated, and with the coincidence matrix properly prepared, we are ready to start with the Oslo method described in the next chapter.

Chapter 4

The Oslo method

“Do what I do. Hold tight and pretend its a plan!”

— The Doctor, Dr. Who, Season 7, Christmas Special

The Oslo method is a set of tools developed by the nuclear physics group at OCL during the last 30 years, merged into one data-analysis framework. This technique is based on three main steps: 1) the unfolding of γ -ray spectra, 2) the extraction of first-generation γ rays, and 3) the determination of the NLD and γ SF as outlined in section 4.1, 4.2 and 4.3, respectively.

As explained in the previous chapter, the experimental setup at the OCL is designed to measure particle- γ coincidences with high efficiency. This setup provides the opportunity to study statistical γ rays as a function of excitation energy up to the neutron (or proton) separation energy. The benefit of performing the Oslo method is that it is possible to extract both the NLD and the γ SF, from one experiment, in this case the $^{192}\text{Os}(\alpha, \alpha'\gamma)^{192}\text{Os}$ experiment.

In this chapter, the methods and the underlying assumptions of the data analysis will be explained in detail, while the final solution of the NLD and γ SF of ^{192}Os will be presented in the next chapter. A discussion of the ^{192}Os parameters applied in the performed normalization will be set in the context of the estimate of the systematic errors introduced by this procedure in chapter 5.

4.1 Unfolding the γ -ray spectra

An incoming γ ray, with an energy E_γ , does not necessarily produce a signal in the detector matching the exact incident energy. In addition to the full energy peak at E_γ , features due to the detector’s response to radiation are observed. These features correlate with the various ways a γ ray may interact with matter. The goal of the unfolding method is to obtain a γ -ray spectrum only containing the full energy peaks.

When a γ ray with energy E_γ enters the detector material, it will most likely undergo one of the three dominant processes [51]:

1. The photoelectric effect.
2. Compton scattering.
3. Pair production.

Ideally, the detector would absorb all of the γ -ray energy, through one or multiple processes, creating the full energy peak at E_γ in the γ -ray spectrum. Unfortunately, energy loss occurs, resulting in ‘false’ peaks or structures at an energy below the incident γ -ray energy, i.e., $E' < E_\gamma$.

Compton scattering is observed as a continuous spectrum below the full energy peak. This is due to the angular dependence of the energy transfer from the γ ray to the electron. The γ ray may also undergo pair production, creating an electron-positron pair resulting in the single and double escape peaks. Quickly finding an electron, the positron will annihilate into two back-to-back γ rays, each with the exact energy of the electron mass. If one (or two) of the γ rays escape from the detector, a peak positioned at $E' = E_\gamma - 511$ keV (or $E' = E_\gamma - 2 \times 511$ keV) will be observed in the γ -ray spectrum. Pair-production in the surrounding material produce 511-keV γ rays observed at 511 keV.

The coincidence matrix (subsection 3.2.5) projected on the x-axis can be thought of as a range of γ -ray spectra, F . For each excitation energy bin a γ -ray spectra F_i is obtained. In addition to distortions of the γ -ray energy, the experimental spectra contain the full-energy peaks at E_γ . By doing in-beam mono-energetic γ -line measurements, the total response of the detector setup can be determined, obtaining the response functions. The information is stored in a matrix $\mathbf{R}(\mathbf{E}', \mathbf{E}_\gamma)$ representing the probability for a count in the detector with energy E' for an incident γ ray with true energy E_γ . The NaI-response functions applied in this work were updated in 2012, see [53].

In matrix form, the measured γ -ray spectrum F can be written as [62]:

$$F = \mathbf{R}u, \quad (4.1)$$

or

$$\begin{pmatrix} F_1 \\ F_2 \\ \vdots \\ F_N \end{pmatrix} = \begin{pmatrix} R_{11} & R_{12} & \cdots & R_{1N} \\ R_{21} & R_{22} & \cdots & R_{2N} \\ \vdots & \vdots & \ddots & \vdots \\ R_{N1} & R_{N2} & \cdots & R_{NN} \end{pmatrix} \begin{pmatrix} u_1 \\ u_2 \\ \vdots \\ u_N \end{pmatrix}$$

where \mathbf{R} is the response function and u the true, unfolded spectrum. The goal is to obtain u . By inverting the equation mathematically, u is easily solved for:

$$u = \mathbf{R}^{-1}F, \quad (4.2)$$

but in practice this turns out to be a challenging problem to solve. The dimension of the matrix is large, and division or multiplication by very large or small matrix elements may lead to numerical truncation errors in addition to large, unreal fluctuations and possible unstable solutions. Although there exist a number of matrix inversion algorithms taking these issues into account, it is not necessary to invert the matrix to solve the matrix equation, see for instance [63]. In this work the folding iteration method [62] described in the next section will be applied to obtain u without using Equation 4.2 directly.

The operation in Equation 4.1 will be referred to as ‘folding’ while the operation in Equation 4.2 will be referred to as ‘unfolding’, i.e., F is the ‘folded’ spectrum while u is the ‘unfolded’ spectrum.

4.1.1 The folding iteration method

Opposed to matrix inversion, folding is bound to yield one solution only. Folding is also fast and simple, which can be exploited in an iteration algorithm. Usually, the full measured experimental spectrum r is taken as the guess function for the unfolded spectrum u^0 . The first iteration is then the folding of the trial function given as $F^0 = \mathbf{R}u^0$.

Of course, the exact folded spectrum, i.e., the experimental spectrum r , is known. This provides the opportunity to calculate the error in the initial guess by the difference method: $r - F^0$. The new guess function u^1 is created by adding the error to the current solution: $u^1 = u^0 + (r - F^0)$. This way the next solution u^{n+1} is obtained by using the previous solution u^n and the error. In Code 4.1 an outline of the generalized iteration method is given.

```
# Initialize:
# R = response matrix
# r = the measured spectrum

u[0] = r

for n in [0,1,2,...]:
    F[n] = R * u[n]
    u[n+1] = u[n] + (r - F[n])
    # calculate 'goodness factor':
    ...
end loop over n
```

Code 4.1: The folding iteration method.

The goal is to stop the iterations when $F^n = \mathbf{R}u^n$ is satisfactorily similar to r . If the iteration routine could run for an infinite amount of time, one can imagine that the exact solution would be obtained. In practice, if many iterations are done (n is large), a oscillatory behavior of the solution is observed

[62]. The algorithm should be stopped when the difference between the folded solution F^n and the measured spectra r is within the experimental uncertainty. This criterium is reached quite fast, i.e., the method converges quickly and the number of iterations is usually set to be $n = 10$ [62].

For every iteration, a ‘goodness’ parameter is calculated by measuring an average of the fluctuations between the channels in addition to a χ^2 test [58]. In this way, the final unfolded spectrum u can be chosen automatically as the solution with the best ‘goodness’ parameter.

4.1.2 The Compton subtraction method

The unfolded spectrum u contains large fluctuations from channel to channel, even if the iterations are stopped early ($n \sim 10$). This noise is introduced by the unfolding method and is not associated with any physical significance. To minimize this noise, one solution is to smooth out the unfolded spectra to remove the undesirable fluctuations. As pointed out by Guttormsen et al. [62], this approach might lead to the misinterpretation of oscillations as physical peaks. After smoothing it is impossible to tell the difference between a full energy peak with few counts, and a smoothed fluctuation bump.

A better approach proposed by Guttormsen et al. [62] is the Compton subtraction method utilized in this work. Unlike the ‘blind’ smoothing of the spectra, the Compton subtraction method uses physical arguments to improve the reliability of the solution. The idea is to first use the unfolding method to account for the response of the detector, i.e., to redistribute counts corresponding to Compton, single and double escape and annihilation effects back into the full energy peak. Then, an estimate of the smoothed Compton contribution to the folded spectrum is made, before it is subtracted from the original unfolded spectrum. In this way, a full energy spectrum containing the true, experimental fluctuations is obtained.

First, u^{10} is calculated with the folding iteration method ($n = 10$). Then, $u_0 = u^{10}$ is set as the starting point for the Compton subtraction method. Taking into account the various ways a γ ray may interact with the detector, the spectrum:

$$v(i) = p_f(i)u_0(i) + w(i) \quad (4.3)$$

is defined where i is the channel number and p_f the probability for the full-energy peak. The spectrum v contains only the full energy spectrum ($p_f u_0$), single (u_s) and double (u_d) escape and the annihilation (u_a) peaks, defining w as:

$$w(i) = u_s + u_d + u_a, \quad (4.4)$$

calculated by using the known probability for the separate physical processes, i.e., the response described in the previous section. A spectrum including only

the Compton scattering can be defined by using the spectrum that does not include any Compton contribution at all; $v(i)$, and subtract from the experimental spectrum:

$$c(i) = r(i) - v(i), \quad (4.5)$$

where r is the ‘raw’ experimental spectrum. The Compton spectrum c contains at this point strong oscillations due to the dependence on the unfolded spectrum u_0 through v .

The fundamental idea of the method presented by [62] can be summarized as: *The Compton spectrum $c(i)$ should be a slowly varying function of energy. Therefore, a strong smoothing may be applied to the Compton spectrum without loss of any physical significant features.* Using this assumption, the spectrum w and the strongly smoothed Compton spectrum¹ c can be subtracted from the raw spectrum:

$$u(i) = [r(i) - c(i) - w(i)]/p_f(i), \quad (4.6)$$

where p_f account for the probability of the full-energy peak. Afterwards, the varying efficiency as a function of γ -ray energies are corrected for:

$$U(i) = u(i)/\epsilon_{tot}(i), \quad (4.7)$$

obtaining the unfolded spectrum U without the unwanted oscillations observed in u_0 . The Compton subtraction method outlined in this section have been tested at the OCL with the CACTUS setup and have been proved to work well, see [62, 65] for more information.

In Figure 4.1 (left) the unfolded matrix obtained after running the unfolding procedure is presented. Compared to the coincidence matrix in Figure 3.13, the number of counts are increased due to the redistributing of counts by the unfolding method and correction for efficiency. The next step in the Oslo method is to obtain a matrix containing the primary γ rays in Figure 4.1 (right), see next section.

¹ Modern simulation tools such as the simulation tool Geant4 [64] may be applied to estimate c directly. This is very relevant for the new and upgraded OSCAR detector setup (see chapter 6). Such numerical tools have not been implemented for the present experimental setup.

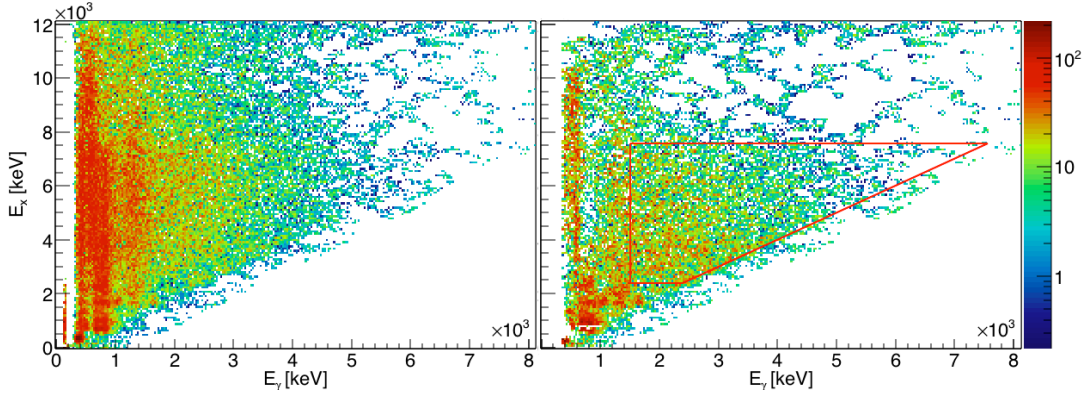


Figure 4.1: **Left:** The unfolded coincidence matrix, the excitation energy E_x of ^{192}Os versus the γ -ray energy. The number of counts are represented by the color scale. **Right:** The first-generation matrix. The red lines represent the limits included in the χ^2 -minimization method in subsection 4.3.1.

4.2 Extracting the first-generation γ -rays

Given the time resolution of the experimental setup, it is not possible to distinguish a γ ray emitted directly after population and for example the second γ -ray in a two-step transition. The first and the second γ ray emitted in a cascade arrives within the same time-slot. To obtain the proper transition probabilities (next section) a first-generation, or primary, γ -ray spectrum must be identified.

The premise of the first-generation method proposed by [66] reads: *States populated directly by the nuclear reaction have the same decay properties as states populated by γ decay from higher lying-states.* This assumption implies that the decay routes of a γ ray from a level at an excitation-energy bin is independent of how the nucleus was excited to this bin. The shape of the γ -ray spectra involving states populated by the nuclear reaction is identical to the spectra created by states populated by higher-lying energy states.

Figure 4.2 present a simplified illustration of the possible paths, or cascades, a γ ray can take from an excited state (E_3) to the ground state (g.s.). An unfolded spectrum of this example nucleus would contain all of the transitions a, b, c, d, e and f. The energy level E_1 can be populated directly, or by states lying above. There are several cascades leading to the emission of a γ ray with energy E_1 , observed as transition f. Only one of the cascades in the figure includes a primary γ ray f, i.e., the first emitted γ ray in the cascade with energy E_1 .

If a gate in excitation energy is set at E_3 , the γ spectrum would contain all of the transitions a, b, c, d, e and f. Similarly, a gate set at E_2 would result in a γ spectrum containing the transitions d, e and f, while a gate at E_1 only the f transition. Turning the argument, all transitions starting from the levels below E_3 contain exactly the secondary transitions in the cascades starting from E_3 .

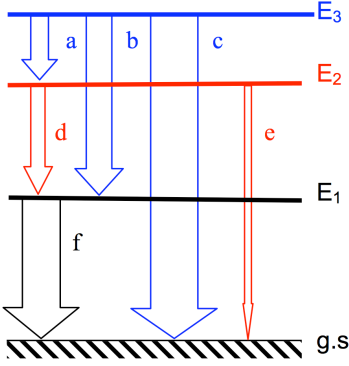


Figure 4.2: An illustration of the possible paths a photon emitted from an excited state can take to the ground state, taken from [65].

Therefore, the primary γ rays from level E_3 can be obtained by subtracting the sum of the transitions from the underlying levels E_2 and E_1 .

The simplified illustration presented above can be generalized into an iterative subtraction method. The unfolded spectra² u_i for a given excitation energy bin i consist of all generations of γ rays from all possible decay cascades starting at bin i . Then, the sum of all spectra u_j at excitation energy bins j with $j < i$ contains the same γ transitions as u_i except for the primary γ rays. The primary γ -ray spectrum h_i for each excitation energy bin i is found by:

$$h_i = u_i - g_i, \quad (4.8)$$

where g_i is a weighted sum of all spectra beneath bin i :

$$g_i = \sum_{j < i} n_{ij} w_{ij} u_j \quad (4.9)$$

The weighting factors w_{ij} and n_{ij} are introduced to take two effects into account. Firstly, the probability for a γ ray to take a specific path going from level i to all possible levels j are not necessarily identical to the probability of the other paths. In other words, w_{ij} contains the branching ratios for a given excitation level with the normalization $\sum_j w_{ij} = 1$. In fact, w_{ij} are the unknowns of Equation 4.8 as the weighting function w_i corresponds directly to the primary γ -ray spectrum h_i for bin i [65].

Secondly, the cross section for populating levels within bin i may not be the same as the cross section for the underlying levels in bin j . The coefficients

²Note: To have a consistent notation throughout the chapter, a notation deviating from the main references [65, 66] have been applied.

n_{ij} are determined so that the total area of each spectrum u_i multiplied by n_{ij} corresponds to the same number of cascades. Then, the n_{ij} factors can be found by the following two normalization methods[65, 66]:

a) Singles normalization. The singles-particle spectrum³ is proportional to the number of times a given level in excitation energy bin i is populated. Therefore this spectrum is also proportional to the number of cascades starting from bin i . The singles spectrum, or the population cross section in arbitrary units for bin i and j are denoted as S_i and S_j , respectively. Then the normalization factor n_{ij} applied in Equation 4.9 is given by:

$$n_{ij} = \frac{S_i}{S_j}. \quad (4.10)$$

b) Multiplicity normalization. If an excited level is populated N times, a decay from this level will result in N γ -ray cascades. Then, the multiplicity, or the number of γ rays emitted from the k th cascade, is M_k . The average γ -ray energy $\langle E_{\gamma,i} \rangle$ from bin i is equal to the total energy carried by the γ rays divided by the total number of γ rays:

$$\langle E_{\gamma,i} \rangle = \frac{NE_i}{\sum_{k=1}^N M_k} = \frac{E_i}{\frac{1}{N} \sum_{k=1}^N M_k} = \frac{E_i}{\langle M_i \rangle} \quad (4.11)$$

so that the average γ -ray multiplicity for an excitation-energy bin i can be defined:

$$\langle M_i \rangle = \frac{E_i}{\langle E_{\gamma,i} \rangle}. \quad (4.12)$$

The area of the γ -ray spectrum u_i , denoted by $A(u_i)$, is equal to the total number of counts in the histogram. Noting that $A(u_i)/\langle M_i \rangle$ is proportional to the singles-particle cross section S_i and using Equation 4.12, the coefficients n_{ij} can be calculated as:

$$n_{ij} = \frac{A(u_i)/\langle M_i \rangle}{A(u_j)/\langle M_j \rangle} = \frac{A(u_i)\langle M_j \rangle}{A(u_j)\langle M_i \rangle} = \frac{A(u_i)\langle E_{\gamma,i} \rangle E_j}{A(u_j)\langle E_{\gamma,j} \rangle E_i} \quad (4.13)$$

According to [65] the two normalization methods give the same results within the experimental error bars. The multiplicity normalization method (b) is convenient to apply, while the singles normalization (a) is not as appealing to implement numerically. In this work the multiplicity normalization method have been employed. A summary of the steps are given below:

³The spectrum obtained by using the particle detectors only, i.e., counting the number of times the target nucleus are left in a specific excitation energy.

1. Apply a trial function w_{ij} .
2. Deduce h_i from Equation 4.8.
3. Transform h_i to w_{ij} by giving h_i the same energy calibration as w_{ij} , and normalize the area of h_i to unity.
4. If $w_{ij}(\text{new}) \approx w_{ij}(\text{old})$, convergence is reached and the procedure is finished.
Otherwise repeat from step 2.

The first trial function in step 1 can in principle be any function, i.e., the unfolded spectrum u_i , a constant or a theoretical estimate. It turns out that the resulting first-generation spectra h_i are not sensitive to the starting trial function[65]. The method has been shown to converge fast [66] within 10-20 iterations performed on the experimental spectra [65].

Figure 4.1 (right) shows the first generation matrix, or the decay probability of ^{192}Os for a given excitation energy and γ -ray energy, obtained after running the iteration method presented above. The first generation matrix includes less counts than the unfolded matrix since all counts corresponding to secondary γ rays have been excluded.

If the multiplicity is well defined, it is possible to apply an area consistency test to Equation 4.8 [66]. The total counts, or the area of the primary γ -ray spectrum $A(h_i)$ should be equal to the area of the unfolded spectrum $A(u_i)$ minus the area of the underlying spectra $A(g_i)$. The choice of the unknown weights w_{ij} may introduce an inaccuracy that can be corrected for by introducing a factor δ , close to unity. Applying Equation 4.8 to the total counts in the spectra and substituting $A(g_i)$ by $\delta A(g_i)$ provides:

$$A(h_i) = A(u_i) - \delta A(g_i). \quad (4.14)$$

The total number of primary γ rays for excitation-energy bin i can also be calculated by dividing the total number of unfolded γ rays by the multiplicity:

$$A(h_i) = \frac{A(u_i)}{\langle M_i \rangle}. \quad (4.15)$$

An expression for the correction factor can be obtained by combining both relations for $A(h_i)$:

$$\delta = \left(1 - \frac{1}{\langle M_i \rangle}\right) \frac{A(u_i)}{A(g_i)} \quad (4.16)$$

The δ parameter may be varied to get the best agreement of the areas (Equation 4.14), but the correction should not exceed 15% [65]. If a larger compensation is needed the choice of the weighting functions should be improved.

4.3 Determining the nuclear level density and the γ -strength function

The next step of the Oslo method is to obtain the general NLD and the γ SF by means of a χ^2 -method, as outlined in subsection 4.3.1. As the final step of the Oslo-framework, the normalization procedure utilized to obtain the physical solution of the NLD and γ SF will be introduced in subsection 4.3.2.

4.3.1 The χ^2 -minimization iteration method

The method applied to extract the NLD and γ SF can be motivated as follows. Consider a single transition from one initial level, or energy eigenstate, i to a final level f . The final level f has an energy E_f and lies in a continuum of states with a level density $\rho(E_f)$. The transition rate λ , or the probability of transition per unit time can be described by *Fermi's golden rule* [67, 68]:

$$\lambda_{i \rightarrow f} = \frac{2\pi}{\hbar} |\langle f | \hat{H}_{int} | i \rangle|^2 \rho(E_f) \quad (4.17)$$

where \hat{H}_{int} is the operator describing the interaction leading to the transition. This expression factorizes the decay probability into the transition matrix element between the initial and final states, and the level density at the final state.

Closely following the arguments of [69], our attention is turned to the measurable quantities: the level density and the γ -ray transition coefficient. The first generation spectra contain information about transition probabilities from several initial levels, within an excitation energy bin. Using Equation 4.17, the resemblance between the first generation spectra $P(E_x, E_\gamma)$ and the decay probability $\lambda_{i \rightarrow f}$ suggests the factorization:

$$P(E_x, E_\gamma) \propto \mathcal{T}_{i \rightarrow f} \rho(E_f), \quad (4.18)$$

where $\mathcal{T}_{i \rightarrow f}$ is the γ -ray transmission coefficient from state i to f and $\rho(E_f) = \rho(E_x - E_\gamma)$ is the level density at the excitation energy E_f after the emission of a primary γ ray.

According to the Brink hypothesis [70]; *the γ -ray transmission coefficient is only dependent on the γ -ray energy, i.e., independent of excitation energy*. Assuming that the Brink hypothesis holds we can replace $\mathcal{T}_{i \rightarrow f}$ with $\mathcal{T}(E_\gamma)$ leading to [71]:

$$P(E_x, E_\gamma) = \frac{\mathcal{T}(E_\gamma) \rho(E_x - E_\gamma)}{\sum_{E_\gamma=E_\gamma^{min}}^{E_x} \mathcal{T}(E_\gamma) \rho(E_x - E_\gamma)} \quad (4.19)$$

The first-generation matrix is normalized so that the sum over all γ -ray energies in the range $E_\gamma^{\min} \leq E_\gamma \leq E_\gamma^{\max}$ is unity, for a given excitation energy bin E_x :

$$\sum_{E_\gamma=E_\gamma^{\min}}^{E_x} P(E_x, E_\gamma) = 1, \quad (4.20)$$

where E_γ^{\min} and E_γ^{\max} is the minimum and maximum γ -ray energy included in the analysis.

An iterative method applied to the first generation matrix $P(E_x, E_\gamma)$ have been developed by Schiller et al. [71] to extract the functions $\mathcal{T}(E_\gamma)$ and $\rho(E_x - E_\gamma)$. The method is designed to minimize:

$$\chi^2 = \frac{1}{N_{\text{free}}} \sum_{E_i=E_x^{\min}}^{E_x^{\max}} \sum_{E_\gamma=E_\gamma^{\min}}^{E_\gamma^{\max}} \left(\frac{P(E_i, E_\gamma) - P_{\text{exp}}(E_i, E_\gamma)}{\Delta P_{\text{exp}}(E_i, E_\gamma)} \right)^2, \quad (4.21)$$

where N_{free} is the number of degrees of freedom and $\Delta P_{\text{exp}}(E_x, E_\gamma)$ is the uncertainty in the experimental first generation matrix $P_{\text{exp}}(E_x, E_\gamma)$. Minimizing χ^2 with respect to \mathcal{T} at every E_γ bin, and with respect to ρ at every excitation energy bin:

$$\frac{\partial}{\partial \mathcal{T}(E_\gamma)} \chi^2 = 0 \quad \text{and} \quad \frac{\partial}{\partial \rho(E_x - E_\gamma)} \chi^2 = 0, \quad (4.22)$$

allows the simultaneous extraction of $\mathcal{T}(E_\gamma)$ and $\rho(E_x - E_\gamma)$ [71]. Then, the following procedure can be performed. First, set $\rho^{(0)} = 1$ and deduce $\mathcal{T}^{(0)}$ by summing Equation 4.19 over the excitation energy interval $E_x^{\min} \leq E_x \leq E_x^{\max}$ while obeying $E_x \geq E_\gamma$:

$$\mathcal{T}^{(0)} = \sum_{E_i=E_x^{\min}}^{E_x^{\max}} P_{\text{exp}}(E_i, E_\gamma)$$

Then, for $n = 0, 1, 2, \dots$:

1. Calculate the next order estimate $\rho^{(n+1)}$ and $\mathcal{T}^{(n+1)}$ by means of the previous estimates $\rho^{(n)}$ and $\mathcal{T}^{(n)}$ (equations given in [71])
2. Calculate $P^{(n+1)}(E_x, E_\gamma)$ by inserting $\rho^{(n+1)}$ and $\mathcal{T}^{(n+1)}$ into Equation 4.19
3. Calculate $\chi^{(n+1)}$ by inserting $P^{(n+1)}(E_x, E_\gamma)$ into Equation 4.21
4. Stop if $\chi^{(n+1)}$ is at the minimum, yielding $\rho^{(n+1)}$ and $\mathcal{T}^{(n+1)}$ as the solution of the iteration method, else start over from 1.

The iteration method usually converges fast [71]. A restriction on the maximum and minimum change of χ^2 per iteration haas been introduced to handle

the cases where the χ^2 -minimum is very shallow, so that the global minimum is found. For further details see [71]. The source codes developed at the OCL for analysis purposes can be found in [57, 58].

The limits E_γ^{min} , E_x^{min} and E_x^{max} are chosen to ensure that the data employed in the analysis stem from the statistical excitation energy region in the first-generation matrix $P(E_x, E_\gamma)$. The maximum excitation energy is set to the neutron separation energy $E_x^{max} = 7.558$ MeV (explained in subsection 3.2.5). The low energy part of the matrix is excluded by the strict $E_\gamma^{min} = 1.5$ MeV limit applied and $E_x^{min} = 2.4$ MeV. Higher and lower values of E_x^{min} do not change the results significantly, i.e., the extraction is not sensitive to the choice of E_x^{min} . The section of the first-generation matrix P included in the χ^2 -minimization method is contained by the red lines in Figure 4.1 (right).

Now, the solutions $\rho^{(n+1)}$ and $\mathcal{T}^{(n+1)}$ obtained in the iteration method above are not the final result of the NLD and γ SF. These functions contain the general shape and the functional form, i.e., they are the general solution of Equation 4.19. The special, or physical solutions are found by constraining the functions by external data, see the next section.

4.3.2 The normalization procedure

If one solution $\mathcal{T}(E_\gamma)$ and $\rho(E_f)$ of Equation 4.19 is known, it can be mathematically shown [71] that there exists an infinite set of solutions given by the transformation:

$$\tilde{\rho}(E_x - E_\gamma) = A \exp[\alpha(E_x - E_\gamma)] \rho(E_x - E_\gamma) \quad (4.23)$$

$$\tilde{\mathcal{T}}(E_\gamma) = B \exp[\alpha E_\gamma] \mathcal{T}(E_\gamma) \quad (4.24)$$

Any combination of values A , B and α will yield solutions $\tilde{\rho}$ and $\tilde{\mathcal{T}}$ obeying:

$$P(E_x, E_\gamma) = \frac{\tilde{\mathcal{T}}(E_\gamma) \tilde{\rho}(E_x - E_\gamma)}{\sum_{E_\gamma=E_\gamma^{min}}^{E_x} \tilde{\mathcal{T}}(E_\gamma) \tilde{\rho}(E_x - E_\gamma)} \quad (4.25)$$

Since the general solution of the NLD and γ SF are known through the χ^2 -minimization procedure explained the previous section, the remaining problem is to attain the physical solution determined by the parameters A , α , and B . These parameters are acquired separately for the NLD and γ SF.

Normalization of the level density

The absolute value A and the slope α of the level density ρ is determined by: 1) normalization to the number of known discrete levels at low excitation energy, and 2) the estimated level density at the neutron separation energy, $\rho(S_n)$.

To calculate $\rho(S_n)$ the spin and parity distributions of the level density at S_n have to be known. These quantities are model dependent, introducing a potentially large uncertainty in the normalization procedure. In this work, only the constant-temperature (CT) formula (Equation 2.8) is considered. The CT formula assumes an equiparity distribution, i.e., that both parities contribute equally to the level density and yields the spin distribution [42]:

$$g(E_x, I) \simeq \frac{2I + 1}{2\sigma^2(E_x)} \exp[-(I + 1/2)^2/2\sigma^2(E_x)], \quad (4.26)$$

for a specific excitation energy E_x and spin I . Following the approach of [72], the energy dependent spin cutoff parameter is introduced as:

$$\sigma^2(E_x) = \sigma_d^2 + \frac{E_x - E_d}{S_n - E_d} [\sigma^2(S_n) - \sigma_d^2], \quad (4.27)$$

going through two anchor points σ_d^2 and $\sigma^2(S_n)$ at the energy E_d and S_n , respectively. The known discrete levels at the excitation energy $E_x = E_d$ is used to create an experimental spin distribution determining the first point σ_d^2 . Assuming a rigid moment of inertia $\Theta = 0.0146A^{5/3}$, the second point at $E_x = S_n$ can be estimated [73]:

$$\sigma^2(S_n) = 0.0146A^{5/3} \frac{1 + \sqrt{1 + 4aU_n}}{2a}, \quad (4.28)$$

where A is the mass number, $U_n = S_n - E_1$ is the intrinsic excitation energy and the level parameter a and the energy shift parameter E_1 is determined according to [73].

The level density at the neutron separation energy S_n can be calculated from the spacing of neutron s-wave ($\ell = 0$) resonances D_0 following (n, γ) capture [71]

$$\rho(S_n) = \frac{2\sigma^2}{D_0} \frac{1}{(I + 1) \exp[-(I + 1)^2/2\sigma^2] + I \exp[-I^2/2\sigma^2]}, \quad (4.29)$$

Here, the spin cutoff parameter σ from Equation 4.27 is implemented and I is the ground-state spin of the target nucleus in the (n, γ) reaction, i.e., $9/2^-$ for ^{191}Os .

Normalization of the γ -ray transmission coefficient

The shared slope α of the level density ρ and the transmission coefficient \mathcal{T} was found in the previous subsection through the normalization of ρ . The parameter B , which gives the absolute normalization of \mathcal{T} , is the only remaining unknown of Equation 4.24. This parameter can be constrained by the known average, total

radiative width $\langle \Gamma_{\gamma 0} \rangle$ at S_n from neutron resonance decay experiments:

$$\langle \Gamma_{\gamma 0}(S_n) \rangle = \frac{1}{2\pi\rho(S_n, I, \pi)} \sum_{I_f} \int_0^{S_n} dE_\gamma \mathcal{T}(E_\gamma) \rho(S_n - E_\gamma, I_f). \quad (4.30)$$

The summation and integration runs over all final levels with spin I_f , that are accessible by $E1$ and $M1$ transitions with energy E_γ , i.e., assuming dipole radiation ($L = 1$). Then, the transmission coefficient \mathcal{T} can be transformed into the γ -strength function f by using Equation 2.10.

As we will see in the next chapter, none of the required parameters for the normalization of the NLD and γ SF are available for ^{192}Os . Therefore, these variables have to be estimated through systematics, which introduce an additional uncertainty in the NLD and γ SF obtained in this work. The parameters and the uncertainty estimate of the normalization procedure for ^{192}Os will be discussed in great detail together with the presented results in the next chapter.

Chapter 5

Results and discussion

“Of course it is happening inside your head, Harry, but why on earth should that mean it is not real?”

— Albus Dumbledore, Harry Potter and the Deathly Hallows

The current work is motivated by the need for experimental nuclear data in order to explain the synthesis of elements heavier than iron, as outlined in chapter 2. In particular, the s-process relies on a series of consecutive neutron captures and β -decays, requiring the knowledge of (n, γ) cross sections.

In chapter 3 the $^{192}\text{Os}(\alpha, \alpha'\gamma)^{192}\text{Os}$ experiment performed in the present work was reviewed. After the completion of the detector calibration, the coincidence matrix was obtained, providing the starting point of the Oslo method explained in chapter 4. Following, the particle- γ -ray spectra was unfolded in section 4.1, before the primary γ rays were extracted by the first generation method in section 4.2. Finally, the method to extract the NLD and γ SF of ^{192}Os was introduced in section 4.3.

In this chapter, a careful error estimate of the normalization parameters of the NLD and γ SF will be performed in section 5.1. Then, the final NLD, γ SF and MACS results will be compared to a few models, external data and theoretical values in section 5.2, 5.3 and 5.4, respectively.

5.1 Obtaining the normalization parameters

Starting out from the first generation matrix of ^{192}Os (section 4.2), the general shape of the NLD and γ SF is determined through the χ^2 -minimization iteration, and then the physical solution is obtained by means of the normalization procedure introduced in section 4.3.

Often, the experimental parameters required by the normalization technique are known, and the procedure can be performed in a straightforward manner. In such cases, the uncertainty of the normalization is introduced by the model

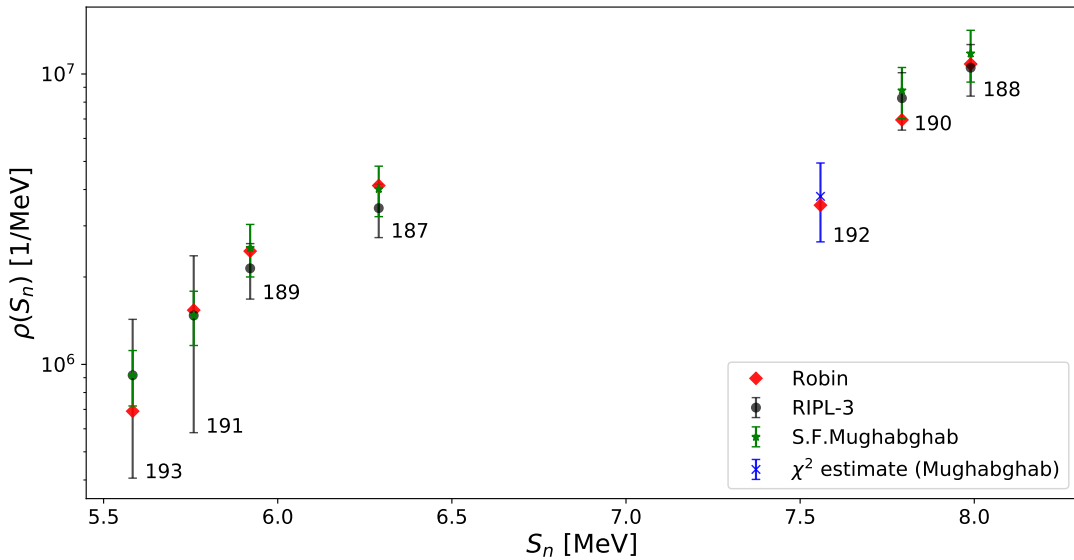


Figure 5.1: The level density at the separation energy $\rho(S_n)$ plotted against the neutron separation energy S_n . The mass numbers A are annotated next to the data points. The values are calculated from D_0 values (RIPL-3 [46], Mughabghab [74]) and by the OCL ‘Robin’ software [58].

dependence of the parameter determination, and the uncertainty of the experimental values applied.

As mentioned previously, no experimental normalization parameters are known for ^{192}Os , introducing an additional uncertainty in the normalized solutions for the NLD and γSF . This error will propagate to the calculated MACS value. Therefore, an error estimate is of utmost importance in order to quantify the significance of the results obtained.

5.1.1 The level density parameters

In order to normalize the level density of ^{192}Os , the level density at the neutron separation energy $\rho(S_n)$ must be calculated by means of Equation 4.29, i.e., the D_0 parameter needs to be known. Unfortunately, no tabulated D_0 values are available for ^{192}Os , and an estimation is done by using available values from neutron resonance experiments of isotopes in the same mass region.

In Figure 5.1, $\rho(S_n)$ values for all available osmium isotopes are presented. The experimental D_0 values for $A = 187 - 193$ (except 192) are taken from [74]¹ (green) and [46] (black) and transformed into $\rho(S_n)$ values by means of

¹The new, updated version of this atlas [75] (available February, 2018) was not included in this work.

Table 5.1: Parameters used to extract the level density within the CT model approach, in addition to the level-density parameter a and back-shift E_1 for the Fermi-gas model in [73].

a [MeV $^{-1}$]	E_1 [MeV]	E_d [MeV]	σ_d	T_{CT} [MeV]	E_0 [MeV]
18.472	0.328	1.1	2.8	0.5	0.331

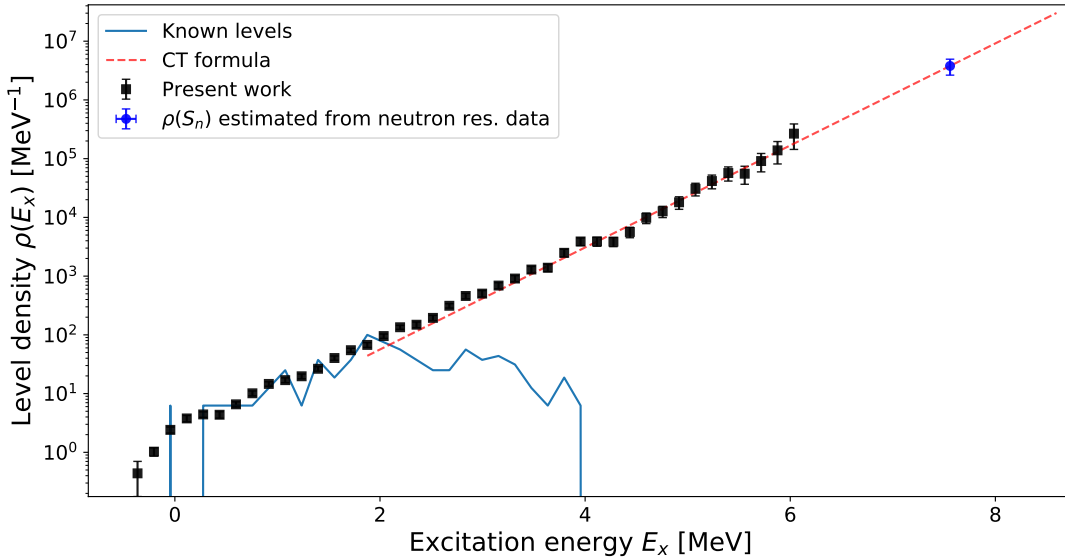


Figure 5.2: The level density versus excitation energy for the Oslo data (black). The CT interpolation between the data and $\rho(S_n)$ (blue) is indicated by a red line in addition to the known levels (light blue).

Equation 4.29. The theoretical, or systematic values (red) are calculated by the OCL ‘Robin’ software [58], using the same formalism as for the experimental values [73] and the global parameterization given in [76].

A χ^2 -minimization was done to estimate the level density at the neutron separation energy for ^{192}Os by using the experimental values provided by [74]. The appropriate scaling factor b between the ‘Robin’ values $\rho_{theory}(S_n)$ and the values provided by [74] was found by minimizing:

$$\chi^2 = \sum_A \frac{(b \cdot \rho_{theory}(S_n) - \rho_{exp}(S_n))^2}{\Delta\rho_{exp}^2(S_n)} \quad (5.1)$$

where $\Delta\rho_{exp}(S_n)$ is the listed uncertainty for the experimental points [74] and the sum runs over $A \in [187, 188, 189, 190, 191, 193]$.

A rough error estimate of the resulting $\rho(S_n)$ point for ^{192}Os (blue in Figure 5.1) was done by taking the largest uncertainty of the experimental points

Table 5.2: The high (H), recommended (R) and lower (L) estimates of the parameters used in the normalization procedure of the level density and the γ -strength function. *Notice that the low (high) D_0 values correspond to the high (low) $\rho(S_n)$ values.*

	D_0 [eV]	$\rho(S_n) \times 10^6$ [MeV $^{-1}$]	$\sigma(S_n)$	$\langle \Gamma_{\gamma 0} \rangle$ [meV]
H	5.25	4.94	7.81	107
R	3.66	3.79	7.41	79
L	2.81	2.64	6.98	61

[74] and adding a 40% relative error. Considering the spread of D_0 values in the literature, 40% is a conservative estimate chosen to rather overestimate the uncertainty than underestimate it. This error analysis leads to the lower (L), recommended (R) and higher (H) estimates for the level density at the neutron separation energy listed in Table 5.2.

The second unknown of Equation 4.29 to obtain the normalization of ρ is the spin-cutoff parameter, calculated by means of Equation 4.27 and 4.28. The applied parameters to obtain the spin-cutoff parameter can be found in Table 5.1.

Following [72], a systematic error band can be created by multiplying the rigid moment of inertia $\Theta = 0.0146A^{5/3}$ of Equation 4.28 with a factor η . In this way, the lower (L), recommended (R) and higher (H) estimates of the spin cutoff parameter listed in Table 5.2 can be introduced by letting $\eta \in [0.8, 0.9, 1.0]$, respectively.

In Figure 5.2, the level density (black) obtained by using the recommended parameters listed in Table 5.2 is presented. The experimental data only reach up to $\sim S_n - 1.5$ MeV, so an interpolation between the Oslo data and $\rho(S_n)$ (blue) is done using the CT level density (red). The slope of the experimental level density is found by forcing the level density to fit the discrete levels, at $E_x = 116$ keV and $E_x = 1236$ keV, in addition to the CT interpolation between $E_x = 3156$ keV and $E_x = 6036$ keV. The CT model parameters of Equation 2.8 is listed in Table 5.1.

The uncertainties presented by the black data points are statistical errors in addition to systematic errors from the unfolding and first generation method. These errors are estimated by the Oslo software as described in [71] and will from this point on only be referred to as statistical.

5.1.2 The γ -ray transmission coefficient parameters

The normalization of the γ SF is done by requiring the integral in Equation 4.30 to be equal to the average, total radiative width $\langle \Gamma_{\gamma 0} \rangle$ at S_n from neutron resonance decay experiments.

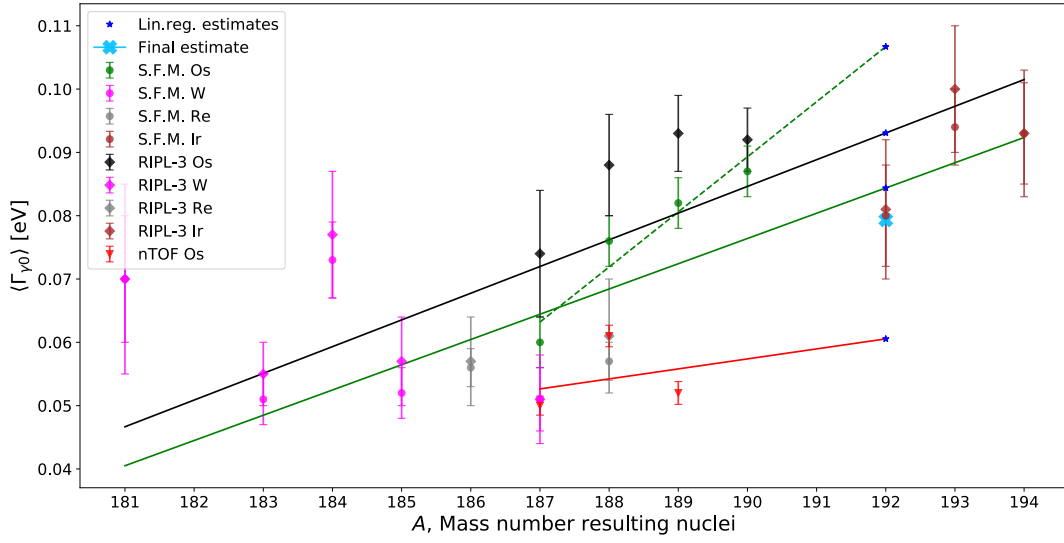


Figure 5.3: The average radiative widths $\langle \Gamma_{\gamma 0} \rangle$ at S_n plotted against mass number A for osmium (green/black), tungsten (magenta), rhenium (gray) and iridium (brown). The data is collected from RIPL-3 [46] (diamond), Mughabghab et al. [74] (circle) and the n_TOF collaboration [77] (triangle). The $\langle \Gamma_{\gamma 0} \rangle$ value for ^{192}Os has been estimated through multiple weighted linear regressions, setting the weights to the inverse of the uncertainty of the points. The black solid line is a linear regression of the RIPL-3 values, the green solid line of all the Mughabghab values, the red solid line of the n_TOF values and the green dotted line of only the osmium points from Mughabghab.

Experimental $\langle \Gamma_{\gamma 0} \rangle$ values are not available for ^{192}Os , because ^{191}Os is unstable. Therefore, the $\langle \Gamma_{\gamma 0} \rangle$ value at S_n has been estimated through a weighted linear regression of the values presented in Figure 5.3. The average, radiative widths are plotted against mass number A for available osmium isotopes in addition to the neighboring isotopes tungsten, rhenium and iridium.

An inconsistency between the $\langle \Gamma_{\gamma 0} \rangle$ values collected from RIPL-3 [46], the n_TOF collaboration [77] and Mughabghab [74] is revealed for the osmium isotopes in Figure 5.3. To investigate the discrepancy, a linear regression on the separate data sets was performed leading to a lower (L) and a higher (H) estimate of the $\langle \Gamma_{\gamma 0} \rangle$ value for ^{192}Os displayed in Table 5.2. The lower estimate is calculated through an extrapolation using the n_TOF values (red solid line) and the higher estimate is provided by an extrapolation using the osmium values from Mughabghab et al. (green dotted line).

In addition, the osmium data points display a different trend than the isotopes in the same mass region. Another estimate is therefore calculated through a linear regression of all RIPL-3 $\langle \Gamma_{\gamma 0} \rangle$ values (black solid line), and another by using all of the values provided by Mughabghab (green solid line) displayed in Figure 5.3.

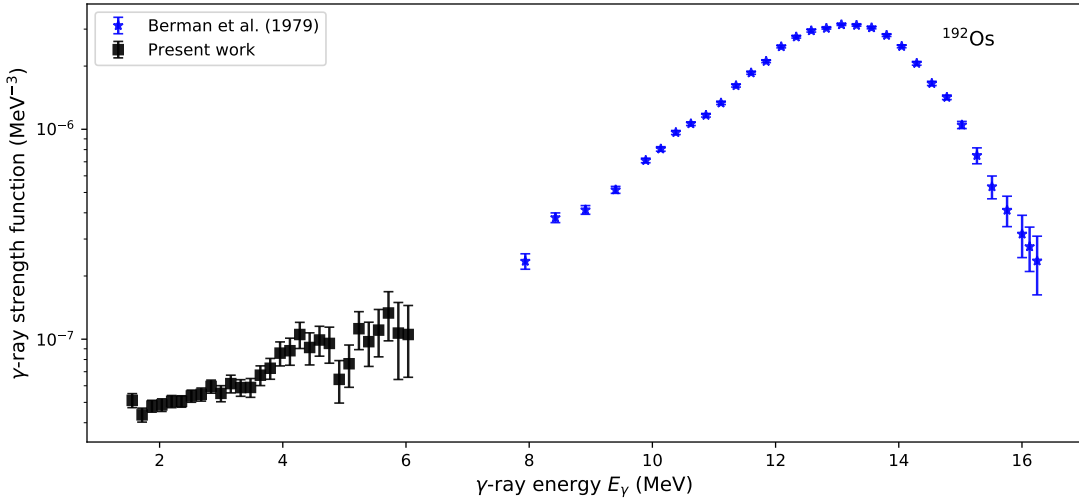


Figure 5.4: The γ -strength function (black) versus γ -ray energy obtained using the recommended $\langle \Gamma_{\gamma 0} \rangle$ value at S_n . In addition, (γ, n) data (blue) from [78] is presented.

The final estimate, or the ‘recommended’ value (light blue cross) is calculated as the mean of the $\langle \Gamma_{\gamma 0} \rangle$ values (blue points) obtained through the four approaches mentioned above.

Using Equation 2.10, the normalized transmission coefficient \mathcal{T} is transformed into the γ SF. In Figure 5.4, the γ SF obtained using the recommended $\langle \Gamma_{\gamma 0} \rangle$ value at S_n (see Table 5.2) is displayed together with (γ, n) data from [78]. As for the level density, the uncertainties presented are statistical errors and systematic errors of the unfolding and first-generation method [71], denoted ‘statistical’ errors from this point on. An estimate of the systematic errors introduced by the normalization parameters will be performed in the next subsection.

5.1.3 Systematic error estimate

The Oslo method software [58] propagates the statistical errors in the analysis, but it does not take into account the systematic errors introduced by the choice of normalization parameters. In this work, the D_0 , $\rho(S_n)$, $\sigma(S_n)$ and $\langle \Gamma_{\gamma 0} \rangle$ values in Table 5.2 were varied to obtain a systematic uncertainty band for the NLD and γ SF. The D_0 and the $\rho(S_n)$ values are correlated, using the lower D_0 value implies using the higher $\rho(S_n)$ value. In principle, there are only three normalization parameters to vary, i.e., $\sigma(S_n)$, $\langle \Gamma_{\gamma 0} \rangle$ and D_0 or $\rho(S_n)$.

The standard deviation of the level density STD_ρ due to systematic and

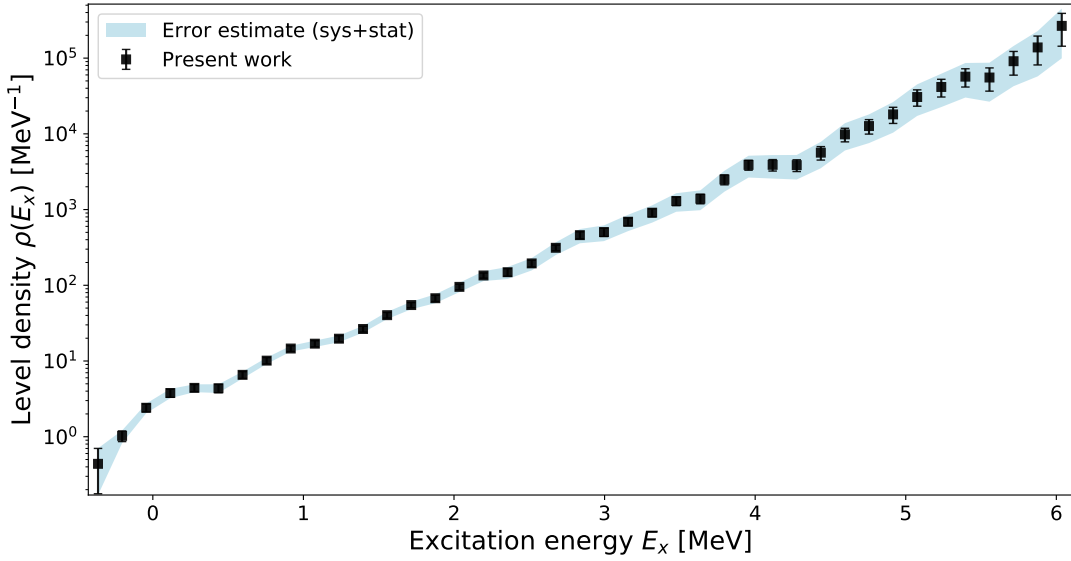


Figure 5.5: The level density versus excitation energy for the Oslo data (black). The systematic uncertainties combined with the statistical errors are presented as the light-blue colored band.

statistical errors was split into:

$$STD_{\rho,high}^2 = \rho_{rec}^2 \left[\left(\frac{\rho_{D_0,low} - \rho_{rec}}{\rho_{rec}} \right)^2 + \left(\frac{\rho_{\sigma,high} - \rho_{rec}}{\rho_{rec}} \right)^2 + \left(\frac{\Delta\rho_{rec}}{\rho_{rec}} \right)^2 \right], \quad (5.2)$$

and

$$STD_{\rho,low}^2 = \rho_{rec}^2 \left[\left(\frac{\rho_{D_0,high} - \rho_{rec}}{\rho_{rec}} \right)^2 + \left(\frac{\rho_{\sigma,low} - \rho_{rec}}{\rho_{rec}} \right)^2 + \left(\frac{\Delta\rho_{rec}}{\rho_{rec}} \right)^2 \right], \quad (5.3)$$

due to the asymmetric higher and lower estimates, compared to the recommended level density ρ_{rec} , listed in Table 5.2. Here, $\rho_{X,low}$ corresponds to the NLD obtained using the lower X value and $\rho_{X,high}$ corresponds to the NLD obtained using the higher X value. The statistical error of the recommended NLD is denoted as $\Delta\rho_{rec}$.

Similarly, for the γ -strength function the standard deviation due to systematic

and statistical errors STD_f was calculated as:

$$STD_{f,high}^2 = f_{rec}^2 \left[\left(\frac{f_{D_0,low} - f_{rec}}{f_{rec}} \right)^2 + \left(\frac{f_{\sigma,high} - f_{rec}}{f_{rec}} \right)^2 + \left(\frac{f_{\langle \Gamma_{\gamma 0} \rangle,high} - f_{rec}}{f_{rec}} \right)^2 + \left(\frac{\Delta f_{rec}}{f_{rec}} \right)^2 \right], \quad (5.4)$$

and

$$STD_{f,low}^2 = f_{rec}^2 \left[\left(\frac{f_{D_0,high} - f_{rec}}{f_{rec}} \right)^2 + \left(\frac{f_{\sigma,low} - f_{rec}}{f_{rec}} \right)^2 + \left(\frac{f_{\langle \Gamma_{\gamma 0} \rangle,low} - f_{rec}}{f_{rec}} \right)^2 + \left(\frac{\Delta f_{rec}}{f_{rec}} \right)^2 \right]. \quad (5.5)$$

where Δf_{rec} is the statistical error of the recommended γ SF. Hence, the higher and lower limits of the level density and γ SF are set to:

$$\rho_{high} = \rho_{rec} + STD_{\rho,high} \quad (5.6)$$

$$\rho_{low} = \rho_{rec} - STD_{\rho,low}, \quad (5.7)$$

and

$$f_{high} = f_{rec} + STD_{f,high} \quad (5.8)$$

$$f_{low} = f_{rec} - STD_{f,low}. \quad (5.9)$$

In Figure 5.5 and 5.6 the combined systematic and statistical uncertainties for the level density and the γ -strength function are displayed as a light-blue colored band. Further uncertainties in the Oslo method, i.e., stemming from the unfolding, first generation method, the Brink hypothesis, and the parity and spin distribution are investigated in [65].

5.2 The level density

In Figure 5.7, the nuclear level density versus excitation E_x energy for ^{192}Os is displayed together with two NLD models, i.e., the CT formula (red) and the HFB+ model (green). Up to ≈ 2 MeV, the discrete level scheme appears to be complete, i.e., up to this point the discrete levels follow the same trend as the present experimental level density.

A quite large total uncertainty is observed in the NLD for ^{192}Os in Figure 5.5 and 5.7, in particularly the last five data points have an uncertainty larger than 50%.

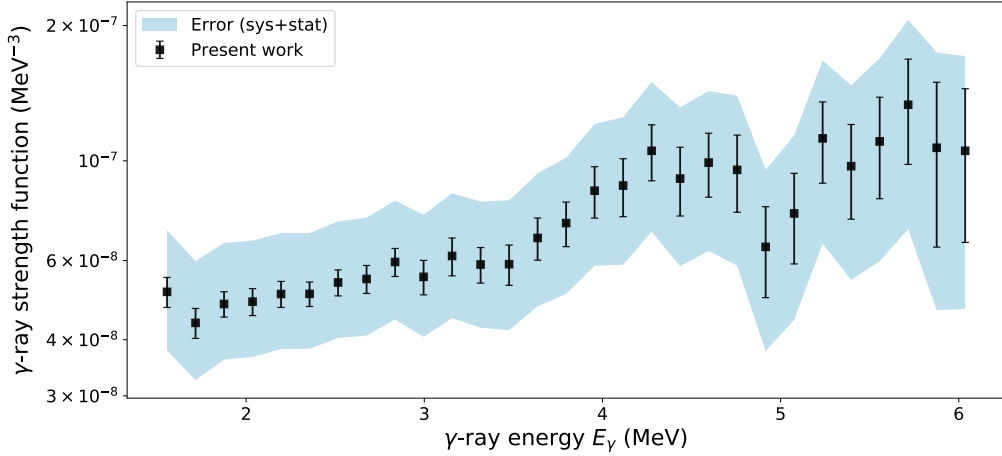


Figure 5.6: The γ -strength function (black) versus γ -ray energy for the Oslo data (black). The systematic uncertainties combined with the statistical errors are presented as the light-blue colored band.

The statistical errors displayed in black have an uncertainty of $\approx 60\%$ in the lowest- E_x data point, $\approx 9\%$ at minimum and $\approx 45\%$ at the highest- E_x data point. Similarly, the average of the high and low systematic uncertainty is $\approx 12\%$ in the lowest- E_x data point, $\approx 1\%$ at minimum and $\approx 48\%$ at the highest- E_x data point. These errors combined, i.e., the blue uncertainty band, is then about 60%. The errors calculated by the Oslo software, have approximately the same magnitude as the uncertainty introduced by the normalization parameters.

No significant large-scale structures are observed in the level density (Figure 5.7). An exponential, i.e., linear growth in the log scale is observed. This fits well with the CT formula, displayed in red, which has been adapted to go through the point at $\rho(S_n)$ in addition to the experimental level density. The HFB+ model, displayed in green, exhibits a very moderate slope of the level density compared to the Oslo data. The deviation between the NLD acquired in this work and the HFB+ model is not within the conservative uncertainty estimate obtained in this work, diverging by several orders of magnitude at high excitation energy. In this case, the HFB+ model give a unsatisfactory description of the level density obtained for ^{192}Os .

5.3 The γ -strength function

The final γ -strength function versus γ -ray energy for ^{192}Os is displayed in Figure 5.8 together with data points from Kopecky et al. [47] (K.), Capote et al. [46] (R.), Berman et al. [78] (B.) and Shizuma et al. [79] (S.).

Similar to the NLD, the γ SF displays large uncertainties (blue band). The statistical errors, displayed in black in Figure 5.6 and 5.8, increase in magnitude

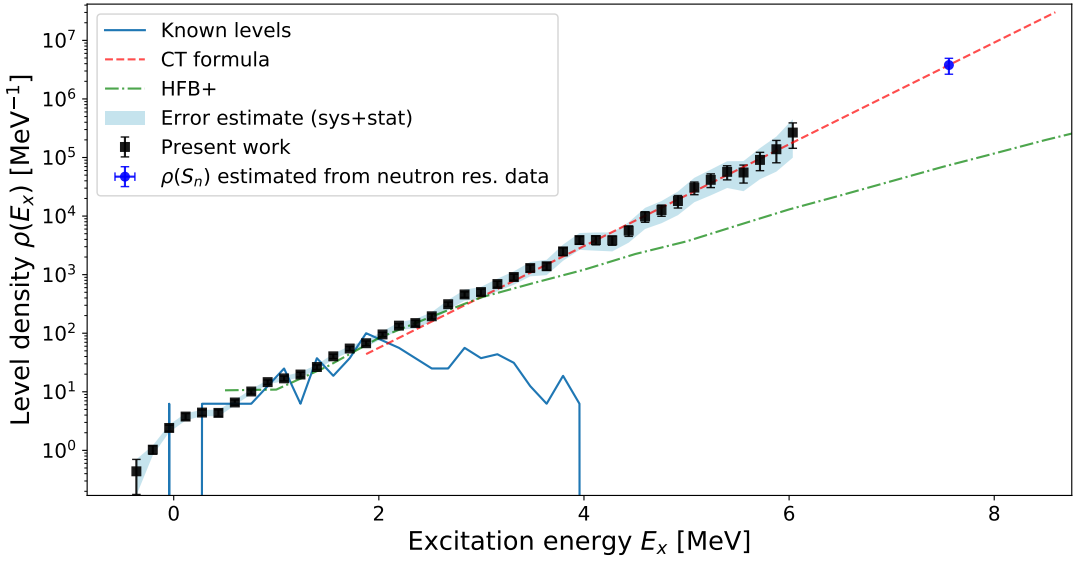


Figure 5.7: Level density versus excitation energy for the Oslo data (black) and the CT extrapolation (red) in addition to the HFB+ model [44]. The systematic uncertainties obtained in subsection 5.1.3 combined with the statistical errors are presented as the colored band.

at higher γ -ray energy, from $\approx 8\%$ at the lowest- E_γ data point, to $\approx 40\%$ at the highest- E_γ data point. The average of the higher and lower systematic uncertainties have a similar magnitude over the whole energy range, varying between $\approx 31\%$ at low γ -ray energy, to $\approx 46\%$ at high γ -ray energy. Combined, the systematic and statistical uncertainty ranges between $\approx 30\%$ at low energy, to $\approx 60\%$ at high energy. It is only the last five data points that have an error larger than 50%.

In general, the higher uncertainty estimate has a larger value than the lower estimate for the γ SF, due to the asymmetric higher and lower estimates of the

Table 5.3: The fit parameters for the GLO and SLO functions (Equation 2.12 and 2.14), using the high (H), recommended (R) and lower (L) γ SF and the (γ, n) data points by [78]. The width E_{M1} and the energy centroid Γ_{M1} of the SLO function was held constant during the fitting procedure.

	E_{E1} [MeV]	Γ_{E1} [MeV]	σ_{E1} [mb]	T_f [MeV]	E_{M1} [MeV]	Γ_{M1} [MeV]	σ_{M1} [mb]
H	13.1	2.3	713	1.5	7.1	4	4.5
R	13.2	2.8	615	1.2	7.1	4	2.1
L	13.2	3.0	572	1.0	7.1	4	0.7

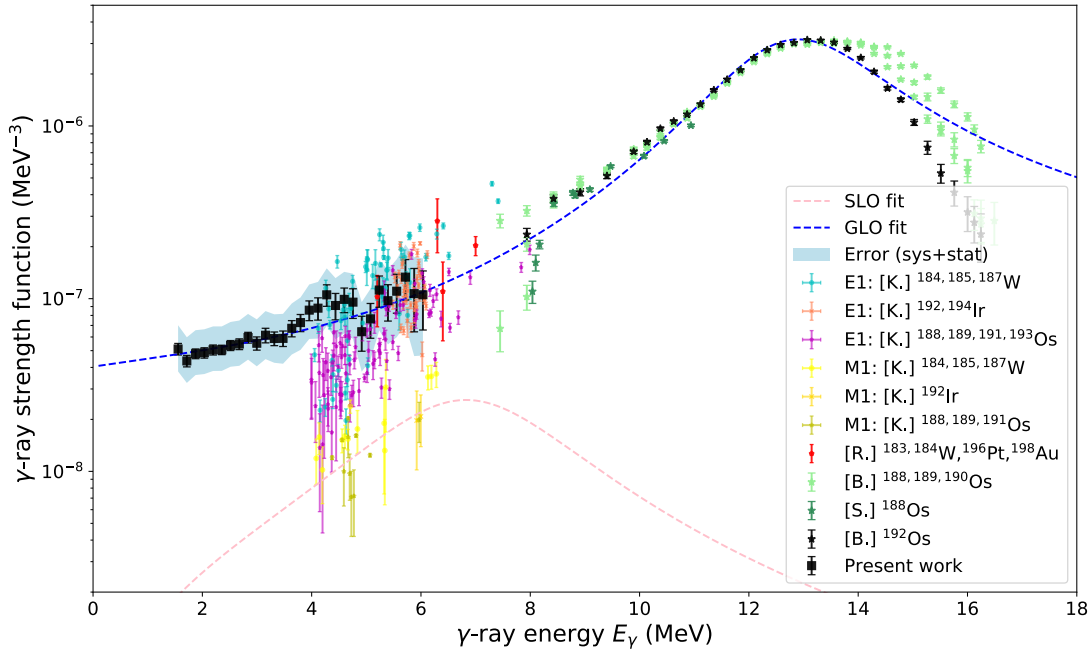


Figure 5.8: The γ -strength function versus γ -ray energy. The systematic uncertainties obtained in subsection 5.1.3 combined with the statistical errors are presented as the colored band. In addition, $E1$ -strength values of $^{188,189,191,193}\text{Os}$ (magenta), $^{192,194}\text{Ir}$ (coral) and $^{184,185,187}\text{W}$ (cyan) and $M2$ -strength values of $^{188,189,191}\text{Os}$, ^{192}Ir and $^{184,185,187}\text{W}$ (yellow) from [47] are presented. RIPL-2 $E1$ values for $^{183,184}\text{W}$, ^{196}Pt and ^{198}Au (red) are taken from [46]. The (γ, n) data is taken from Berman et al [78] for $^{188,189,190,192}\text{Os}$ and Shizuma et al. [79] for ^{188}Os . The estimated $E1$ and $M1$ strengths are shown as the blue and pink dotted lines, respectively.

normalization parameters in Table 5.2. In addition, the smallest uncertainty of the γ SF is larger than the smallest error of the NLD. This is due to the $\langle \Gamma_\gamma \rangle$ value, which only influences the uncertainty of the γ SF. The normalization of the NLD is not dependent on the $\langle \Gamma_\gamma \rangle$ value, while the uncertainty of the NLD normalization parameters propagates into the γ SF error. However, compared to the (γ, n) data points by Berman et al. [78] and Shizuma et al. [79], the absolute value of the γ SF looks reasonable.

The separate $E1$ and $M1$ strengths of the final γ SF were found by a fitting $f_{total}^{total} = f_{E1}^{GLO} + f_{M1}^{SLO}$ (Equation 2.12 and 2.14) to the Oslo data and the (γ, n) data points by [78], see Figure 5.8. The number of free parameters for the SLO (Equation 2.14) were reduced by following the suggestion of [46], see subsection 2.5.2. Using this global parameterization for the SLO parameters, i.e., setting the width and the energy centroid constant, the only unconstrained parameter of the SLO function was the peak cross section σ_{SLO} . For the GLO

parameters on the other hand, the best fit of all parameters was found by treating all parameters as free with no constraints. The optimized parameters are listed in Table 5.3.

The result of the fitting procedure is presented in Figure 5.8 as the blue and pink dotted lines for the $E1$ and $M1$ strength, respectively. As expected, the overall shape of the GLO is well adjusted to the Oslo data and the Giant dipole resonance (GDR) represented by the (γ, n) data points. Similarly, the absolute value of the estimated $M1$ strength agrees well with the $^{188,189,191}\text{Os}$, ^{192}Ir and $^{184,185,187}\text{W}$ values given in [47].

Although none of the data points provided by [47] or [46] are $E1$ or $M1$ parameters of the ^{192}Os isotope, they do provide a consistency check, i.e., that the strengths have approximately the same magnitude. A large spread in strength in the $E1$ data provided by [47] of $^{192,194}\text{Ir}$, $^{188,189,191,193}\text{Os}$ and $^{184,185,187}\text{W}$ is observed, most data points lie within the uncertainty of the Oslo data, but several points lie outside as well.

Due to the limited E_γ -energy range and large uncertainties of the Oslo data, it is difficult to say whether there exist any significant structures in the γ SF of ^{192}Os . It could be that a pygmy dipole resonance [80] exists in the osmium isotopes. Its presence would largely affect the MACS calculations, but unfortunately it is not possible to conclude on the existence of such structures with the present results.

5.4 The radiative neutron capture cross section

The final step in this work is to constrain the MACS of the $^{191}\text{Os}(n, \gamma)^{192}\text{Os}$ reaction by applying the experimental NLD and γ SF in the TALYS code [44] introduced in chapter 2.

In Code 5.1 the input file is shown, including all input parameters applied, utilized by TALYS to calculate the MACS values by means of the experimental NLD and γ SF. The first block of parameters is required TALYS input, i.e., the minimal number of parameters accepted. Here, the involved species in the $^{191}\text{Os}(n, \gamma)^{192}\text{Os}$ reaction is listed: projectile (n), ejectile (γ), element (Os) and mass (191). The energy keyword must be given, but will later become irrelevant since MACS values will be calculated, i.e., an average over a large number of incident energies is performed (see Equation 2.3).

The keyword `Nlevels` is used to limit the number of known discrete levels, from tables such as [18], used by TALYS. In this case the number of levels are set to 29, as this is approximately where the discrete levels saturate, i.e., where the experimental level density and the discrete levels show a significantly different slope at $E_x \approx 2$ MeV (Figure 5.7).

To use the $E1$ and $M1$ strengths obtained in the previous section, the keywords `E1file` and `M1file` are used. The files `TALYS_E1_rec_strength.txt` and `TALYS_M1_rec_strength.txt` contain tables of the estimated $E1$ and $M1$ strengths

in the very particular format specified by the TALYS manual. The strength files must be present in the same folder as the input file itself.

```

projectile n
ejectiles g
element Os
mass 191
energy 0.002 # arbitrary energy

equidistant y
transeps 1.00E-15
xseps 1.00E-25
popeps 1.00E-25
preequilibrium y
gnorm 1.

# (a) MODIFIED (HF+) TABLES
# i.e., the NLD from the present work
ldmodel 4
ptable 76 192 0.0
ctable 76 192 0.0
Nlevels 76 192 29

# (b) GAMMA STRENGTH FUNCTION TABLES
# i.e., E1 and M1 strengths from the present work
E1file 76 192 TALYS_E1_rec_strength.txt
M1file 76 192 TALYS_M1_rec_strength.txt

# Global parameters for the n-OMP
localomp n

# Files to check that the output is correct:
outlevels y
outdensity y
outgamma y

# MACS for a range of T:
astro y
# MACS for kT=30 keV only:
# astroE 0.03

```

Code 5.1: TALYS input file for the $^{191}\text{Os}(n, \gamma)^{192}\text{Os}$ reaction.

Table 5.4: Parameters used to calculate the standard deviation of the MACS values. Here, M_X correspond to the MACS obtained by using ρ_Y and f_Z as input in the TALYS code.

M_{rec}	M_2	M_3	M_4	M_5	M_6	M_7
ρ_{rec}	$\rho_{D_0,high}$	$\rho_{D_0,low}$	$\rho_{\sigma,low}$	$\rho_{\sigma,high}$	ρ_{rec}	ρ_{rec}
f_{rec}	$f_{D_0,high}$	$f_{D_0,low}$	$f_{\sigma,low}$	$f_{\sigma,high}$	$f_{\langle \Gamma_{\gamma 0} \rangle,low}$	$f_{\langle \Gamma_{\gamma 0} \rangle,high}$
M_8	M_9	M_{10}	M_{11}	-	-	-
$\rho_{stat,low}$	$\rho_{stat,high}$	ρ_{rec}	ρ_{rec}	-	-	-
$f_{stat,low}$	$f_{stat,high}$	$f_{stat,low}$	$f_{stat,high}$	-	-	-

Unfortunately, a keyword similar to the $E1$ and $M1$ files is not implemented in TALYS for the NLD². Therefore, the experimental NLD is given as input to the code in a very intricate way. The OCL software [58] tabulates the experimental NLD in the specific TALYS format, and gives it as an output file (`talys_nld_cnt.txt`). Then, the content of this file is copied and pasted into the NLD file that TALYS will read for ^{192}Os , in this case the tabulated NLD model number four (`1dmodel 4`)³.

At the very end at the input file, the keyword for the MACS calculation is given. Here, two kinds of calculations are done, either: 1) `astro y` specifying a MACS calculation over a range of astrophysically relevant temperatures, chosen by TALYS, or 2) `astroE 0.03` specifying a MACS calculation at a single temperature of $T = 0.03 \text{ keV}/k_b$. Unfortunately, two separate calculations must be done, as the latter temperature is not included in the former temperature range. In addition, the output files given by the two calculations (using the different MACS keywords) are identical, so the first may overwrite the second. See the TALYS manual and [44] for further details on the input parameters given in Code 5.1.

The TALYS calculation done by means of the experimental NLD and γ SF is compared to a TALYS default run. This default calculation is performed with identical keywords as listed in Code 5.1, except for the keywords relevant to the NLD and γ SF, i.e., the blocks marked (a) and (b) are excluded. Then, the TALYS code will set the remaining parameters to default, according to the manual.

To quantify the uncertainty of the final, experimentally constrained MACS value, the error bands of the NLD and γ SF are propagated into the uncertainty of the MACS values. The upper and lower limits of the NLD and γ SF obtained in the previous section are applied to calculate the ‘systematic’ part of the standard

²Hopefully, this workaround method will not be necessary in the future as it is prone to human errors, relying on manual copy and paste labor.

³The NLD file of `1dmodel 4` is found in the TALYS directory: `talys/structure/density/ground/goriely/Os.tab`

Table 5.5: The Maxwellian-averaged (n, γ) cross sections with corresponding standard deviation STD (in the unit of mb) at the s-process temperature $k_b T = 30$ keV for the $^{191}\text{Os}(n, \gamma)^{192}\text{Os}$ reaction. Values from KADoNiS [19] (KAD), the TALYS [44] default run (DEF) and the present work (OCL18) are compared. Four theoretical MACS values from [81] (RaT99), [82] (HWF76), [83] (Gor02) and [84] (Gor05) calculated in 2000, 1976, 2002 and 2005, respectively, are listed.

	OCL18	KAD	DEF	RaT99	HWF76	Gor02	Gor05
$\langle\sigma\rangle_{n,\gamma}$	1134	1290	523	802	1090	1565	1399
STD	354	280	-	-	-	-	-

deviation of the MACS value:

$$STD_{sys,high}^2 = \left(\frac{M_2 - M_{rec}}{M_{rec}} \right)^2 + \left(\frac{M_4 - M_{rec}}{M_{rec}} \right)^2 + \left(\frac{M_6 - M_{rec}}{M_{rec}} \right)^2, \quad (5.10)$$

and

$$STD_{sys,low}^2 = \left(\frac{M_3 - M_{rec}}{M_{rec}} \right)^2 + \left(\frac{M_5 - M_{rec}}{M_{rec}} \right)^2 + \left(\frac{M_7 - M_{rec}}{M_{rec}} \right)^2, \quad (5.11)$$

where M_Y denote a MACS value calculated by means of the TALYS code using the NLD and γ SF input Y listed in Table 5.4. The ‘statistical’ part of the standard deviation of the MACS value is calculated as:

$$\begin{aligned} STD_{stat}^2 &= \left(\frac{M_8 - M_{rec}}{M_{rec}} \right)^2 + \left(\frac{M_{10} - M_{rec}}{M_{rec}} \right)^2 \\ &= \left(\frac{M_9 - M_{rec}}{M_{rec}} \right)^2 + \left(\frac{M_{11} - M_{rec}}{M_{rec}} \right)^2 \end{aligned} \quad (5.12)$$

since the statistical contribution to the errors are symmetrical, i.e., the statistical errors contribute equally to the lower and upper MACS estimate.

Then, the statistical and systematic uncertainties can be combined into the final standard deviation of the MACS value by:

$$STD_{tot,high} = M_{rec} \sqrt{STD_{sys,high}^2 + STD_{stat}^2}, \quad (5.13)$$

and

$$STD_{tot,low} = M_{rec} \sqrt{STD_{sys,low}^2 + STD_{stat}^2} \quad (5.14)$$

The Maxwellian-averaged cross section for the $^{191}\text{Os}(n, \gamma)^{192}\text{Os}$ reaction calcu-

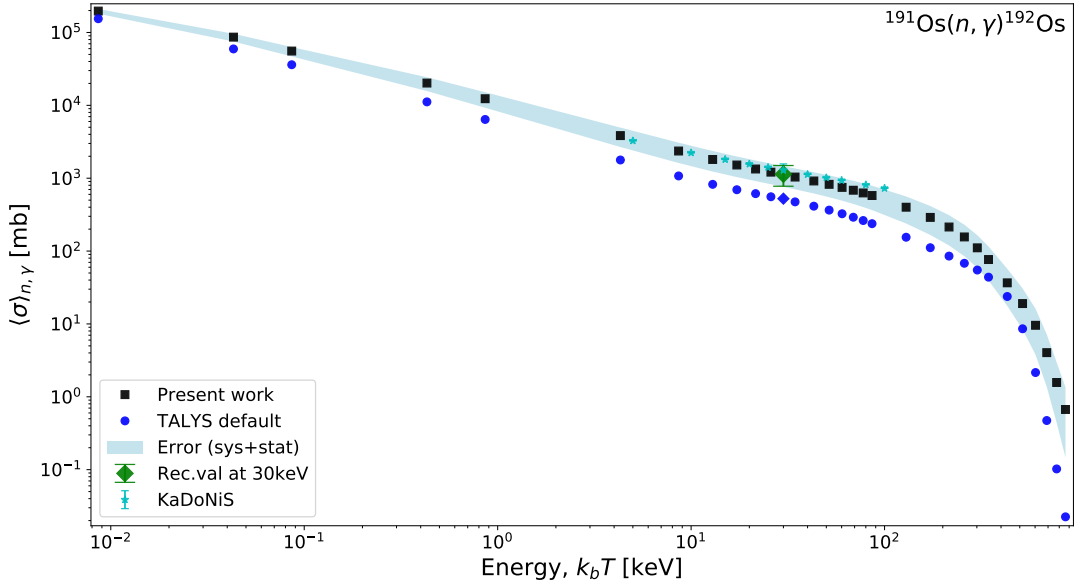


Figure 5.9: The Maxwellian-averaged (n, γ) cross section versus incident neutron energy $E_n = kT$ at the stellar temperature T . The systematic and statistical uncertainties (blue band) of the recommended MACS for the $^{191}\text{Os}(n, \gamma)^{192}\text{Os}$ reaction are presented as the colored band. In addition, values from the KADoNiS library [19] and a TALYS calculation done with default input are shown. Points at the s-process temperature $kT = 30$ keV are highlighted with a separate marker.

lated with the TALYS code [44] is presented in Figure 5.9. The propagated uncertainty, the colored band, lies between $\sim 6\%$ and $\sim 100\%$ at low and high incident neutron energy, respectively. It is in particular the six last data points that have an uncertainty larger than 50%. Although the uncertainties estimated in the current work are asymmetrical, the upper and lower standard deviations are rather similar in magnitude, providing a mean of $STD_{mean} = (348.8 \text{ mb} + 358.6 \text{ mb})/2 \approx 354 \text{ mb}$ at the energy of 30 keV.

KADoNiS [19] only lists the uncertainty for the MACS at 30 keV. It is not clear how this uncertainty is determined, [19] and [36] write: “The MACS from $kT=5$ keV to 100 keV are obtained from theoretical calculations with corresponding uncertainties between 25 and 50% in most cases.” Therefore, it is difficult to determine how robust the KADoNiS uncertainty estimate is. As it is the only theoretical MACS value provided with an uncertainty, it will be used as the principal value for comparison with the value obtained in this work.

For the energy range between $k_b T = 5 - 100$ keV in Figure 5.9, the values provided by KADoNiS [19] agree well with the present, constrained MACS values. Interestingly, the theoretical estimate provided by the TALYS default input

parameters gives a significantly smaller cross section value than the present result and the KADoNiS values over the whole energy range. This is likely due to an overall lower default level density and γ SF in the TALYS code compared to the present experimental data and to the models used in KADoNiS.

A comparison of the MACS values at the s-process temperature of 30 keV is presented in Table 5.5. As noticed before, the TALYS default value is significantly lower than the present result and the KADoNiS MACS, and lies outside of the error band. In addition, four theoretical MACS values from [81] (RaT99), [82] (HWF76), [83] (Gor02) and [84] (Gor05), listed at the KADoNiS web page [19], are presented. The deviations between the four theoretical values are large, but lie within the uncertainty of the present work, except for the value at 1565 mb by [83] in 2002. This MACS was later updated in 2005 to 1399 mb [83].

The magnitude of the systematic and statistical errors leads to a rather large relative error in the present result of $\approx 32\%$ in contrast to $\approx 22\%$ for the KADoNiS cross sections. Nevertheless, it is rewarding to observe that the theoretical value provided by KADoNiS is consistent and well within the uncertainty of the experimentally constrained MACS obtained in this work.

Chapter 6

Summary and outlook

“The universe is big. It’s vast and complicated and ridiculous. And sometimes, very rarely, impossible things just happen and we call them miracles.”

— The Doctor, Dr. Who, Season 5, Episode 12

6.1 Summary of the results

In the current work, the first experimentally constrained Maxwellian-averaged cross section for the $^{191}\text{Os}(n, \gamma)^{192}\text{Os}$ reaction relevant to the s-process nucleosynthesis has been obtained. The nuclear level density and the γ -strength function of ^{192}Os have been extracted from particle-coincidence data using the Oslo method and normalized by means of parameters estimated from neutron-resonance data of isotopes in the vicinity of ^{192}Os . The uncertainties obtained by the error estimate of the normalization parameters have the same order of magnitude as the errors propagated by the Oslo method.

No significant structures are revealed in the nuclear level density of ^{192}Os and the exponential growth of the constant temperature model describes the level density well. Although the estimated uncertainties of the level density are large ($\approx 9\text{--}60\%$), in particular at high excitation energy, the Hartree-Fock-Bogolyubov plus combinatorial model lies orders of magnitudes outside of the errors of the experimental level density.

The uncertainties of the γ -strength function are slightly larger than the errors of the level density ($\approx 30\text{--}60\%$), but the overall absolute value agrees well with (γ, n) data and $E1$ and $M1$ strengths provided by external data. The given energy range and uncertainties makes it difficult to conclude on the presence of any significant structures in the γ -strength function.

The experimentally constrained result of the Maxwellian-averaged cross section, $\langle\sigma\rangle_{n,\gamma} = 1134 \pm 354 \text{ mb}$ at 30 keV, is consistent with the theoretical predic-

tions listed in the KADoNiS library. The TALYS default calculation, on the other hand, yields a $\approx 50\%$ lower Maxwellian-averaged cross section value compared to the present result, lying outside of the experimental error bar.

Although, the propagated uncertainty obtained for the Maxwellian-averaged cross sections is large ($\approx 32\%$), the errors have been estimated in a conservative and transparent way. This is, perhaps, in contrast to several values purely relying on theory for which no uncertainty is reported.

6.2 Upgrade of the experimental setup: OSCAR

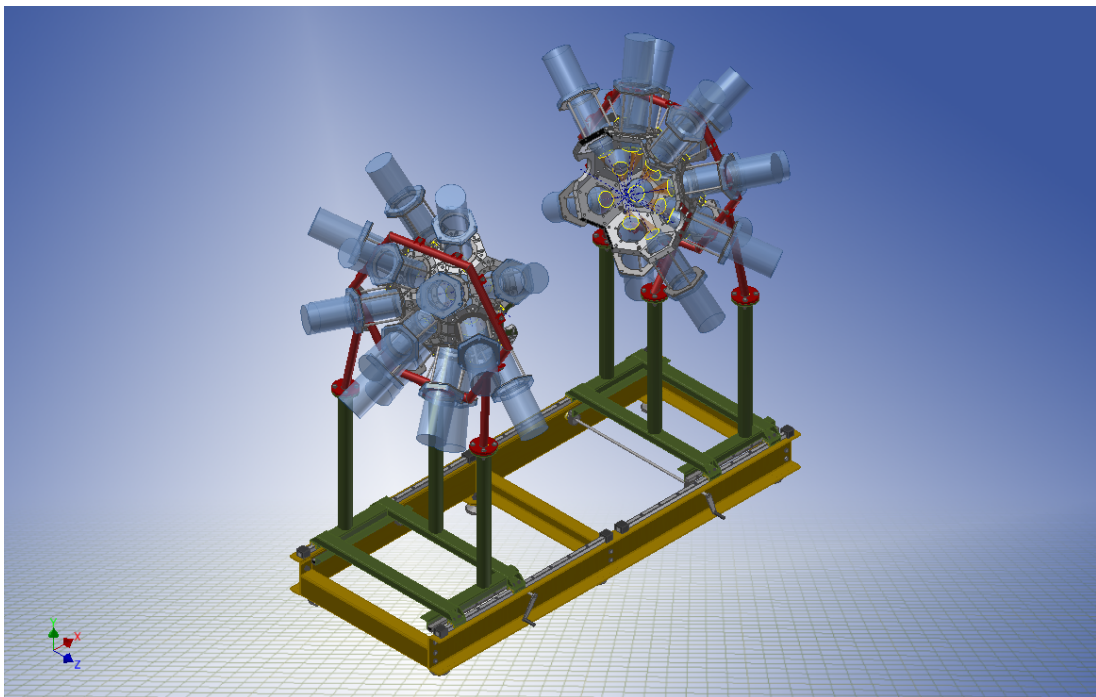


Figure 6.1: A 3D model of the new OSCAR detector array at the OCL. The detectors are mounted on a frame that can be opened, providing convenient access to the target chamber as illustrated in the figure by [85].

The infrastructure at OCL was recently updated with a new detector array based on 30 large volume ($3.5'' \times 8''$) LaBr₃(Ce) scintillator crystals and a new digital data acquisition system, see Figure 6.1. The first experiment with the complete detector array at the OCL was performed in late 2017. Also, some of the LaBr₃ detectors have already been used at international facilities such as HIE-ISOLDE and iThemba LABS.

OSCAR's superior energy resolution allows for an entirely new class of experiments to be conducted. An interesting question not investigated in this work is the spin dependence of the level density. This aspect of the NLD will be studied in future experiments. With the OSCAR detectors it is possible to gate on individual transitions and study a spin-gated level density.

In addition, the exceptional timing resolution of the LaBr₃ crystals allows for neutron discrimination, providing reliable Oslo data above the neutron separation energy overlapping with (n, γ) data. This gives the nuclear physics group in Oslo the opportunity to investigate the Brink hypothesis, which the Oslo method relies on, in great detail.

6.3 Outlook

The present thesis has been motivated by the numerous unresolved questions in regard to the synthesis of heavy elements. In this work, the neutron capture rate of a single reaction, i.e., $^{191}\text{Os}(n, \gamma)^{192}\text{Os}$ has been experimentally constrained, but the need for more data remain a critical challenge.

Within the current data set, it is possible to extract the nuclear level density and γ -strength function of ^{194}Ir and ^{193}Ir created by the $^{192}\text{Os}(\alpha, d)^{194}\text{Ir}$ and $^{192}\text{Os}(\alpha, t)^{193}\text{Ir}$ reactions. In this way, multiple reaction rates can be obtained by gating on the deuterium and tritium banana in the present data set, without performing any new experiments.

In addition, the mass region of osmium involve several branch-point isotopes with a large impact on the s-process path. Complementary experiments with the new OSCAR detectors at the OCL using targets of stable isotopes in the vicinity of ^{192}Os would result in several MACS values. Hence, new experimentally constrained data points would be obtained in a region currently relying on theoretical calculations.

It is not possible to conclude on the astrophysical implications of this work by means of a single Maxwellian-averaged cross section. To study the impact of the $^{191}\text{Os}(n, \gamma)^{192}\text{Os}$ reaction, the current result would have to be implemented in an s-process nucleosynthesis reaction network code including branch points, which lies outside the scope of this work. Nevertheless, the present result provides a useful test of reaction theory, and contribute to the eminent nucleosynthesis puzzle.

Bibliography

- [1] N. R. Council. *Connecting Quarks with the Cosmos: Eleven Science Questions for the New Century.* The National Academies Press, Washington, DC, 2003. ISBN 978-0-309-07406-3. doi: 10.17226/10079. URL <https://www.nap.edu/catalog/10079/connecting-quarks-with-the-cosmos-eleven-science-questions-for-the>.
- [2] Image credit: NASA/The Jet Propulsion Laboratory, Caltech. URL <https://www.jpl.nasa.gov/infographics/infographic.view.php?id=10824>. Accessed: May, 2018.
- [3] E. M. Burbidge, G. R. Burbidge, W. A. Fowler, and F. Hoyle. Synthesis of the Elements in Stars. *Review of Modern Physics*, 29(4), 1957. doi: <https://doi.org/10.1103/RevModPhys.29.547>.
- [4] A. G. W. Cameron. Nuclear reactions in stars and nucleogenesis. *Publications of the Astronomical Society of the Pacific*, 69(408):201–222, 1957. ISSN 00046280, 15383873. URL <http://www.jstor.org/stable/40676435>.
- [5] F. Hoyle. A New Model for the Expanding Universe. *Monthly Notices of the Royal Astronomical Society*, 108:372, 1948. doi: 10.1093/mnras/108.5.372.
- [6] A. G. Lemaitre. Contributions to a British Association Discussion on the Evolution of the Universe. *Nature*, 128:704–706, 1931. URL <http://dx.doi.org/10.1038/128704a0>.
- [7] F. Hoyle. The nature of the universe; a series of broadcast lectures. In *Basil Blackwell, Oxford*, page 121. 1950. URL <http://adsabs.harvard.edu/abs/1950nusb.book.....H>.
- [8] G. Gamow. Expanding universe and the origin of elements. *Physical Review*, 70(7-8):572–573, 1946. ISSN 0031899X. doi: 10.1103/PhysRev.70.572.2.
- [9] R. A. Alpher, H. Bethe, and G. Gamow. On the origin of the chemical elements. *Physical Review*, 73(7):803–804, 1948. doi: 10.1103/PhysRev.73.803. URL <https://link.aps.org/doi/10.1103/PhysRev.73.803>.

- [10] R. H. Cyburt, B. D. Fields, K. A. Olive, and T. H. Yeh. Big bang nucleosynthesis: Present status. *Reviews of Modern Physics*, 88(1):1–22, 2016. ISSN 15390756. doi: 10.1103/RevModPhys.88.015004.
- [11] G. Audi, F. G. Kondev, M. Wang, W. J. Huang, and S. Naimi. The NUBASE2016 evaluation of nuclear properties. *Chinese Physics C*, 41(3):1–138, 2017. ISSN 16741137. doi: 10.1088/1674-1137/41/3/030001.
- [12] C. Iliadis. *Nuclear Physics of Stars*. John Wiley & Sons, 2015. ISBN 9783527336494. URL <https://books.google.no/books?id=riTPBwAAQBAJ>.
- [13] Image credit: NASA, J. P. Harrington (U. Maryland) and K. J. Borkowski (NCSU). URL https://www.nasa.gov/multimedia/imagegallery/image_feature_741.html Accessed: Feb, 2018.
- [14] B. Balick, J. Wilson, and A. R. Hajian. NGC 6543: The Rings Around the Cat’s Eye. *The Astronomical Journal*, 121(1):354–361, 2001. ISSN 00046256. doi: 10.1086/318052. URL <http://stacks.iop.org/1538-3881/121/i=1/a=354%5Cnpapers2://publication/doi/10.1086/318052>.
- [15] P. W. Merrill. Spectroscopic Observations of Stars of Class. *The Astrophysical Journal*, 116:21, July 1952. doi: 10.1086/145589.
- [16] F. Käppeler, R. Gallino, S. Bisterzo, and W. Aoki. The s process: Nuclear physics, stellar models, and observations. *Reviews of Modern Physics*, 83(1):157–193, apr 2011. ISSN 0034-6861. doi: 10.1103/RevModPhys.83.157. URL <https://link.aps.org/doi/10.1103/RevModPhys.83.157>.
- [17] A. I. Karakas and J. C. Lattanzio. The dawes review 2: Nucleosynthesis and stellar yields of low- and intermediate-mass single stars. *Publications of the Astronomical Society of Australia*, 31:e030, 2014. doi: 10.1017/pasa.2014.21.
- [18] Data extracted using the NNDC On-Line Data Service from the ENSDF database. URL <https://www.nndc.bnl.gov/ensdf/>. Accessed: 2017-2018.
- [19] Data extracted using the KADoNiS On-Line Data Service. URL <http://www.kadonis.org>. Accessed: 2018-05-01.
- [20] J. Lippuner and L. F. Roberts. SkyNet: a modular nuclear reaction network library. *The Astrophysical Journal Supplement Series*, 233(2), 2017. ISSN 1538-4365. doi: 10.3847/1538-4365/aa94cb. URL <http://arxiv.org/abs/1706.06198>.
- [21] M. Arnould, S. Goriely, and K. Takahashi. The r-process of stellar nucleosynthesis: Astrophysics and nuclear physics achievements and mysteries. *Physics Reports*, 450(4-6):97–213, 2007. ISSN 03701573. doi: 10.1016/j.physrep.2007.06.002.

- [22] F. K. Thielemann, A. Arcones, R. Kppeli, et al. What are the astrophysical sites for the r-process and the production of heavy elements? *Progress in Particle and Nuclear Physics*, 66(2):346–353, 2011. ISSN 01466410. doi: 10.1016/j.ppnp.2011.01.032. URL <http://dx.doi.org/10.1016/j.ppnp.2011.01.032>.
- [23] B. P. Abbott, R. Abbott, T. D. Abbott, et al. GW170817: Observation of Gravitational Waves from a Binary Neutron Star Inspiral. *Physical Review Letters*, 119(16):30–33, 2017. ISSN 10797114. doi: 10.1103/PhysRevLett.119.161101.
- [24] A. Goldstein, P. Veres, E. Burns, et al. An Ordinary Short Gamma-Ray Burst with Extraordinary Implications: Fermi-GBM Detection of GRB 170817A. *The Astrophysical Journal Letters*, 848(2):L14, 2017. ISSN 2041-8213. doi: 10.3847/2041-8213/aa8f41. URL <http://arxiv.org/abs/1710.05446>{%}0A<http://dx.doi.org/10.3847/2041-8213/aa8f41>.
- [25] V. Savchenko, C. Ferrigno, E. Kuulkers, et al. INTEGRAL Detection of the First Prompt Gamma-Ray Signal Coincident with the Gravitational Wave Event GW170817. *The Astrophysical Journal Letters*, 848(2):L15, 2017. ISSN 2041-8213. doi: 10.3847/2041-8213/aa8f94. URL <http://arxiv.org/abs/1710.05449>{%}0A<http://dx.doi.org/10.3847/2041-8213/aa8f94>.
- [26] D. Kasen, B. Metzger, J. Barnes, E. Quataert, and E. Ramirez-Ruiz. Origin of the heavy elements in binary neutron-star mergers from a gravitational-wave event. *Nature*, 551(7678):80–84, 2017. ISSN 14764687. doi: 10.1038/nature24453. URL <http://dx.doi.org/10.1038/nature24453>.
- [27] S. Goriely and H. T. Janka. Solar r-process-constrained actinide production in neutrino-driven winds of supernovae. *Monthly Notices of the Royal Astronomical Society*, 459(4):4174–4182, 2016. doi: 10.1093/mnras/stw946. URL <http://dx.doi.org/10.1093/mnras/stw946>.
- [28] M. Arnould, S. Goriely, and K. Takahashi. The p-process of stellar nucleosynthesis: astrophysics and nuclear physics status. *Physics Reports*, 384 (1-2):1–84, 2003. doi: [https://doi.org/10.1016/S0370-1573\(03\)00242-4](https://doi.org/10.1016/S0370-1573(03)00242-4).
- [29] B. V. Kheswa, M. Wiedeking, F. Giacoppo, et al. Galactic production of ^{138}La : Impact of $^{138},^{139}\text{La}$ statistical properties. *Physics Letters, Section B: Nuclear, Elementary Particle and High-Energy Physics*, 744:268–272, 2015. ISSN 03702693. doi: 10.1016/j.physletb.2015.03.065. URL <http://dx.doi.org/10.1016/j.physletb.2015.03.065>.
- [30] J. J. Cowan and W. K. Rose. Production of C-14 and neutrons in red giants. *The Astrophysical Journal*, 212:149–158, February 1977. doi: 10.1086/155030.

- [31] F. Herwig, M. Pignatari, P. R. Woodward, et al. Convective-reactive proton-¹²C combustion in Sakurai's object (V4334 Sagittarii) and implications for the evolution and yields from the first generations of stars. *Astrophysical Journal*, 727(2), 2011. ISSN 15384357. doi: 10.1088/0004-637X/727/2/89.
- [32] P. Denissenkov, G. Perdikakis, F. Herwig, et al. The impact of (n, γ) reaction rate uncertainties of unstable isotopes near $n = 50$ on the i-process nucleosynthesis in he-shell flash white dwarfs. *Journal of Physics G: Nuclear and Particle Physics*, 45(5):055203, 2018. URL <http://stacks.iop.org/0954-3899/45/i=5/a=055203>.
- [33] Facility for Rare Isotope Beams, Michigan State University (FRIB). URL <http://www.frib.msu.edu>.
- [34] Facility for Antiproton and Ion Research in Europe GmbH (FAIR). URL <http://www.fair-center.eu>.
- [35] High intensity and Energy-ISOLDE at CERN (ISOLDE). URL <http://hie-isolde-project.web.cern.ch>.
- [36] Z. Bao, H. Beer, F. Käppeler, et al. Neutron Cross Sections for Nucleosynthesis Studies. *Atomic Data and Nuclear Data Tables*, 76(1):70–154, 2000. ISSN 0092640X. doi: 10.1006/adnd.2000.0838. URL <http://linkinghub.elsevier.com/retrieve/pii/S0092640X00908386>.
- [37] I. Dillmann, M. Heil, F. Käppeler, et al. Kadonis the karlsruhe astrophysical database of nucleosynthesis in stars. *AIP Conference Proceedings*, 819(1):123–127, 2006. doi: 10.1063/1.2187846. URL <https://aip.scitation.org/doi/abs/10.1063/1.2187846>.
- [38] I. Dillmann, T. Szűcs, R. Plag, et al. The Karlsruhe Astrophysical Database of Nucleosynthesis in Stars Project - Status and Prospects. *Nuclear Data Sheets*, 120:171–174, 2014. ISSN 00903752. doi: 10.1016/j.nds.2014.07.038.
- [39] Data extracted using the NNDC On-Line Data Service from the NUDAT 2.7 database. URL <http://www.nndc.bnl.gov/nudat2/>.
- [40] A. C. Larsen. Starting Grant application to the European Research Council (2014).
- [41] S. Hilaire and S. Goriely. Global microscopic nuclear level densities within the HFB plus combinatorial method for practical applications. *Nuclear Physics A*, 779:63–81, 2006. ISSN 03759474. doi: 10.1016/j.nuclphysa.2006.08.014.

- [42] T. Ericson. The statistical model and nuclear level densities. *Advances in Physics*, 9(36):425–511, 1960. doi: 10.1080/00018736000101239. URL <https://doi.org/10.1080/00018736000101239>.
- [43] A. Gilbert and A. G. W. Cameron. A composite nuclear-level density formula with shell corrections. *Canadian Journal of Physics*, 43(8):1446–1496, 1965. doi: 10.1139/p65-139. URL <https://doi.org/10.1139/p65-139>.
- [44] S. Goriely, S. Hilaire, and A. J. Koning. Improved predictions of nuclear reaction rates with the TALYS reaction code for astrophysical applications. *Astronomy & Astrophysics*, 487(2):767–774, 2008. ISSN 0004-6361. doi: 10.1051/0004-6361:20078825. URL <http://www.aanda.org/10.1051/0004-6361:20078825>.
- [45] G. A. Bartholomew, E. D. Earle, A. J. Ferguson, J. W. Knowles, and M. A. Lone. *Gamma-Ray Strength Functions*. Springer Science + Business Media, 1973. ISBN <http://id.crossref.org/isbn/978-1-4615-9044-6>. doi: 10.1007/978-1-4615-9044-6_4.
- [46] R. Capote, M. Herman, P. Obložinský, et al. RIPL - Reference Input Parameter Library for Calculation of Nuclear Reactions and Nuclear Data Evaluations. *Nuclear Data Sheets*, 110(12):3107–3214, 2009. ISSN 00903752. doi: 10.1016/j.nds.2009.10.004.
- [47] J. Kopecky, S. Goriely, S. Péru, S. Hilaire, and M. Martini. E1 and M1 functions from average resonance capture data. *Physical Review C*, 95(5):054317, 2017. ISSN 2469-9985. doi: 10.1103/PhysRevC.95.054317. URL <http://link.aps.org/doi/10.1103/PhysRevC.95.054317>.
- [48] J. M. Blatt and V. F. Weisskopf. *Theoretical Nuclear Physics*. John Wiley & Sons, Inc., 1952.
- [49] The homepage of the Oslo Cyclotron Laboratory (OCL). URL <http://www.mn.uio.no/fysikk/english/research/about/infrastructure/OCL/>. Accessed: 2017-09-13.
- [50] N. Nenoff, G. Baldsiefen, H. Hübel, et al. Dipole band structures in ^{195}Hg . *Nuclear Physics A*, 629(3-4):621–634, 1998. ISSN 03759474. doi: 10.1016/S0375-9474(98)00653-8.
- [51] W. R. Leo. *Techniques for Nuclear and Particle Physics Experiments*. Springer-Verlag, 1994. ISBN 3540572805.
- [52] M. Guttormsen, A. Bürger, T. E. Hansen, and N. Lietaer. The SiRi particle-telescope system. *Nuclear Instruments and Methods in Physics Research*,

- Section A: Accelerators, Spectrometers, Detectors and Associated Equipment*, 648(1):168–173, 2011. ISSN 01689002. doi: 10.1016/j.nima.2011.05.055.
- [53] L. Crespo Campo, F. L. Bello Garrote, T. K. Eriksen, et al. Statistical γ -decay properties of 64-Ni and deduced (n,γ) cross section of the s-process branch-point nucleus 63-Ni. *Physical Review C*, 94(4):044321, 2016. ISSN 2469-9985. doi: 10.1103/PhysRevC.94.044321. URL <https://link.aps.org/doi/10.1103/PhysRevC.94.044321>.
 - [54] Qkinz kinematics calculator. doi: <https://doi.org/10.5281/zenodo.1154143>.
 - [55] A. C. Larsen. *Statistical properties in the quasi-continuum of atomic nuclei*. PhD thesis, 2008.
 - [56] M. Guttormsen, A. Atac, G. Lsvhsiden, et al. Statistical Gamma-Decay at Low Angular Momentum. 1990.
 - [57] All OCL source codes. URL <https://github.com/oslocyclotronlab/oslo-method-software>. Accessed: 2017-09-13.
 - [58] Oslo Method Software. doi: <https://doi.org/10.5281/zenodo.1153994>.
 - [59] H. Bethe and J. Ashkin. Passage of radiations through matter. In E. Segre, editor, *Experimental Nuclear Physics*, volume 1. Jhon Wiley & Sons, New York, 1953.
 - [60] J. Ziegler, J. Biersack, and U. Littmark. *The Stopping and Range of Ions in Solids*. Pergamon Press, New York, 1985.
 - [61] K. D. Borg, R. Meijer, and A. D. Woude. The $^{16}\text{O}(\alpha, p)^{19}\text{F}$ reaction at $E\alpha = 40$ MeV. *Nuclear Physics A*, 273(1):172–188, nov 1976. ISSN 0375-9474. doi: 10.1016/0375-9474(76)90306-7. URL <https://www.sciencedirect.com/science/article/pii/0375947476903067>.
 - [62] M. Guttormsen, T. S. Tveter, L. Bergholt, F. Ingebretsen, and J. Rekstad. The unfolding of continuum γ -ray spectra. *Nuclear Instruments and Methods in Physics Research A*, 374:371–376, 1996. ISSN 01689002. doi: 10.1016/0168-9002(96)00197-0.
 - [63] D. Lay. *Linear Algebra and its Applications*. Pearson, 4th edition, 2014. ISBN 1292020555.
 - [64] The Geant4 toolkit for the simulation of the passage of particles through matter. URL <http://geant4.web.cern.ch>.

- [65] A. C. Larsen, M. Guttormsen, M. Krčíčka, et al. Analysis of possible systematic errors in the Oslo method. *Physical Review C - Nuclear Physics*, 83(3), 2011. ISSN 1089490X. doi: 10.1103/PhysRevC.83.034315.
- [66] M. Guttormsen, T. Ramsoy, and J. Rekstad. The first generation of gamma-rays from hot nuclei. *Nuclear Instruments and Methods in Physics Research*, 255:518–523, 1987. ISSN 01689002. doi: 10.1016/0168-9002(87)91221-6.
- [67] E. Fermi. *Nuclear Physics*. University of Chicago Press, Chicago, 1950. URL <http://www.press.uchicago.edu/ucp/books/book/chicago/Nbo3631242.html>.
- [68] P. A. M. Dirac. The Quantum Theory of the Emission and Absorption of Radiation. *Proceedings of the Royal Society A: Mathematical, Physical and Engineering Sciences*, 114(767):243–265, 1927. ISSN 1364-5021. doi: 10.1098/rspa.1927.0039. URL <http://rspa.royalsocietypublishing.org/cgi/doi/10.1098/rspa.1927.0039>.
- [69] M. Guttormsen, A. C. Larsen, A. Bürger, et al. Fermi’s golden rule applied to the γ decay in the quasicontinuum of Ti46. *Physical Review C - Nuclear Physics*, 83(1):1–10, 2011. ISSN 1089490X. doi: 10.1103/PhysRevC.83.014312.
- [70] D. M. Brink. PhD thesis, Oxford University, 1955.
- [71] A. Schiller, L. Bergholt, M. Guttormsen, et al. Extraction of level density and γ strength function from primary γ spectra. *Nuclear Instruments and Methods in Physics Research, Section A: Accelerators, Spectrometers, Detectors and Associated Equipment*, 447(3):498–511, 2000. ISSN 01689002. doi: 10.1016/S0168-9002(99)01187-0.
- [72] M. Guttormsen, S. Goriely, A. C. Larsen, et al. Quasicontinuum γ decay of Zr 91,92: Benchmarking indirect (n,γ) cross section measurements for the s process. *Physical Review C*, 96(2):1–10, 2017. ISSN 24699993. doi: 10.1103/PhysRevC.96.024313.
- [73] T. von Egidy and D. Bucurescu. Systematics of nuclear level density parameters. *Physical Review C - Nuclear Physics*, 72(4), 2005. ISSN 05562813. doi: 10.1103/PhysRevC.72.044311.
- [74] S. F. Mughabghab. *Atlas of Neutron Resonances*. Elsevier, Amsterdam, fifth edition, 2006. ISBN 9780080461069. URL <https://www.elsevier.com/books/atlas-of-neutron-resonances/mughabghab/978-0-444-52035-7>.

- [75] S. F. Mughabghab. *Atlas of Neutron Resonances*. Elsevier, Amsterdam, sixth edition, 2018. ISBN 978-0-444-63769-7. URL <https://www.sciencedirect.com/science/article/pii/B9780444637697000063>.
- [76] T. von Egidy and D. Bucurescu. Experimental energy-dependent nuclear spin distributions. *Physical Review C - Nuclear Physics*, 80(5):1–19, 2009. ISSN 1089490X. doi: 10.1103/PhysRevC.80.054310.
- [77] K. Fujii, M. Mosconi, A. Mengoni, et al. Neutron physics of the Re/Os clock. III. Resonance analyses and stellar (n,γ) cross sections of Os186,187,188. *Physical Review C - Nuclear Physics*, 82(1):1–18, 2010. ISSN 1089490X. doi: 10.1103/PhysRevC.82.015804.
- [78] B. L. Berman, D. D. Faul, R. A. Alvarez, P. Meyer, and D. L. Olson. Giant resonance in transitional nuclei: Photoneutron cross sections for osmium isotopes. *Physical Review, Part C, Nuclear Physics*, 19:1205, 1979. doi: 10.1103/PhysRevC.19.1205. URL <http://dx.doi.org/10.1103/PhysRevC.19.1205>.
- [79] T. Shizuma, H. Utsunomiya, P. Mohr, et al. Photodisintegration cross section measurements on W186, Re187, and Os188: Implications for the Re-Os cosmochronology. *Physical Review C - Nuclear Physics*, 72(2):1–9, 2005. ISSN 1089490X. doi: 10.1103/PhysRevC.72.025808.
- [80] D. Savran, T. Aumann, and A. Zilges. Experimental studies of the Pygmy Dipole Resonance. *Progress in Particle and Nuclear Physics*, 70:210–245, 2013. ISSN 01466410. doi: 10.1016/j.ppnp.2013.02.003. URL <http://dx.doi.org/10.1016/j.ppnp.2013.02.003>.
- [81] T. Rauscher and F. K. Thielemann. Atomic data nucl. data tables, 75, 1 (2000).
- [82] J. Holmes, S. Woosley, W. Fowler, and B. Zimmerman. Atomic data nucl. data tables 18, 305 (1976).
- [83] S. Goriely. Hauser-Feshbach rates for neutron capture reactions. v. 2002.
- [84] S. Goriely. Hauser-Feshbach rates for neutron capture reactions. v. 8/29/2005.
- [85] Illustration created by Jan Mierzejewski, C3D (UiO copyright).